Electrochemical Model Studies on Metal-air and Lithium-ion Batteries

Universität Ulm

Institut für Oberflächenchemie und Katalyse

Dissertation

Zur Erlangung des Doktorgrades Dr. rer. nat.

der Fakultät für Naturwissenschaften der Universität Ulm

vorgelegt von

Dorothea Alwast

(Augsburg)

2020

Amtierender Dekan:	Prof. Dr. Thorsten Bernhardt
1. Gutachter:	Prof. Dr. R. Jürgen Behm
2. Gutachter:	Prof. Dr. Werner Tillmetz

Tag der Promotion: 08.03.2021

Contents

1 Introduction 1

1.1 Novel battery systems 1

1.2 Ionic liquids – electrolytes for novel batteries? 3

1.3 The electrochemical stability window 4

1.4 The oxygen reduction reaction in ionic liquids 6

1.5 Differential Electrochemical Mass Spectrometry – A Promising Method for Battery Investigation? 7

1.6 Objective 9

2 Experimental section 11

2.1 Electrochemical measurement systems 11

2.1.1 Swagelok cell for volatile electrolytes 11

2.1.2 Open beaker cell for ionic liquid decomposition 14

2.1.3 Electrochemical flow-cell 17

2.2 Electrochemical procedure 19

2.2.1 Cyclic Voltammetry 19

2.2.2 Linear Sweep Voltammetry 20

2.2.3 Oxygen reduction reaction and oxygen evolution reaction measurements 20

2.3 Electrode preparation 21

2.3.1 Reference electrodes 21

2.3.2 Working electrodes 22

2.3.3 Counter electrodes 23

2.4 Karl-Fischer titration 23

2.5 X-ray diffraction 24

2.6 Scanning electron microscopy and energy dispersive X-ray spectroscopy 24

3 Results and discussion 27

3.1 DEMS study on the stability of the Li_xVO_2F electrode and electrolyte decomposition at the electrode 27

3.1.1 Introduction 27

3.1.2 Results and discussion 28

3.1.3 Summary 33

3.2 A Novel Approach for Differential Electrochemical Mass Spectrometry Studies on the Decomposition of Ionic Liquids 35
3.2.1 Abstract 35
3.2.2 Introduction 35
3.2.3 Results and Discussion 38
3.2.3.1 BMP-TFSI 38
3.2.3.2 EMIM-TFSI 48
3.2.4 Conclusions 54
3.2.5 Supporting Information 55
3.3 Effect of Li^+ and Mg^{2+} on the Electrochemical Decomposition of the Ionic Liquid 1-Butyl-1-methylpyrrolidinium bis(trifluoromethanesulfonyl)imide and Related Electrolytes 61
3.3.1 Abstract 61
3.3.2 Introduction 62
3.3.3 Results and discussion 63
3.3.3.1 Influence of impurities 63
3.3.3.2 Effect of the electrode material 69
3.3.3.3 Influence of the addition of Li^+ and Mg^{2+} salts 74
3.3.4 Conclusions 80
3.3.5 Supporting information 81
3.4 Influence of additives on the reversible ORR / OER in the magnesium containing ionic liquid N-Butyl-N-methylpyrrolidinium bis(trifluoromethane-sulfonyl)imide 83
3.4.1 Abstract 83
3.4.2 Introduction 84
3.4.3 Results and discussion 86
3.4.3.1 Influence of $Mg(TFSI)_2$ on the ORR in BMP-TFSI 86
3.4.3.2 ORR/OER in the presence of crown ether additive 88
3.4.3.3 Drying agents 94
3.4.4 Summary 98
3.4.5 Supporting Information 99

3.5 Ionic Liquid Electrolytes for Metal-Air Batteries: Interactions between O_2, Zn^{2+} and H_2O Impurities 101
3.5.1 Abstract 101
3.5.2 Introduction 102
3.5.3 Results 104
3.5.4 Discussion 115
3.5.5 Conclusions 117
3.5.6 Supporting Information 118
4 Summary **119**
5 Zusammenfassung (German) **123**
6 Bibliography **129**
7 Appendix **143**
7.1 Liste der verwendeten Daten 143
7.2 Lebenslauf 145
7.3 Publikationen 147
7.4 Danksagung 149
7.5 Erklärung 151

Abbreviations

BMP-TFSI	1-butyl-1-methylimidazolium bis(trifluoromethanesulfonyl)imide
CE	counter electrode
CV	cyclic voltammogram
DEMS	differential electrochemical mass spectrometry
DFT	density functional theory
DMC	dimethyl carbonate
EC	ethylene carbonate
EDX	energy dispersive X-ray spectroscopy
EEI	electrode electrolyte interphase
EMIM-TFSI	1-ethyl-3-methylimidazolium bis(trifluoromethanesulfonyl)imide
EW	electrochemical window
FAP	perfluoroalkane phosphate
FEP	fluorinated ethylene propylene
GC	glassy carbon
HER	hydrogen evolution reaction
IL	ionic liquid
LIB	lithium ion battery
LP30	1 M $LiPF_6$ in 1:1 wt.% EC/DMC
LUMO	lowest unoccupied molecular orbital
NBH	borane dimethylamine complex
OER	oxygen evolution reaction
ORR	oxygen reduction reaction
PEEK	polyether ether ketone
PMP-TFSI	1-propyl-1-methylpyrrolidinium bis(trifluoromethanesulfonyl)imide
PVdF	polyvinylidene difluoride
QMS	quadrupole mass spectrometer
RE	reference electrode
RRDE	rotating ring disk electrode
SEI	solid electrolyte interphase
SEM	scanning electron microscopy
UHV	ultra-high vacuum
WE	working electrode
XRD	X-ray diffraction

1 Introduction

During the last decades the development of mobile devices like mobile phones or electric vehicles lead to an increased need for transportable energy carriers. For both applications the need for batteries will increase within the next years. Lithium ion batteries are the most widely spread type of batteries for these requirements.[1-3] In this type of battery, Li^+ ions move through the electrolyte from the anode to the cathode during discharging and back when charging. For Li-ion batteries, a substantial part in terms of volume, weight and cost is the cathode material.[3-6] Typical electrodes for Lithium-ion batteries are lithium oxides with different central ions and structures like lithium cobalt oxide, lithium manganese oxide or lithium iron phosphate as cathode materials, while graphite or lithium titanate act as anode materials.[7] Though, the resources for this type of battery are limited. Therefore, a first step for batteries with lower environmental impact is the development of Cobalt-free cathode materials. Furthermore, and especially in regard to the rapid population growth and the resulting even higher need for batteries, the environmental impact of Lithium mining demonstrates the need for the development of alternative battery systems with higher energy densities consisting of abundant materials.

1.1 Novel battery systems

To increase the energy density of the common metal-ion battery three possibilities are feasible: i) increasing the transported charge within the battery by using multivalent ions, ii) using metal anodes with high energy density and oxygen from air as reactant for the cathode, or iii) increasing the maximum voltage of the battery. Metal-air batteries like Mg-air or Zn-air batteries are promising candidates, fulfilling the first two requirements. Metal-air batteries store energy by using a redox reaction between a metal anode and oxygen, the active cathode material, from ambient air. To date, unifunctional Pt or Ru/IrO_2-based noble metal catalysts show high catalytic performances regarding ORR or OER reaction in batteries.[8-12] The drawback of the combination of two unifunctional catalysts in order to achieve a bifunctional catalyst are the high commercial costs and the complexity of the preparation process.[10] For this reason, the oxygen is oxidized and reduced at a bifunctional catalyst deposited onto a porous carbon cathode. The basic reaction steps can be summarized as presented in Figure 1,

with the metal anode on the left and the porous carbon electrode on the right hand side. While primary Zn-air batteries are commercially available, rechargeable Metal-air batteries are currently under fundamental research with the objective to overcome several challenges. Often the main focus of the research is placed on the charging process. Especially for Mg-air batteries the Mg plating is a main issue due to the formation of MgO and $Mg(OH)_2$ in the presence of water impurities, which hinders further deposition.[13-15]

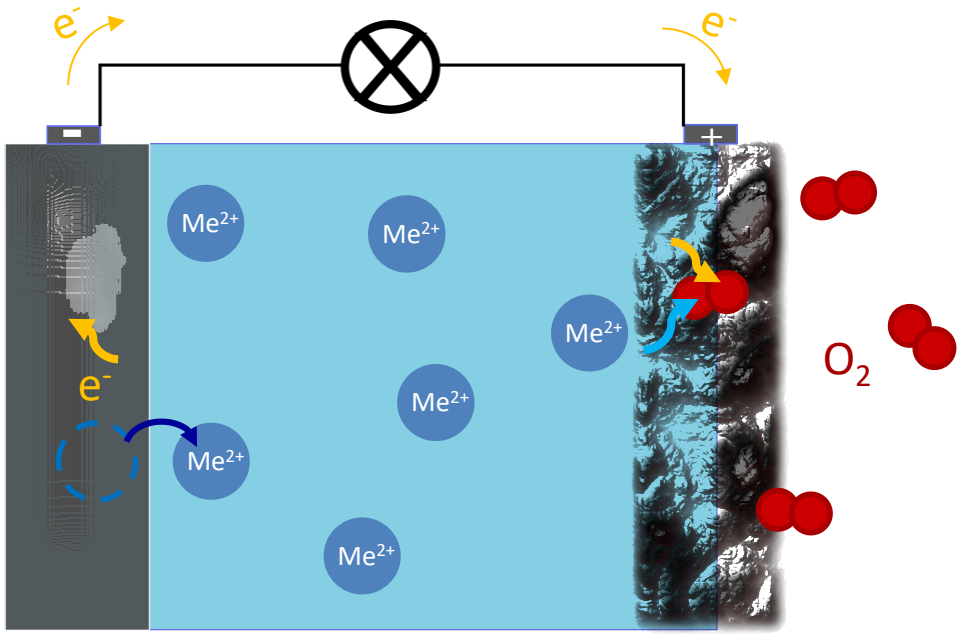


Figure 1: Sketch of a metal-air battery and occurring processes during discharge.

The primary, non-rechargeable Zn-air battery is usually based on an aqueous alkaline electrolyte. In order to develop rechargeable Zn-air batteries, the research is focussed on the reversibility of the oxygen reduction reaction (ORR) and the oxygen evolution reaction (OER) during discharge and charge of the battery.[16] Both reactions have been studied in aqueous alkaline electrolytes.[17-19] Also, the porous electrode not only enables O_2 diffusion into the cell, but also CO_2 can reach the electrolyte and form hydrogen carbonates, which change the pH value of the alkaline electrolyte and therefore change the electrochemistry of the battery cell.[4,20,21]

For these reasons, organic electrolytes and ionic liquids (ILs) offer an interesting alternative for metal-air battery electrolytes, which also have different properties as medium for the ORR and OER.[22-24]

1.2 Ionic liquids – electrolytes for novel batteries?

Ionic liquids are salts which, by definition, show a melting point below 100 °C.[25,26] The low melting point of ILs compared to inorganic salts like NaCl or $MgSO_4$ results from its bigger ions, which often contain delocalized π-electron systems or long alkyl chains, which are able to shield the ion charge and therefore hinder the formation of stable ionic bonds. Also, the asymmetry and the consequently inhibited structural arrangements of the ions leads to weaker interactions between anion and cation compared to inorganic salts.

ILs can be divided into three main categories, which differ in the type of the anion.[27,28] The first generation of ILs, which is based on $AlCl_3$, decomposes in contact with water.[29] The second generation, based on tetrafluoroborate and hexafluroborate anions, is less reactive in contact with water in comparison to first generation ILs. Nevertheless, they are strongly hygroscopic and this changes the physical and chemical properties of the IL in contact with air. Currently most of the used ILs consist of hydrophobic ions, i.e., bis(trifluoromethane-sulfonyl)imide ($TFSI^-$) or perfluoroalkane phosphate (FAP^-), which are considered as a class between the second and the third IL generation. The third generation ILs contain functional groups and can therefore be adapted to specific scopes of application, e.g., active pharmaceutical ingredients (API), which enable the production of ILs with biologic activity.[30] Common cations for all of those ILs include imidazolium, pyrrolidinium, pyridinium and tetraalkylammonium. From the combination of both, cation and anion, ILs with a huge variety of physical and chemical properties are feasible, e.g. low volatility, high thermal stability, wide electrochemical stability windows (about 5 V in comparison to 1.23 V for water[31]), low flammability and a negligible vapour pressure.

The most interesting generations for the application of ILs in metal-air batteries are the 2.5 and third generation ILs due to their water-resistance and their high electrochemical stability. Though, ILs often show a high viscosity, which is usually 30-50, partly 600 times higher than that of water.[32] This high viscosity limits the ionic conductivity due to lower mass transport of the ions. Additionally, the electrochemical stability of the ILs is highly dependent on the presence of impurities, such as water or metal ions.

In order to determine the ideal combination of anion and cation for a special task, two different approaches are feasible: one is by trial and error, the other by a systematic characterization of the properties of the ILs. The latter is obviously the better choice, though a combination of both ways – finding promising ILs by trial and error and analysing the reason for their properties to further improve the molecules – allows room for the development of even better ILs.

Numerous studies on the electrochemical behaviour of promising ILs were published within the last decade.[33-40] Due to these and other studies, promising anion and cation combinations have emerged, especially pyrrolidinium and imidazolium cations combined with the $TFSI^-$ anion. In comparison to this, the standard battery electrolytes, which are currently used for Li-ion batteries, consist of mixtures of ethylene carbonate, dimethyl carbonate and/or diethylcarbonate in combination with $LiPF_6$. These electrolytes show large disadvantages regarding safety due to their flammability. Moreover, their main disadvantage for a possible use in metal-air batteries is the volatility of the organic solvents. Both aspects can be avoided using ILs as a main component of the battery electrolyte.

1.3 The electrochemical stability window

For the application of ILs as battery electrolytes, different aspects need to be considered. Even though there are many advantages of some ILs such as the increased safety due to a reduced dendrite growth in lithium/$Li_4Ti_5O_{12}$-battery cells[41] and low flammability, the decisive factor is the performance of the battery. A rechargeable battery can be realized by two different methods: i) by the use of an electrolyte that is stable in the used potential range, does not decompose and thus does not passivate the electrodes, or ii) by using an electrolyte which is reductively decomposed at the anode but forms a stable electrode electrolyte interphase (EEI) that is both ion-conducting and passivating towards unwanted side reactions, including further electrolyte decomposition. The structure and the composition of the EEI are also essential for the initial capacity loss, self-discharge characteristics, cycle life, rate capability and safety of batteries.[42] Though, the processes at this interphase are very complex and it is hardly possible to analyse it in a complete battery. One first step for improving the EEI, and consequently the battery, is the fundamental understanding of the electrochemical decomposition mechanisms of the ILs on suitable model systems. Especially the EEI components, i.e., the products of electrolyte decomposition, are a key aspect for the performance.[42]

Generally, the electrochemical stability of the ILs is given by the reduction and oxidation potentials. These potentials are noted versus a reference potential, which is given by a suitable (see discussion below, chapter 2.3.1) reference electrode. In order to study the decomposition mechanisms and to allow conclusions on the occurring processes during decomposition, as a starting point for well-defined and well-structured model electrodes noble metal electrodes, i.e., Au and Pt are used.[43-45] While the Nernst potentials for oxidation and reduction are defined by thermodynamics, the measured potentials are often influenced by kinetics and thus

the working electrode acting as an electro-catalyst has a relevant impact on the stability of the electrolyte. Carbon is commonly used as support for catalysts, conductive agent or host material for metal ions on the anode side.[7] Thus, glassy carbon can be used as well-defined model substrate.[43]

Furthermore, the stability of the ILs is influenced by impurities like halides or water. Even though water decreases the viscosity of the IL and increases the conductivity, it is able to catalyse the IL decomposition.

In preliminary studies different approaches were used to investigate the electrochemical stability and the consequential decomposition mechanism. Among others, cyclic voltammetry (CV) measurements were performed to determine the electrochemical stability window of ILs.[43-45]

In order to improve the IL electrolyte it is necessary to identify whether the anion or the cation is decomposed at respective potentials and which decomposition mechanism proceeds. For the determination of the potential window of pyrrolidinium and TFSI-based ILs, it is commonly accepted that at anodic potentials the anion decomposition is the limiting factor.[40] For cathodic potentials, there is an ongoing discussion whether the anion or the cation is decomposed first.[33,35,46] Ab-initio molecular orbital theory and density functional theory (DFT) studies combined with infrared spectroscopy were used by Howlett et al.[35] to investigate the stability of 1-butyl-1-methylpyrrolidinium bis(trifluoromethanesulfonyl)imide (BMP-TFSI). They reported that the decomposition of the anion starts at more positive potentials than the cathodic breakdown of the IL.[34,35] However, at cathodic potentials the cation decomposition is the main decomposition pathway. Similarly, Kroon et al.[46] utilized DFT calculations and mass spectrometry after decomposition to demonstrate that the cation is reduced at cathodic potentials, forming a radical. This radical can be either instable and decompose, or it can recombine with other formed radicals or it can chemically react with alkenes, forming an even larger radical (radical addition-reaction).

Despite these measurements, however, the potential-dependent decomposition mechanism still remains unclear. By the help of potential dependent tracking of the electrochemical decomposition, it might be possible to gain more information on the mechanism and to make an important contribution to the discussion, which ion is decomposed first at which potential. Therefore, the electrochemical decomposition of BMP-TFSI and 1-ethyl-3-methylimidazolium bis(trifluoromethanesulfonyl)imide (EMIM-TFSI) was studied within the scope of this thesis. The results of our measurements are presented and discussed in chapter 3.2.

Since a metal battery electrolyte consists not only of a solvent, but also of dissolved metal ions (mostly Li^+ for Li-batteries) which are used as charge carrier and therefore included in the electrolyte, the influence of metal ions like Li^+ and Mg^{2+} on the electrochemical stability of the ionic liquid is a key factor for the use of ionic liquids as battery electrolytes, as well.[47,48] Similar to the measurements presented in chapter 3.2, the use of potential dependent tracking of the decomposition used in this thesis might help understanding the decomposition mechanism and the influence of metal ions on this mechanism. This will be discussed in chapter 3.3.

1.4 The oxygen reduction reaction in ionic liquids

In a metal-air battery, oxygen from air is reduced on the cathode side during discharge. In return, during charge, the oxygen ions are re-oxidized and oxygen is released again. For this reason, the electrochemical reduction and oxidation of oxygen is crucial for the battery performance. Therefore, several studies for ORR and OER regarding reversibility and the influence of the electrolyte composition in BMP-TFSI-based electrolytes on these reactions were performed.[22,49-51]

Taking a look at the mechanisms known for aqueous electrolytes for the ORR and OER is a first step towards understanding the processes occurring during ORR / OER in organic electrolytes.[52-56] The ORR in aqueous electrolytes proceeds mainly via two pathways: i) a four-electron transfer reaction from O_2 to H_2O and ii) a two-electron transfer forming hydrogen peroxide.[54-57] In aprotic organic electrolytes, the reduction can even stop after the transfer of only one electron, resulting in the formation of superoxide.[16]

For aqueous electrolytes the ORR is kinetically hindered, hence, a catalyst is used for utilizing the reaction. The best catalysts known up to now for the ORR are based on Pt[54-56,58-60], which also improves the selectivity against side reactions e.g. peroxide formation.[61,62] In organic electrolytes, in contrast, the role of the electro-catalyst on the reaction mechanism is barely understood. For different electrode materials, GC, Au,[63] Pt and manganese oxide catalysts,[64] no influence on the ORR / OER has been found in neat and Mg^{2+}-containing BMP-TFSI. This observation was explained by an outer sphere reaction mechanism, reflecting very weak interactions between the superoxide anion and the surface.[63] On the other hand, by the use of rotating ring disk electrode (RRDE) and DEMS measurements, Reinsberg et al. found a transfer of around two electrons per O_2 molecule forming peroxide on GC, Au and Pt electrodes in another organic, Mg^{2+}-containing electrolyte (0.4 M $Mg(ClO_4)_2$ in DMSO);

when using Rh electrodes even 3 to 4 electrons are transferred.[65] Thus in organic electrolytes a catalytic influence of the electrode material can be observed only in few cases and in contrast to aqueous electrolytes not for Pt or Au. Because of the low activity of noble metal catalysts (Pt, Au) in DMSO and IL-based electrolytes in comparison to GC,[51,64,65] and the high activity of said noble metals as catalyst in aqueous media, an interesting topic for studies is the influence of the addition of water as a catalyst on the ORR / OER in BMP-TFSI electrolytes, which is discussed in chapter 3.5. On the other hand, the presence of water can also lead to the irreversible formation of (Mg)-peroxide in Mg^{2+} containing electrolyte.[14,51,63,64] Thus, in this case the addition of complexing agents to remove water residuals is an interesting approach. Another option to enable the reversible O_2 reduction/oxidation is masking the Mg^{2+} ion and therefore hindering the irreversible formation of MgO_2. Both aspects were addressed in chapter 3.4 by the addition of the complexing agents borane dimethylamine complex and 18-crown-6.

1.5 Differential Electrochemical Mass Spectrometry – A Promising Method for Battery Investigation?

Differential Electrochemical Mass Spectrometry (DEMS) is a method which combines electrochemistry with mass spectrometry. With DEMS it is possible to detect the gaseous reaction products during the electrochemical reactions or the consumption of volatile educts in parallel to the electrochemical measurement. Therefore, it allows drawing a conclusion on the reactions which take place during electrochemistry.

In order to enable measurements in volatile electrolytes, a membrane is placed between the electrolyte and the vacuum of the mass spectrometer chamber.[66,67] To improve the time delay caused by the process of gas diffusion through the electrolyte and to the mass spectrometer, the working electrode is placed close to or directly on top of the membrane,[67] which can be sputter coated with a conductive metal film.[68] Another option is the use of an electrochemical flow-cell where the gaseous products pass by the membrane after the electrochemical reaction.[69,70]

By using these DEMS cells, in previous studies new insights in reaction mechanisms in different aqueous systems were achieved: For example, when studying ORR catalysts such as RuO_2 or IrO_2, the participation of the oxide-O atom was unclear. The isotopic labelling in combination with DEMS measurements showed that lattice oxygen from the catalyst is exchanged and the labelled atoms are found in the evolved O_2.[71,72]

A second example: For fuel cell applications, different platinum catalysts based on a carbon support are investigated. One challenge is the ongoing carbon corrosion and the resulting loss of the platinum surface area. Also the O_2 formation rate during OER at novel catalyst electrodes is of considerable interest. The investigation of both aspects by differentiating the formed CO, CO_2 and O_2 is possible by using DEMS.[73-75]

One first approach for the use of DEMS in Battery studies was the use of a membrane-free electrochemical cell. In this study, a headspace-like cell, where the decomposition products are transported from the gas-phase above the electrolyte to the UHV by a carrier gas, was used.[76] With this setup, the cell is directly connected to the UHV chamber. Subsequently, not only the decomposition products but also electrolyte vapour additional to the carrier gas can be measured in the mass spectrometer. Therefore, also the background signal of the electrolyte is increased in comparison to membrane-setups. Due to the high amount of carrier gas in comparison to signal height, also the spectrometer sensitivity and the dynamic range are key issues for this setup.[76]

The other option is used for non-volatile electrolytes. In this case, an open cell can be placed directly into the vacuum, where the volatile decomposition products are detected and no carrier gas is used. This approach can be used for the investigation of ionic liquid electrolytes due to their low vapour pressure.

Different cell-types for DEMS investigations which were used in the scope of this thesis are described in chapter 2.1.

1.6 Objective

As described previously, DEMS is a promising and highly successful method for investigating reaction mechanisms. Using this method by adapting it to systems which are not measurable up to date opens a new approach for the understanding of surface and interphase reactions. In this thesis I am following this idea, using newly designed DEMS setups to gain fundamental insights on the reactions taking place at realistic or model battery electrodes. For all measurements half cells are used to ensure that all measured features are only influenced by one electrode.

In a first step, a cell based on a Swagelok cell similar to the description in ref. [77] was built in order to investigate reactions on the novel cathode material Li_xVO_2F in LP30 standard electrolyte. This measurement cell was further developed based on aqueous measurement systems to overcome several issues, like the differentiation of the products formed at working and counter electrode, as it is described in chapter 2.1.1. In a second step an open cell design was developed to investigate non-volatile electrolytes like the promising ILs and the influence of metal ions on their electrochemical stability. The spotlights for these measurements were novel metal-air battery systems. For the ORR /OER reaction taking place in this type of battery, O_2 needs to be present. In order to study electrolyte systems consisting of volatile species (e.g., H_2O, O_2, ether) added into the ILs, a different closed cell design was developed, based on an aqueous DEMS flow-cell setup. With this, volatile electrolyte species are available for the electrochemical reaction.

The main part of the thesis can be separated into three groups:

i) In order to replace cobalt-containing electrodes in Li-ion batteries, the development of new battery electrode materials is a key factor. One promising cathode material is lithium vanadium oxofluoride (Li_xVO_2F). This material is assumed to have high storage capacity due to the oxidation of the oxide species in the material. DEMS measurements were performed to study the stability of the electrode material during oxidation and to determine the O_2 release. Additionally the decomposition behaviour of the electrolytes at highly positive potentials was investigated. The results are presented and discussed in chapter 3.1.

ii) For the use of ILs in novel battery systems, the electrochemical stability is a key factor. In order to improve the electrochemical stability of existing ILs, understanding the decomposition mechanism is a first step. Additionally, not only the electrolyte itself but also the charge carrier (Li^+, Mg^{2+}) is part of the electrochemical cell. Therefore, the electrochemical stability of the ILs BMP-TFSI

and 1-ethyl-3-methylimidazolium bis(trifluoromethanesulfonyl)imide (EMIM-TFSI) as well as the influence of the addition of Li^+ and Mg^{2+}, was investigated with DEMS measurements. For all measurements, a polycrystalline Au wire was used as working electrode (WE). From the different fragments detected during electrochemical decomposition, conclusions were drawn on the decomposition mechanisms in the chapters 3.2 and 3.3.

iii) Similarly, a key aspect for the development of metal-air batteries is the reversibility of the oxygen reduction reaction. For Mg^{2+}-containing BMP-TFSI, it is known that the OER only proceeds after excessive application of negative potentials to the working electrode.[51,64,78] Therefore, the addition of 18-crown-6, which is known for masking metal ions, is a promising approach for improving the ORR reversibility. Both aspects are investigated and discussed in chapter 3.4. Finally, the aspect of the presence or absence of water influencing the reversibility of the ORR in Mg^{2+} and 18-crown-6 containing electrolyte was studied in chapter 3.4. This aspect was also investigated in Zn^{2+} containing BMP-TFSI in chapter 3.5.

Conclusions for each system are given at the end of the respective chapters. Lastly, the main results will be summarized in chapter 4.

2 Experimental section

The following experimental section contains experimental descriptions that I have already published in references [110, 145, 166, 183] and is reproduced and adapted with permission from the respective journals.

For all measurements presented in this thesis four different combined electrochemistry-mass spectrometry set-ups were used, which are in the focus of this thesis and therefore described in detail in chapter (2.1). In the following chapter the procedures used in the electrochemical measurements and its differences are explained; cyclic voltammetry (2.2.1), linear sweep voltammetry (2.2.2), ORR and OER (2.2.3) measurements. In the third chapter (2.3) the preparation of the different electrodes is introduced, followed by description of the Karl-Fischer titration for determining the water content of the electrolytes in chapter (2.4). Finally, X-ray diffraction (2.5) and scanning electron microscopy (2.6) are addressed as method for post mortem analysis of the working electrode surface.

2.1 Electrochemical measurement systems

The requirements on the DEMS measurement system can be very different, depending on the electrode / electrolyte system which shall be investigated. Therefore it is necessary to adapt the cell type to the measurement task. In the following sections the different cell-systems for the electrochemical mass spectrometric measurements are presented, followed by the specific measurement and cleaning procedure.

2.1.1 Swagelok cell for volatile electrolytes

The Swagelok-cell described in ref. [77], which was originally developed for high pressure battery testing, was used in this thesis and was adapted for connection to the MS part of an existing DEMS system. The advantage of using this cell type is the comparability to standard battery tests which can also be conducted in it.[77,79,80] The test-cell consisted mainly of a Swagelok cross which is tightly sealed to the environment which houses the electrochemical cell. The Swagelok cross and the contained electrochemical cell is illustrated in the schematic drawing of the cell in Figure 2.

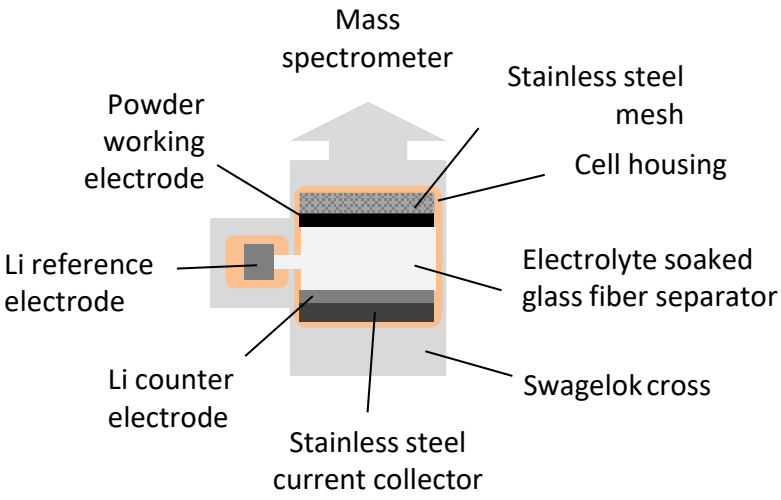


Figure 2: Schematic drawing of the measurement cell, specifically designed for model studies on the decomposition of volatile electrolytes.

The cell housing consisted out of non-conductive polyether ether ketone (PEEK) in order to avoid an electrical contact to the Swagelok cross. As a current collector for the working electrode a stainless steel mesh was used to allow the diffusion of the formed gaseous decomposition / degradation products from the working electrode to the mass spectrometer. Both electrodes were separated by an electrolyte soaked glass fiber separator, which also connected the reference electrode through a side-opening of the cell housing. In order to control the background pressure which arrived at the DEMS, additionally a leak-valve was installed between the cell and the vacuum chamber. To get a sufficient time-dependency of the electrochemical reaction and the mass spectrometric signal (at an adjusted pressure of 10^{-8} mbar no electrochemical decomposition products were detected in the time scale of one measurement), during measurement the valve was completely opened, resulting in a pressure of 10^{-6} mbar and a time-dependency below 1 s. Also in order to reduce the background pressure from volatile electrolyte components, a cooling trap was installed after the leak-valve. With this, the background pressure was reduced without hindering the online detection of electrochemical decomposition products during the measurement. Thereby, the signal to noise ratio was improved by a factor of 7. With this setup the analysis of gaseous reaction products from volatile electrolytes was possible; however, the separation between the products formed at the working and the counter electrode was not possible. For this reason the cell was further improved, based on an open design known from aqueous electrolytes.[67] In contrast to the closed Swagelok cell described before, with this open cell design it was necessary to conduct measurements inside a glovebox. Counter and reference electrodes were placed from above the electrolyte to enable the diffusion of reaction products from the counter electrode out of the measurement cell and into the glovebox.

The working electrode was again placed close to the vacuum chamber to ensure that the reaction products can be detected by the MS. To improve the signal to noise ratio, additionally a membrane was inserted between the electrolyte and the mass spectrometer chamber. A schematic drawing of the cell is shown in Figure 3.

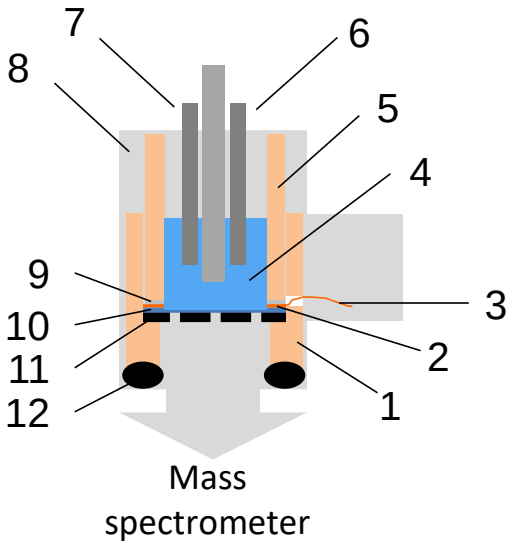


Figure 3: Schematic drawing of the measurement cell, specifically designed for the investigation of battery electrode materials in volatile electrolytes with PEEK U-cup (1), Cu ring (2), Cu wire (3), Electrolyte (4), PEEK cylinder (5), CE and RE separated by a Teflon plate (6, 7), Swagelok cross (8), Teflon ring (9), sputtered Membrane (10), stainless steel frit (11), rubber O-ring (12).

The membrane was sputtered with aluminium in order to improve the electrical contact below the electrode material (10), which was directly coated on top (detailed description in section 2.3.2). Because the membrane is non-conductive from the backside, also the electrical contacts had to be rearranged such, that even for non-metal electrodes an even charge distribution can be reached. Therefore, a Cu ring (2) was placed on top of the electrode material and the ring was contacted with a Cu wire (3), which was fed through the side-opening of the cell housing. Both, Cu ring and wire were isolated from the electrolyte by Parafilm-rings. On top a Teflon tightening ring (9) and a cylinder (5) was inserted and the assembly was pressed by mounting a standard Swagelok ferrule onto the upper cylinder in the Swagelok cross and tightening it with a standard Swagelok nut. The working and counter electrodes (6, 7) were placed from the upper opening of the Swagelok cross (8) and the cell was kept open to the glovebox-atmosphere. Due to this, the volatile decomposition products from the counter electrode were able to leave the cell towards the opening into the glovebox and therefore did not reach the membrane and could not be detected during DEMS measurements.[78]

However, the membrane only allows small molecules or fragments to pass through. Therefore, the setup with membrane was appropriate for the investigation of battery electrode

materials (i.e. oxygen evolution from breakdown of the electrode structure) and for determining small decomposition products of the electrolyte decomposition e.g. CO, CO_2, O_2, ethylene. Results presented in chapter 3.1 showed that $LiPF_6$ fragments cannot penetrate the membrane.

For the measurements in chapter 3.1, LP30 (1 M $LiPF_6$ in 1:1 wt.% EC/DMC, water content ~20 ppm, Solvionic, purity 99.9 %) was used as electrolyte. The electrochemical measurements were conducted with a potentiostat (PAR 263A) and the emerging gas was analysed in an existing external UHV chamber setup which was already described in ref. [67]. The UHV chamber is housing a quadrupole mass spectrometer (QMS, Pfeiffer Vacuum QMA 410), providing two yttritised Iridium filaments for the ionization of the volatile species, a quadrupole for mass selection of ions and an off-axis secondary electron multiplier (SEM) for ion detection.

2.1.2 Open beaker cell for ionic liquid decomposition

For the decomposition measurements of the ILs BMP-TFSI and EMIM-TFSI (see sections 3.2 and 3.3) also a specifically designed cell is favourable. Due to the very low vapour pressure of the investigated ILs it was possible to directly install the electrochemical cell into the vacuum system of the mass spectrometer (MS). A setup with membrane in between is not necessary in this case: a barrier in between electrochemical cell and MS UHV measurement chamber would even lower the sensitivity of the measurement setup. Since the reaction itself takes place in UHV, this additionally enables measurements under well-defined conditions with reduced influence of contaminations from air like oxygen and water. Therefore, for the measurement setup an additional glovebox is also not necessary.

The direct placement of the electrochemical cell in the UHV system of the mass spectrometer has another big advantage: The volatile species which are formed during decomposition can be measured with almost no time-delay in the MS. On the other hand, this setup would also have a big disadvantage: since the whole cell is inside the UHV, not only the volatile species formed at the WE are present in the UHV, but also decomposition products formed at the CE. To overcome this issue a two-chamber UHV design is necessary, which is described in Figure 4.

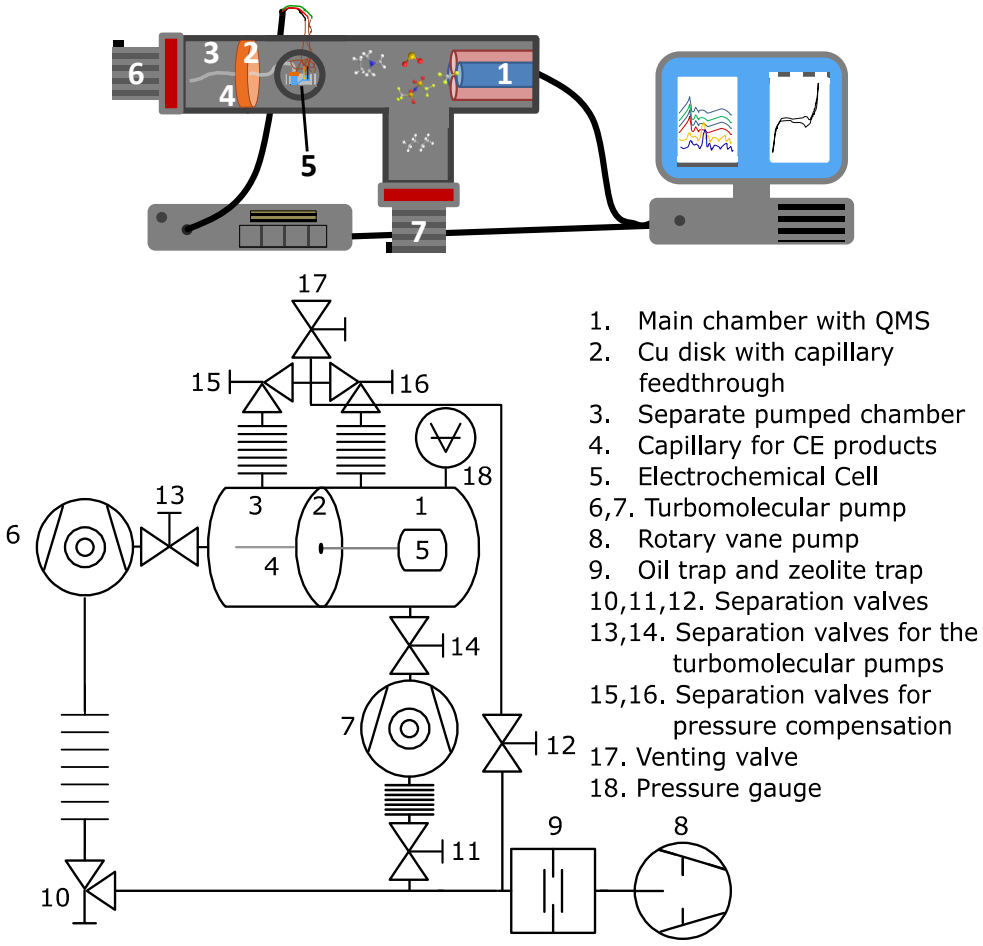


Figure 4: Schematic drawing of the UHV-DEMS System specifically designed for measurements with non-volatile electrolytes.

The UHV-DEMS System consists out of two independently pumped UHV chambers: the main chamber, which is employed with a QMS (1, details see section 2.1.1), and a separate chamber (3). The chambers are separated by a copper disk with one cannulation (2). This cannulation serves as capillary feedthrough for a fluoropropylene capillary (4, inner diameter 1.6 mm). The electrochemical cell (5, magnification in Figure 5) is directly placed into the main chamber and the CE products are led by the capillary (4) into the separate pumped chamber (3). To install the electrochemical cell before the experiment, the main chamber needs to be vented. By closing the separation valves 13 and 14, the turbomolecular pumps (6, 7) can keep running during venting of the chamber. After the installation, the chamber is pumped to $1 \cdot 10^{-3}$ mbar by the rotary vane pump by closing the valves 10 and 11 and opening 12. To ensure that the pressure difference between both chambers during pumping by the rotary vane pump cannot damage the copper disk, a pressure compensation system (15, 16) is installed. For lowering the pressure to $7 \cdot 10^{-8}$ bar, the valve 12 is closed and 10 and 11 are opened again. Afterwards, 13 and 14 are opened and 15 and 16 are closed to enable the separation of both chambers.

The following paragraph contains a revised and adapted version of the cell description published in reference [110]. The electrochemical cell (see Figure 5) consists of two compartments (diameter 0.5 cm) which are drilled into a Kel-F cell body, one is drilled completely through the cell body (19) and open at both sides and the other one is only partly drilled through and therefore closed at the bottom (20). Both compartments are interconnected by a small drill hole. The closed compartment (20) accommodates the working and the reference electrode, while the counter electrode is placed underneath the hole of the other compartment (19). The counter electrode, which is used for all measurements, is a polycrystalline Au foil, which is pressed against the opening at the bottom of the Kel-F cell body with a O-ring seal (diameter: 5 mm, thickness: 1 mm, perfluoroelastomer FPM, arcus GmbH) in between (21).

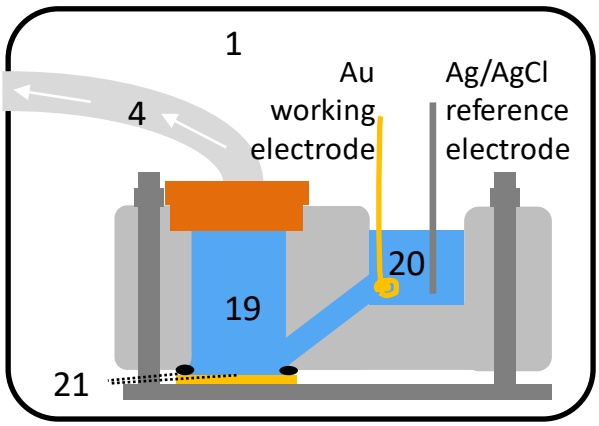


Figure 5: Schematic drawing of the measurement cell, specifically designed for model studies on the decomposition of ionic liquids.

In the first configuration during the development of the DEMS-system, the Au wire served as CE, while the Au foil was used as WE. In that case, the pumping capillary was connected to the compartment with the Au wire, and the Au wire was fit between capillary and the compartment wall such that no gas could leak from the compartment into the measurement chamber. In this case, the RE was placed into the compartment housing the Au foil. It turned out, however, that we could not detect any decomposition products from the WE compartment in this configuration. Apparently, because of the high viscosity of the IL, the diffusion of volatile reaction products through a few millimetre thick IL layer is so slow that they are not detected on the time scale of the experiments, or only smeared out over a rather long time range, which lowers the signal intensity to below the detection limit. (Note that decomposition products from the CE compartment were pumped off via the capillary and were not detected by mass spectrometry, indicating that the connection between capillary and compartment wall

was gas tight.) In the second approach used for the measurements in chapter 3.2 and 3.3, the configuration was changed such that volatile products formed at the interface between the WE (now the Au wire), the IL and the vacuum are detected with high sensitivity and a very low time delay. Now the pumping capillary was connected to the compartment with the Au foil as CE (see Figure 5). This way, we could exclude any contributions from products formed at the CE. However, in this configuration the choice of the WE is restricted to electrodes, which can be dipped into the electrolyte.[110]

For the measurements in chapter 3.2, BMP-TFSI (Merck, ultra pure > 99.0%, halides < 10 ppm, water < 10 ppm) and EMIM-TFSI (Merck, solarpure, halides < 0.1%, water < 1.0 %) was used as electrolyte. In chapter 3.3 one batch of BMP-TFSI was purchased from Merck (ultra pure > 99.0 %, halides < 10 ppm, water < 10 ppm) and another one BMP-TFSI was purchased from Solvionic (99.9 %, halides < 1 ppm; water < 20 ppm). The salts Li(TFSI) (Solvionic, 99.9 % Extra Dry, water < 20 ppm) and $Mg(TFSI)_2$ (Solvionic, 99.5 %, water < 250 ppm) were added to the IL in an Ar-filled glove box.

For the technical specifications of the potentiostat and the mass spectrometer, see section 2.1.1.

2.1.3 Electrochemical flow-cell

For investigation of electrode reactions also involving volatile species (as it is the case at the cathode of all metal-air batteries) besides an IL based electrolyte, an open cell based DEMS system as described above is not usable, because of the immediate evaporation of the volatile electrolyte components into UHV. Additionally, for an efficient and reproducible ORR a controlled mass transport during the measurement is essential. To achieve this, a flow cell has to be used, even though the advantage of the open cell design for non-volatile IL based electrolytes vanishes. In this study we adapted an existing DEMS dual thin-layer flow cell for aqueous electrolytes[70] to measurements with the more viscous and water-free ILs. For this purpose, the porous membrane, which is used in aqueous systems, was replaced by a non-porous Teflon membrane (10 µm), separating the electrolyte from the mass spectrometer chamber. This was necessary because of the lower hydrophilicity of the ILs compared to water-based electrolytes. A schematic drawing of the setup is shown in Figure 6. The dual thin-layer flow cell used for the measurements consisted of a cell body made of Kel-F® mounted on a stainless steel frit (d), where the Teflon-membrane is placed on top. The Pt counter electrode (c) is separated by a glass frit (b) from the electrochemical cell. The glassy

carbon working electrode (a) is placed face down on top of an O-ring (diameter: 7 mm, thickness: 0.5 mm, perfluoroelastomer FPM, arcus GmbH) which serves as sealing between the electrode and the cell body to prevent electrolyte leaking. The reference electrode (e) is directly placed in the outlet-capillary of the flow-cell. The electrolyte was prepared in an Ar-filled glove box and was transferred through air to a separate vacuum chamber (Figure 6g). There it was dried at 10^{-7} mbar for minimum 12 h. Prior to the measurements, the preparation chamber (6g) was filled with nitrogen and the electrolyte was pumped in a loop between the preparation chamber (6g) and the flow cell by a peristaltic pump (Ismatek, Reglo ICC) with a flow rate of 0.16 mL min^{-1} (total volume 10 mL).[51,63] The capillary system was surrounded by N_2-flushed tubes to reduce the amount of moisture and O_2 diffusing through the capillary walls. The preparation chamber (6g), which was used for drying the electrolyte, was also used for saturating it with O_2. For this, an additional gas capillary was inserted into the electrolyte reservoir to directly enrich the electrolyte with O_2 (Figure 6f).

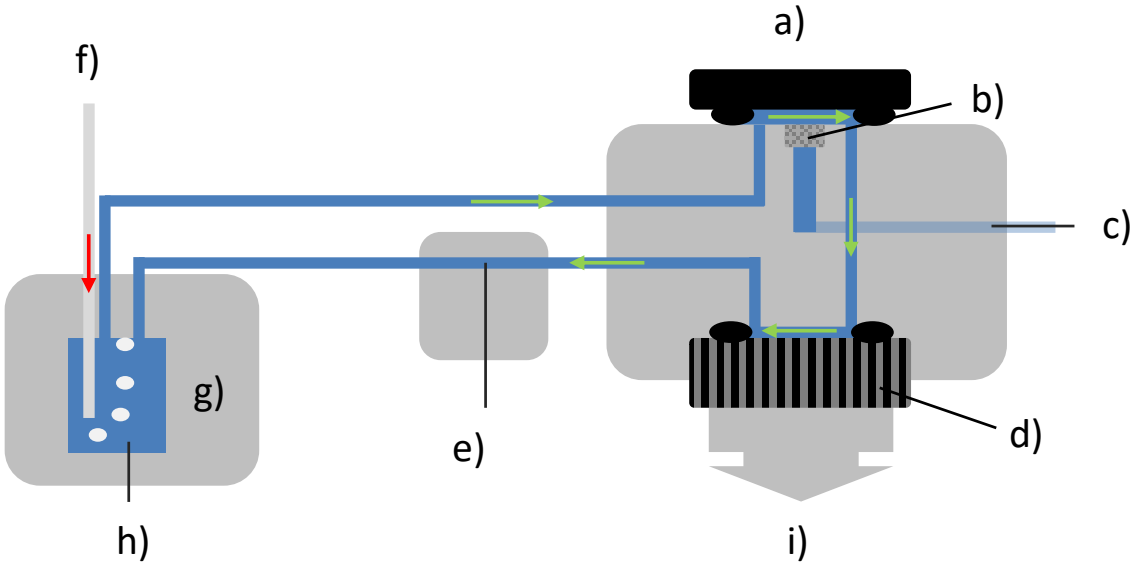


Figure 6: Schematic drawing of the measurement cell, specifically designed for model studies on the ORR and OER in ionic liquids with a) Glassy Carbon working electrode, b) glass frit, c) Pt counter electrode, d) steel frit, e) Mg/MgO reference electrode, f) gas capillary for N_2 and O_2 saturation, g) preparation chamber, h) electrolyte reservoir, i) mass spectrometric chamber.

In chapter 3.4 BMP-TFSI (Solvionic, 99.9 %, halides ≤ 1 ppm; H_2O ≤ 20 ppm), $Mg(TFSI)_2$ (Solvionic, 99.5 %, H_2O ≤ 250 ppm), 18-crown-6 (99.0 %, H_2O ≤ 0.29 %, Alfa Aesar) and borane dimethylamine complex (NBH, 97 %, Sigma-Aldrich) were used for the preparation of the electrolytes. After mixing the electrolytes in the glovebox, the electrolytes (pure BMP TFSI, the 0.1 M $MgTFSI_2$ containing BMP TFSI and the 0.1 M NBH containing BMP TFSI) were transferred through air into the vacuum chamber.

In chapter 3.5 BMP-TFSI (Solvionic, 99.9 %, halides ≤ 1 ppm; H_2O ≤ 20 ppm) and $Zn(TFSI)_2$ (Solvionic, 99.5%, water content ≤ 100 ppm) were used. The salt was added to the IL in an Ar-filled glove box. The electrolytes (neat BMP-TFSI and 0.01 M $Zn(TFSI)_2$ in BMP-TFSI) were transferred through air into the vacuum chamber. For the measurements with humidified electrolyte, O_2 was first saturated with water by bubbling it through a water-filled washing bottle at 23 °C and then conducted into the electrolyte reservoir in the preparation chamber. The water content of the humidified electrolyte was determined by Karl-Fischer titration to 0.8 ± 0.03 wt% (0.62 mol l^{-1}; 15.9 at%) in neat BMP-TFSI and 1.1 ± 0.03 wt% (0.85 mol l^{-1}; 20.6 at%) in 0.01 M $Zn(TFSI)_2$ in BMP-TFSI. In chapter 3.5 the term "dry" is used for the non-humidified electrolyte used after pumping for > 12 h in the vacuum chamber, which still contains some residual water (below 60 ppm for BMP-TFSI electrolyte).
The electrochemical measurements were carried out with a Pine Instruments potentiostat (AFRDE 5) and the emerging gas was analysed via a quadrupole mass spectrometer (Pfeiffer Vacuum QMS 422), providing a tungsten filament for the ionization of the volatile species, a quadrupole for mass selection of ions and an off-axis SEM for ion detection.

2.2 Electrochemical procedure

Different modes of electrochemical measurements have been used within the framework of this thesis. The methods for characterization of the electrodes and the electrolytes with the respective electrochemical DEMS-cell are explained in the following chapter.

2.2.1 Cyclic Voltammetry

The cyclic voltammetry (CV) measurements were performed in a three electrode set-up containing a working electrode (WE), a counter electrode (CE) and a reference electrode (RE). The voltammogram is a display of the resulting electric current from the electrode reactions plotted against the potential.[81] The applied potential is shown in Figure 7 on the left. A CV of a typical Redox-System shall be explained in Figure 7 on the right. The shown system consists of a polycrystalline Au electrode put into a $[Fe(CP)_2]$ (= Ferrocene)-containing BMP-TFSI electrolyte. A and c mark the reversal points of the potential. $[Fe(CP)_2]$ has very defined potentials for oxidation and reduction, which leads to the oxidation peak (b) in the positive going (anodic) scan and the reduction peak (d) in the negative going (cathodic) scan.

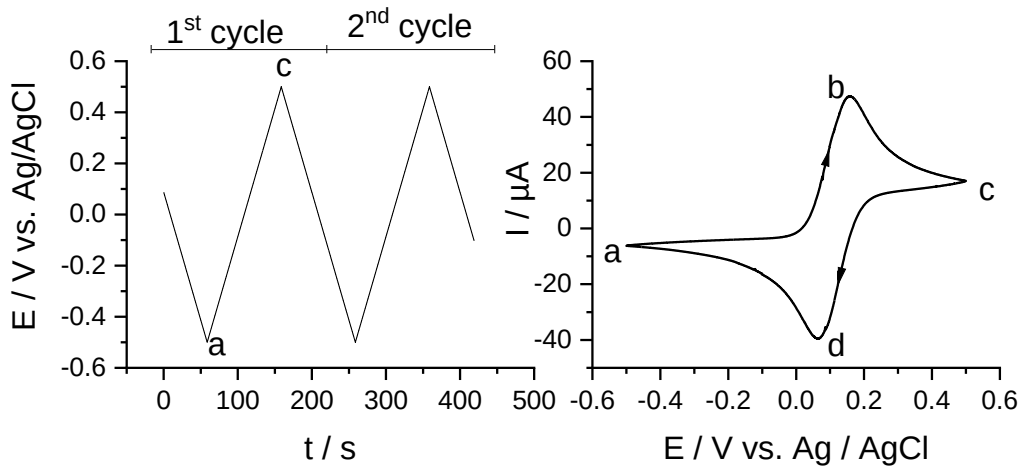


Figure 7: Left: Typical potential profile for CVs – a triangular potential wave switching the potentials at -0.5 and 0.5 V vs. Ag/AgCl; right: Cyclic voltammogram of 1 M $[Fe(Cp)_2]$ in BMP-TFSI on a polycrystalline Au electrode at 10 mV s^{-1}.

2.2.2 Linear Sweep Voltammetry

In contrast to CVs, for linear sweep voltammetry measurements the potential is only swept in one direction. This method is especially useful for beaker cell experiments, where the reaction products from preceding scans can influence the following experiments. In order to avoid these contaminations, only one scan can be performed for each experiment and afterwards the cell needs to be cleaned from all reaction residuals. This method is used for the decomposition measurements in section 3.1 and 3.2.

2.2.3 Oxygen reduction reaction and oxygen evolution reaction measurements

In the electrochemical flow cell setup, the working electrode is not directly on top of the membrane which separates the electrolyte from the vacuum in the mass spectrometric chamber. Therefore, there is a relevant delay-time until the products, which are formed / consumed at the working electrode, arrive at the membrane. This delay-time can be determined with potential step measurements. With these measurements the time of O_2 consumption / evolution can be correlated with the mass spectrometric signal. All measurements in chapter 3.4 and 3.5 are corrected by the respective delay time of 7 s for a flow rate of 0.16 mL min^{-1} applied in the electrolyte loop for all measurements.

For the DEMS measurements, the product formation rate can be monitored by recording the corresponding ion current (I_{MS}). This current is directly proportional to the incoming flow (J)

of that species (I_{MS} = k·J). When there is an additional electrochemical production of this species in the flow cell, J is given by the faradaic current I_F corresponding to that process: $J = N \cdot I_F/(z \cdot F)$, where z is the number of electrons, F is the Faraday constant and N is the ratio of I_F to the total amount of electrochemically produced species. When the current efficiency is not equal to 1, I_F has to be replaced by its product with the current efficiency, resulting in $I_{MS} = (k^*/z) \cdot I_F$ with $k^* = k \cdot N/F$.[69]

For the ORR and OER it is possible to determine a sensitivity factor k* if a reaction with a known number of transferred electrons is used. For the ORR measurements in BMP-TFSI based electrolytes I used the first reduction step (E > -0.4 V) for calibration. For this reduction step a one-electron transfer is expected.[49] Using the ratio between the ion current of the m/z 32 signal (I_{32}) and the Faradaic current (I_F) according to the equation $k^* = z \cdot I_{MS}/I_F$, a sensitivity factor k* of $4.5 \cdot 10^{-8}$ of the DEMS measurements in chapter 3.4 and k* of $3.4 \cdot 10^{-7}$ in chapter 3.5 was determined.

2.3 Electrode preparation

2.3.1 Reference electrodes

To ensure a stable potential of the reference electrode, usually a redox system with constant concentrations of each participant of the redox reaction is needed. A quasi-reference electrode is a reference electrode where no thermodynamic equilibrium is achieved. For this reason the electrodes cannot maintain a constant potential. However, under known conditions and by blending ferrocene / ferrocenium (Fc/Fc^+) or other redox couples with known redox potentials into the electrolyte these quasi reference electrodes can be related to others.[33,35] For the measurements in battery electrolytes, due to the presence of Li^+, the use of Li metal as quasi-reference electrode has been established. Therefore, in section 3.1 a lithium-stripe cut from lithium foil (99.9 %, Alfa Aesar) is used as reference electrode in LP30 (0.1 M $LiPF_6$ in ethylene carbonate : dimethyl carbonate 1:1) electrolyte.

For ionic liquid electrolytes quasi-reference electrodes are used, because it is hardly possible to find redox systems without contamination of the test solution with solvent molecules from the reference electrode. One reference electrode which can be used for ILs is the Ag/Ag^+ reference electrode, which was first described by Katayama et al.[49] This electrode is based on a silver salt (Ag(TFSI) for TFSI-based ILs), which is dissolved in the IL. To avoid Ag^+ contamination in the measurement, the reference electrode is separated from the measurement cell by a Viton-frit.[34,49,82] This electrode is an appropriate reference electrode under ambient

conditions. Under UHV conditions a more space-saving electrode is needed. Therefore, a Ag wire coated with a AgCl film was directly inserted into the measurement cell and used as quasi-reference electrode.[83] This reference electrode was prepared by annealing a Ag wire with a H_2 flame to clean the wire. Afterwards AgCl was deposited by immersing the wire into 0.1 M HCl and applying a potential of 4 V between the wire and an additional electrode for one minute, where the Ag wire was the positive electrode. After deposition the wire was rinsed with ultrapure water and again annealed in a H_2 flame until an evenly white film was formed. This electrode was used for the decomposition measurements in the chapters 3.2 and 3.3.

However, for measurements in O_2 saturated electrolyte, the Ag/AgCl redox couple is not appropriate due to the formation of Ag_2O, which results in a shift of the potential. In this case, a Mg wire (Goodfellow, 99.99+, diameter 0.25 mm) with a native oxide film was used as a reference electrode for the ORR measurements in chapters 3.4 and 3.5. All potentials given in this thesis for electrochemical systems using BMP-TFSI based electrolytes were normalized versus the Fc/Fc^+ redox couple and are therefore comparable with each other. The calibration between the different redox couples was made by adding Ferrocene into the respective electrochemical cells and measuring the offset of the Fc/Fc^+ redox signal in the CV for all reference electrodes. The potential of the Ag/Ag^+ electrode is shifted by 0.44 V vs. Fc/Fc^+,[84,85] the potential of the Li/Li^+ couple is shifted by -3.26 V,[86] and the Mg/MgO electrode is shifted by 1 V.[64] These shifts are only valid for the investigated BMP-TFSI electrolyte based systems! The potentials of LP30 based electrochemical cells are not comparable and therefore directly given vs. Li/Li^+.

2.3.2 Working electrodes

The Li_2VO_2F electrodes used in chapter 3.1 consist of 70 wt.% active material, 20 wt.% carbon black and 10 wt.% polyvinylidene difluoride binder (PVdF) (Solvey 6050). A slurry was prepared by mixing the materials with N-methyl-2-pyrrolidone (NMP, Alfa Aesar, 99.5 %). The electrode-substrate consists of a 50 µm fluorinated ethylene propylene membrane (Bohlender, Bola; for information on permeation and solubility of different gases see Pasternak et al.[87]), which was sputter coated on one side with a 40 nm Al-film. The slurry was coated onto the Al-film with doctor-blade technique and subsequently dried in vacuum for 12 h while step-wise increasing the temperature up to 120°C. The resulting electrode film was pressed with a hydraulic press (Specac) at a pressure of 1.2 ton cm^{-2}. The electrodes of

13 mm diameter were punched from the coated membrane, dried at 100 °C under vacuum and stored in an Ar glovebox. Before use, they were additionally dried in the glovebox at 100 °C on a hot plate.

For the Au wire working electrode in chapter 3.2-3.3 an as-received Au wire was bended and cleaned with acetone and boiled in water (Millipore MilliQ, 18.2 MΩ cm). After drying it was directly used for the electrochemical measurements.

The GC working electrodes used in chapter 3.3-3.5 were polished with a 0.3 µm alumina slurry prior to use and rinsed with Millipore water. Afterwards it was polished on a neoprene dish to remove residual alumina, rinsed with acetone and dried under a nitrogen flow.

2.3.3 Counter electrodes

As counter electrodes in chapter 3.1 a Li metal stripe cut from lithium foil (99.9 %, Alfa Aesar) was used. For the decomposition measurements in chapter 3.2 and 3.3 a Au foil (99.9 % Alfa Aesar) was used, which was placed below the electrochemical cell, whereas the flow-cell measurements in chapter 3.4 and 3.5 were performed with a Pt wire counter electrode (Goodfellow, 99.99+, diameter 0.5 mm), which was separated from the working electrode by a glass frit.

2.4 Karl-Fischer titration

To determine the amount of water in electrolytes (or in general: in solvents), Karl-Fischer titration is the standard method.[88] The Karl-Fischer titration is based on the reaction of SO_2 and I_2. These two molecules react in the presence of water:[89]

$$2\ H_2O + SO_2 + I_2 \rightarrow SO_4^{2-} + 2\ I^- + 4\ H^+$$

The main compartment of the titration cell contains the anode solution with added analyte. The solution consists of SO_2 and KI dissolved in pyridine and methanol. In the titration cell a Pt electrode is immersed. At the Pt anode I_2 is generated which is directly consumed by the water from the analyte.

The end point of the titration is detected by a bipotentiometric titration method. Between a second pair of Pt electrodes in the solution a detector circuit maintains a constant current between the two detector electrodes. In the presence of excess I_2 an abrupt voltage change marks the end point of the titration. From the charge which was needed to produce I_2, the amount of water in the original sample can be calculated.

The limit of detection by the used C30 Coulometric KF Titrator (Mettler Toledo) is from 1 ppm up to 5 % of water.

2.5 X-ray diffraction

A common non-destructive tool to investigate films and determine the molecular structure on the electrode surface after electrodeposition of crystalline films is X-ray diffraction (XRD). This technique provides information about the crystallographic structure and lattice parameters as well as structural changes, e.g. phase changes of the film. For the XRD measurements diffraction patterns of an X-ray beam at different lattice phases are recorded. Applying Bragg's law ($2dsin\theta = n\lambda$) on the measurements of the angles of these diffraction beams, where d is the distance between the crystal planes, θ is the scattering angle, λ the wavelength of the X-ray beam and n a positive integer, the lattice spacing of the cubic system d_{hkl} can be calculated.[90]

XRD measurements in chapter 3.5 were performed using a Siemens D5005 XRD X-ray diffractometer with CuKα radiation (λ = 1.542 Å) in a scanning range from 10-70°.

2.6 Scanning electron microscopy and energy dispersive X-ray spectroscopy

For scanning electron microscopy (SEM), a focused electron beam (1-30 kV) is scanned over the sample to gain information about the morphology and the chemical composition of the sample on the nanoscale.[91] Three different types of signals may be detected: secondary electrons (SE), backscattered electrons (BSE) and element-characteristic X-rays. The SE are electrons generated as ionization products by inelastic scattering interactions with beam electrons and only have energies of < 50 eV whereas the BSE are generated by elastic scattering of the emitted beam electrons from the sample and show energies of some keV. Because of their low kinetic energy, the SE reaching the detector originate from the first nm of the surface, therefore providing high resolution information about the morphology of the sample surface. In contrast, due to the higher energy, BSE originate from the first few µm (depending on the electron energy in the primary beam) and therefore the contrasts of images using this detector type are much lower. On the other hand, the intensity of the BSE beam is depending on the substrate material, therefore the brightness of the image changes with the material composition and a "material contrast image" can be gained. By detecting the

characteristic X-rays, energy dispersive X-ray spectroscopy (EDX) can be performed, enabling elemental mapping and estimation of the local elemental composition of the surface.
The SEM images in chapter 3.4 were recorded with a field emission-scanning electron microscope (FE-SEM, Zeiss Ultra Plus) with a beam energy of 10 to 12 kV. On small sectors of the SE-generated morphological images, EDX measurements were performed by using an additional large-area silicon-drift detector (Oxford X-Max 50) with an applied acceleration voltage of 15 kV and a detection time of 5 min per spot.

3 Results and discussion

In this section all publications are included, in which I was first or second author during the time of my thesis. Additionally a chapter about results of DEMS studies on novel cathode materials for Li-ion batteries is presented in chapter 3.1. These results were measured within the scope of Reference [92]. The first publication (chapter 3.2) includes a detailed DEMS study on the decomposition mechanism of BMP-TFSI and EMIM-TFSI at anodic and cathodic potentials. Second, a study on the influence of Li^+ and Mg^{2+} as well as the electrode material on the BMP-TFSI decomposition is presented in chapter 3.3. In the third publication (chapter 3.4) the influence of 18-crown-6 and borane dimethylamine complex on the ORR / OER in Mg^{2+} containing BMP-TFSI was studied. The last part (chapter 3.5) includes results on the ORR characteristics in Zn^{2+} containing BMP-TFSI with and without the addition of water, obtained by using a flow-cell set-up for IL-DEMS measurements.

3.1 DEMS study on the stability of the Li_xVO_2F electrode and electrolyte decomposition at the electrode

3.1.1 Introduction

The most widely spread battery system for mobile devices are Li-ion batteries. This type of rechargeable battery was largely developed by John Goodenough, Stanley Whittingham, Rachid Yazami and Akira Yoshino during the 1970s-1980s.[5,93,94] In this type of battery, Li^+ ions move through the electrolyte from the anode to the cathode during discharging and back when charging. Typically, a mixture of lithium salts such as $LiPF_6$, $LiClO_4$ or $LiBF_4$ in carbonate solvents such as ethylene carbonate, dimethyl carbonate and diethyl carbonate is used as battery-electrolyte.[95,96] For anode materials usually a carbonaceous material or lithium titanate is used.[94,97,98] However, for Li-ion batteries, a substantial part in terms of volume, weight and cost is the cathode material.[3,4] For today's Li-ion batteries, layered metal oxides are used as cathode materials such as $LiCoO_2$,[5] $LiNiO_2$,[99-101] and $LiMn_2O_4$.[102] Recent studies, however, showed that Li-rich materials with disordered rocksalt structures show good transport properties while the structural integrity of the electrode material is retained during charge and discharge.[4,103] One of these materials is Li_xVO_2F. It was claimed recently that this material shows indications for the contribution of O atoms to the capacity by the formation of peroxide and superoxide during charging.[104,105] To ensure that the formation of peroxide and

superoxide do not result in the formation of oxygen, DEMS measurements were employed and irreversible O_2 formation was investigated via DEMS. Additionally, the formation of a stable EEI, consisting of decomposed electrolyte, is a key factor for the performance of the battery. During DEMS measurement also formation of an EEI is taking place, therefore volatile reaction products from the electrochemical decomposition of the electrolyte on the electrode surface are expected to be measured in parallel.

3.1.2 Results and discussion

The measurements were performed in two different modified Swagelok cell setups described in section 2.1.1, with and without a membrane, in order to detect all different decomposition products on the one hand (without membrane) and to reduce the background pressure in order to improve the signal-to-noise ratio, thus to detect also small amounts of decomposition products (with membrane). Hence, the membrane has to be chosen such that the decomposition products are able to diffuse through the membrane. In both cases, the m/z ratios of different molecule fragments, which are attributed to the fragmentation of the LP30 electrolyte components by the mass spectrometer, such as m/z 15, 28, 32, 44 (ethylene carbonate), m/z 15, 32, 44 (dimethyl carbonate) and 85, 104 ($LiPF_6$) or to fragments of electrochemical decomposition products, e.g., ethylene (m/z 27, 28), methanol (m/z 15, 32), oxygen (m/z 32), CO (m/z 28), CO_2 (m/z 28, 44) were monitored during cyclic voltammetry measurements.[106,107]

In Figure 8 the m/z ratios of 2, 32, 44, 85, and 104, measured in the membrane-free Swagelok cell, as well as the applied voltage and the Faradaic current response are shown. Due to the open-cell design the electrode was cycled with 10 mV s^{-1}. The fast scan rate was chosen in order to avoid cell dry-out before finishing the measurement. In the first 15 minutes all ion current signals show a significant decrease, which is caused by the falling pressure after opening the valve between the cell and the measurement chamber. The signals of m/z 2, 32 and 44 show again an increase during the first linear sweep, starting roughly after 30 minutes of measurement time. The change of the signals seems independent of the applied voltage and falls again after two hours. This hints to a change in the background signals (consisting of non-decomposed electrolyte components, which reach the gas phase and are fragmented by the MS) shortly after starting the measurement, possibly influenced by diffusion of the electrolyte through the electrode material. The shape of the increase on the m/z 2 and 32 signals differs from the one of the 44 signal. This difference hints to a different electrolyte

molecule being the origin of these signals. Besides that, the measurements show no significant increase in m/z 32, which means that no O_2 evolution can be detected. However, for the $LiPF_6$ fragments (m/z 85, 104) a potential dependent behaviour was observed. At potentials higher than 3.8 V the decomposition of $LiPF_6$ occurs, with a peak at the upper potential limit.

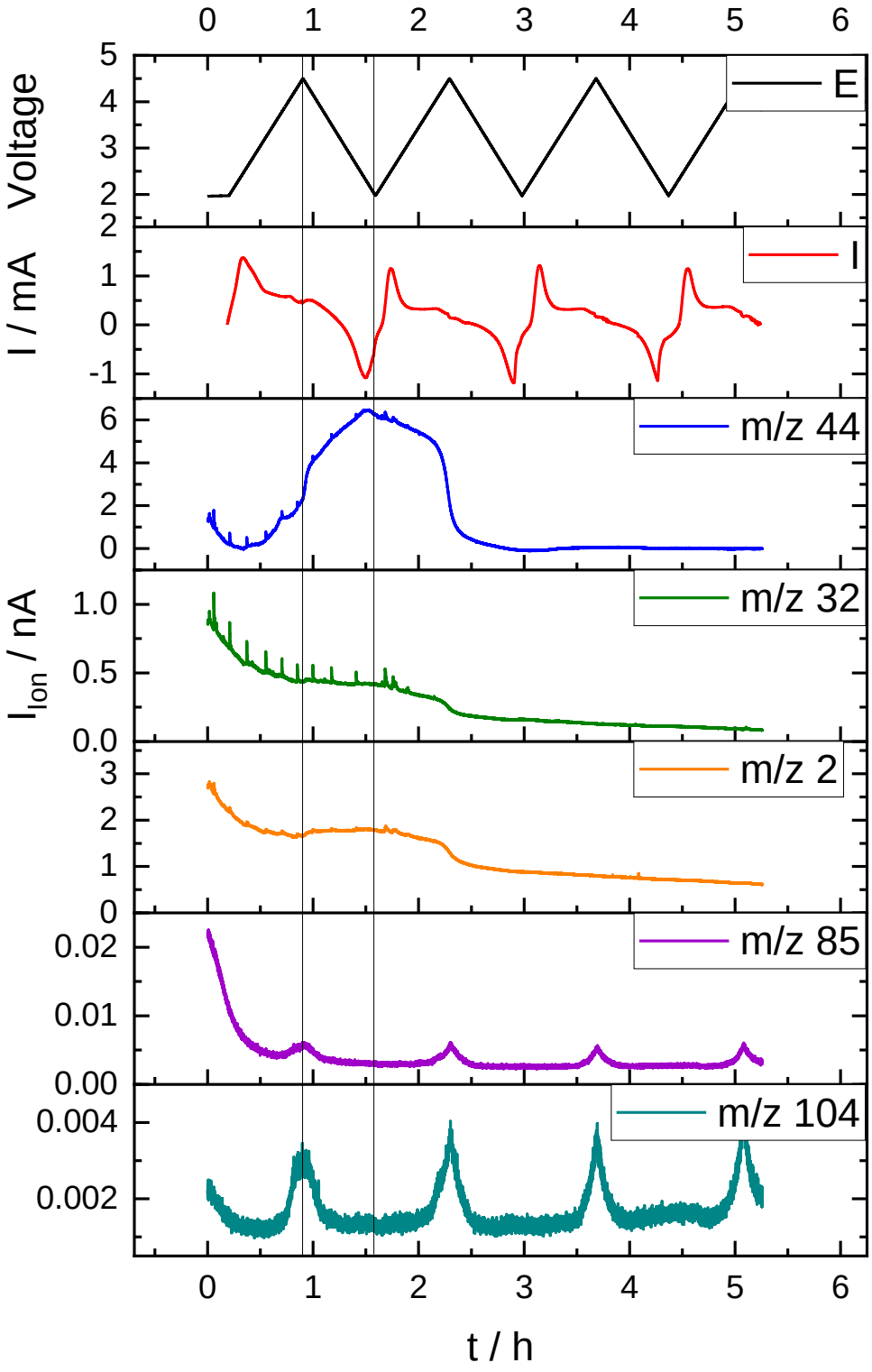


Figure 8: Potentiodynamic DEMS measurements in the membrane-free Swagelok-cell with a $LixVO_2F$ electrode in LP30 electrolyte (scan rate 10 mV s^{-1}): applied potential and selected ion current responses as indicated.

The background signal in the membrane-free Swagelok cell setup may be too high to detect small volumes of O_2 which evolve during cycling. Additionally, battery materials are usually cycled with orders of magnitude slower scan rates. For this reason, the membrane Swagelok cell was used for measuring the same electrode material at a scan rate of 0.2 mV s^{-1}. The used membrane is impermeable for electrolyte molecules. This not only enables measurements without cell dry-out but also reduces the background signal of the electrolyte fragments. In contrast to the electrolyte molecules, O_2 molecules are small enough to diffuse through the membrane. Therefore also small volumes of O_2 can be detected during measurement.

In Figure 9 the applied cell potential, the Faradaic current and the simultaneously measured ion current traces of m/z 44, 27, 28, 15 and 32 are shown. In the anodic scan, a peak in the ion current of m/z 32 is observed between 3.2 and 3.6 V, which does not correlate to other signals. The independence to other peaks is an indication that this peak is only influenced by one fragment and can therefore be attributed to the formation of O_2. However, O_2 evolution only occurs during the first cycle and at much lower potentials than it was observed on LNMO-based electrode materials.[78] For the following cycles no indication for further O_2 evolution is observed in the anodic scan. Therefore, I assume that the O_2 evolution during the first anodic scan is caused by (unknown) impurities which are oxidized in the first cycle, releasing only O_2 as a volatile species. Also the partial decomposition of electrode components cannot be excluded. Comparing the measurements in Figure 8 and 9, the differences in the height of the Faradaic currents are expected due to the different loading and different scan rate. Not expected is the difference in the shape of the faradaic current: in the membrane-cell an additional peak appears between 3.5 and 4 V, thus after the O_2 increase. However, the faradaic current peak only appears in the membrane containing DEMS cell. There are different possibilities for the origin of the peak: i) different electrode composition than in the other measurement of the membrane-free cell, ii) some contaminations / systematic failures in the membrane-cell or iii) reaction of the active electrode material with the conductive aluminium layer sputtered on the membrane. The second option was tested using the open beaker cell, which is described in section 2.1.2, in a glovebox. For this measurement also the peak between 3.5 and 4 V appears which indicates that a systematic failure in the Swagelok-cell is not responsible for the appearance of the peak in the Faradaic current. The same electrode material which was coated on the membrane was also used for other measurements published in reference [92] and showed no additional feature during charging. Thus, the remaining third option seems to be the most likely one. Unfortunately,

this cannot be avoided for low-background measurements in the current type of membrane-cell.

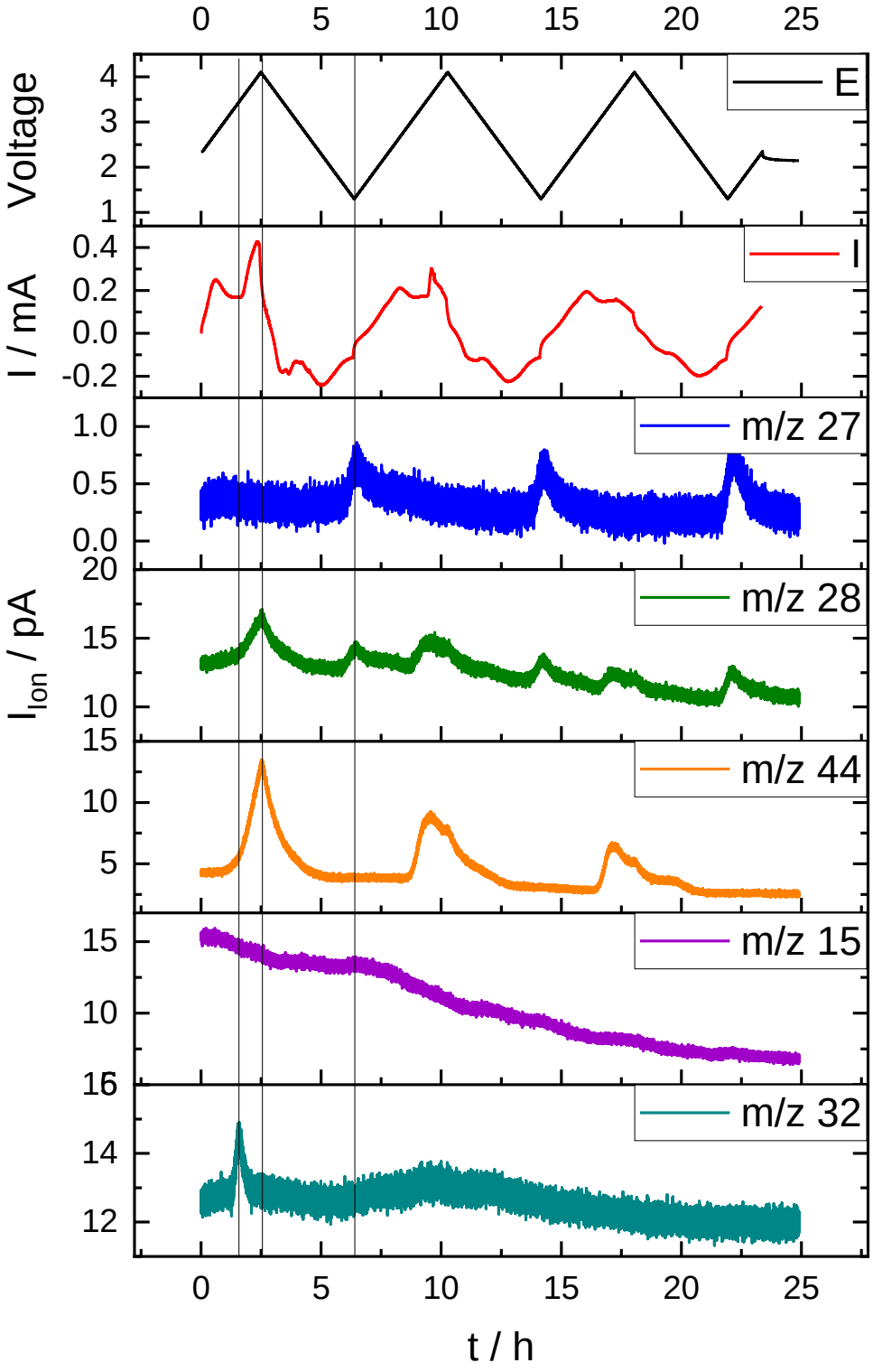


Figure 9: Potentiodynamic DEMS measurements in the membrane Swagelok-cell with a Li_xVO_2F electrode in LP30 electrolyte (scan rate 0.2 mV s^{-1}): applied potential and selected ion current responses as indicated.

Having a look at the other m/z ratios in the first anodic scan, the ion currents of m/z 44 and 28 which are related to CO_2 (44, 28) and CO (28), respectively, increase in parallel at potentials

above 3.0 V. The shapes of both peaks around the upper potential limit seem to be similar, which points for the same origin (CO_2) of both fragments. However, the expected ratio of the 44 to 28 signals is around 10:1 according to NIST database.[106] The MS used for the present measurements is optimized for low ionization energies, resulting in low fragmentation of products and we would expect even less CO being formed in the ion source. Therefore, the resulting ratio of 2:1 between the ion currents of 44 and 28 in Figure 9 hints for the parallel (electro-)chemical formation of CO_2 and CO. Additionally, the peak-shape changes between the first and following cycles (similarly for both m/z = 44 and 28). There are two possible sources for CO and CO_2 during the first and following cycles: i) decomposition of residual Li_2CO_3 which is inevitably present as a contaminant on transition metal oxide surfaces, which can chemically react and release CO_2 or ii) the decomposition of the carbonate electrolytes.[108] For the latter option, from our measurement we cannot decide if the different peak-shapes between the first and the other cycles are related to the pronounced decomposition of the electrolyte in the first cycle, forming an interfacial layer between the electrode and the electrolyte (EEI), resulting in a different decomposition mechanism in the following cycles, or whether it is caused by decomposition of residual Li_2CO_3 from synthesis.

Combining the results with those from the Swagelok-cell without inserted membrane (Figure 8), we see that the increase of m/z 28 and 44 starts in parallel to the $LiPF_6$ decomposition. This is an indication for the electrolyte decomposition starting at 3.2 V. Also DEMS measurements from Cambaz et al. using the same electrode material found CO and CO_2 fragments at positive potentials and therefore concluded that the electrolyte decomposition starts at 3.6 V in galvanostatic measurements.[109] However, from the measurements shown by Cambaz et al. it cannot be excluded that some share of the m/z 28 and 44 signals originate from Li_2CO_3 surface contaminations.

In the cathodic scan, at the lower potential limit, we find an additional peak at around 1.5 V for m/z 28, which is not observed for m/z 44, but for m/z 27, instead. The ratio between the m/z 28 and 27 signals is about 0.6, which fits to the expected fragmentation of ethylene. The latter can be formed by the electrochemical decomposition of the electrolyte. In the measurements by Cambaz et al., also a peak in the m/z 28 is visible at around 1.5 V.[109] Unfortunately, m/z 27 is not shown in the publication by Cambaz et al.. Therefore we can only speculate about the formation of ethylene in their measurement. In our measurements also the m/z 15 ion current shows a significant, potential independent decrease which can mainly be attributed to changes in the partial pressure of dimethyl carbonate. Small changes in the signal might be induced by a potential dependent rate of DMC decomposition. The m/z

ratios of 85 and 104, as indicators for $LiPF_6$ decomposition, were measured as well, but are not included in Figure 9 as there are no changes of the ion current visible during the measurement. This might be due to the relatively large size of the decomposition products, which cannot diffuse through the membrane and can therefore not be detected by the MS.

3.1.3 Summary

As a result, the observed fragments for both Swagelok-cells give insight into the potential dependent formation of decomposition products. The membrane-cell enables the detection of only small amounts of small decomposition products. In this set-up, some O_2 release was detected during the first anodic scan. Due to the appearance of the peak at rather low potentials, the O_2 evolution might originate from the oxidation of impurities or decomposition of electrode components in the first anodic scan, resulting in O_2 release. The subsequent cycles showed no additional O_2 signal, which indicates that the electrode material remains stable after the first charging. The electrolyte decomposition products were detected both at the upper and lower potential limits. In the negative scan below 1.5 V the formation of ethylene was observed, whereas at positive potentials above 3.2 V CO_2 formation was monitored in the membrane-cell. The membrane-free cell, however, showed the formation of $LiPF_6$ decomposition products, which were not observed in the membrane cell. This indicates that for a detailed insight in reaction mechanisms, the combination of the results of both cells is necessary.

Therefore, it has been shown that the results of DEMS measurements are highly dependent on the design of the electrochemical cell, i.e. if a membrane is included or not.

3.2 A Novel Approach for Differential Electrochemical Mass Spectrometry Studies on the Decomposition of Ionic Liquids

The content in this section was published in Ref. [110] and is reproduced and adapted with permission from Journal Electrochimica Acta / ©2016 Elsevier Ltd. (Electrochim. Acta 2016, 197, 290-299 / 10.1016/j.electacta.2015.12.226). The experimental section was removed and the information was added to the experimental part in chapter 2 of this work. The style and numbering of the references and the figures have been adapted to fit the layout of the thesis. The measurement setup was developed by the author of this thesis, Johannes Schnaidt, Zenonas Jusys and Yeuk-Ting Law. The electrochemical measurements and the data evaluation were conducted by me. Furthermore, I was strongly involved in the creative process of the publication. This work was supported by the German Federal Ministry of Education and Research (project "Perspektiven für wiederaufladbare Mg-Luftbatterien", contract number 2E2-ESP350).

3.2.1 Abstract

We report on a novel differential electrochemical mass spectrometry (DEMS) set-up, which allows us the online detection of volatile products formed during potential induced decomposition of ionic liquids, and its application for elucidating the decomposition mechanism of the two ionic liquids (ILs) 1-butyl-1-methylpyrrolidinium bis(trifluoromethanesulfonyl)imide (BMP-TFSI) and 1-ethyl-3-methylimidazolium bis(trifluoromethanesulfonyl)imide (EMIM-TFSI) on polycrystalline Au electrodes. In the cathodic scan, the BMP^+ cation decomposes at potentials more negative than -1.0 V vs. Ag/AgCl by cleaving the butyl side chain; below -2.6 V also ring opening takes place. For EMIM-TFSI reduction, we find a decomposition product which based on its mass is compatible with a stable imidazolium radical appearing at -2.3 V, accompanied by its saturated derivative. In the anodic scan the $TFSI^-$ anion is decomposed first for both ILs, possible decomposition products are discussed.

3.2.2 Introduction

Ionic liquids are considered to be promising electrolytes for future battery applications due to a number of favorable properties such as high ionic conductivity, very low vapor pressure, low flammability, and high thermal and electrochemical stability.[1,111-114] Since the

electrochemical stability of ILs plays a key role for their use as battery electrolytes, it is interesting to study their electrochemical decomposition.

The electrochemical stability window, i.e., the potential difference between onset of the cathodic and anodic decomposition of the IL, is usually examined by cyclic voltammetry.[115] It is generally accepted that in most ILs the cathodic limit is determined by the onset of the reduction of the cation, while the anodic limit is set by the oxidation of the anion.[25,33,43,115-118] This conclusion is based on the comparison of the onset potentials for the anodic/cathodic decomposition of different combinations of cations and anions in ILs and on calculated values of the HOMO and LUMO energies.[46,115,119] Though appearing reasonable, direct experimental proof for this assignment is largely missing.

This general problem is topic of the present work, where we want to gain closer insight on the stability and decomposition behaviour of ILs by *in situ* determination of the volatile products formed during the decomposition reaction. Differential electrochemical mass spectrometry (DEMS) is known as a powerful method for the online detection of volatile reaction products,[69] but commonly used set-ups developed for aqueous electrolytes, where a porous, hydrophobic membrane serves as interface between the electrochemical cell and the differentially pumped vacuum system housing the mass spectrometer, are for several reasons not suitable for operation with ILs, among others because of the high viscosity of the ILs and the low permeability of the membrane for larger molecules. Furthermore, a flow cell set-up as developed and generally used in our institute [70] is inappropriate because of its high consumption of expensive IL electrolyte. Mass spectrometry set-ups developed for battery related research with non-aqueous electrolytes either use gas purging [76,120] or a leak valve [121] to transport the volatile products to the analysis chamber. We here report on the development of a new set-up, where we make use of the extremely low vapour pressure of the ILs. This allows us to operate without a separating membrane or any capillary inlet system, by placing the open electrochemical cell directly into the vacuum chamber of the mass spectrometer. This approach also offers the advantage of characterizing the IL under "ideal" conditions, minimizing the effects of impurities such as water, oxygen or even nitrogen.

This set-up is employed to investigate the decomposition behaviour of the two ILs BMP-TFSI and EMIM-TFSI during potential scans on polycrystalline Au electrodes. BMP-TFSI is one of the most promising ILs for the use in batteries due to its especially wide electrochemical window and its hydrophobicity and stability against atmospheric influences, in particular against exposure to water vapour and air.[47,122-124] Before starting with the description of the

DEMS set-up and the presentation and discussion of the results, we will briefly summarize the results of previous studies relevant for this work.

Assuming that decomposition of BMP-TFSI at too high cathodic potentials proceeds via reduction of the BMP^+ cation which takes up an electron, Kroon et al. performed quantum chemical calculations to calculate the stability of the resulting BMP radical.[46] They found that the radical is not stable and decomposes into a smaller radical and a neutral fragment. The calculated relative energies of possible decomposition products, relative to that of the initial molecule, indicated that the formation of methylpyrrolidine and of a butyl radical is the most probable initial decomposition step. Two additional decomposition routes, which are also possible based on their energetics, were the formation of a dibutylmethylamine radical via ring opening or of a butylpyrrolidine and of a methyl radical. Such products were indeed found by *ex situ* GC-MS after extensive decomposition of BMP-TFSI on glassy carbon electrodes.[46] In contrast, Howlett et al. concluded from electrochemical and IR spectroscopic measurements that the $TFSI^-$ anion in a comparable IL (1-propyl-1-methylpyrrolidinium, PMP-TFSI) is reductively decomposed already at potentials positive of the onset of massive PMP^+ cation reduction.[35] They proposed a decomposition mechanism based on *ab initio* calculations. Furthermore they found that the $TFSI^-$ reduction depends sensitively on the water content of the IL. Endres et al. also observed cathodic peaks before the onset of massive BMP-TFSI decomposition,[33,117] which according to Howlett et al. [35] were also due to $TFSI^-$ decomposition. From *in situ* STM measurements, Endres et al. concluded that the $TFSI^-$ breakdown products are loosely adsorbed on the Au surface and soluble in the IL.[33] Markevich et al.[125] concluded from stepwise electrochemical decomposition and IR measurements of the volatile reaction products after each step that the decomposition of the cation as well as the anion takes place at cathodic potentials. However, it is unclear, if and how a separation between the products formed at the CE and the WE was achieved It is well known, that impurities influence the stability of ILs.[126-130] The influence of especially water and oxygen traces on the stability of BMP-TFSI towards cathodic decomposition was studied in more detail by Randström et al. employing cyclic voltammetry.[34,131] While in the presence of water traces similar features in the voltammogram were observed according to Endres et al. and Howlett et al.,[33,35,117] the former authors did not find any voltammetric features indicating the reduction of the $TFSI^-$ anion in pure and dry BMP-TFSI before the onset of massive electrolyte decomposition.[131] Furthermore, comparing measurements performed under N_2 or Ar purging and measurements under vacuum they found that even the presence of N_2 leads to an additional cathodic process.[34]

To gain more insight into the correlation between structure and reactivity, we also investigated the decomposition of a closely related second IL, which contains same anion but a different cation. We chose EMIM-TFSI, which in contrast to BMP-TFSI has an aromatic, imidazolium based cation. Investigations of Xiao et al. on Pt and Kroon et al. on Au working electrodes (WEs) in a comparable aromatic IL (1-butyl-3-methylimidazolium tetrafluoroborate – BMIM-BF_4), using NMR spectroscopy for product analysis, led to the conclusion that reduction of $BMIM^+$ results in the formation of the related carbene and molecular hydrogen ($^1/_2$ H_2),[132] or via a disproportionation reaction in the above carbene and the related hydrogenated species.[46] In addition, Kroon et al. showed by quantum chemical calculations that a BMIM radical formed in the first reduction step would be stable in vacuum.[46]

In the following we will first describe the new experimental set-up and the experimental procedures in chapter 3.1.2. This will be followed by the discussion and comparison of the decomposition behaviour of BMP-TFSI (section 3.1.3.1) and EMIM-TFSI (section 3.1.3.2), demonstrating the insight accessible from such kind of measurements.

3.2.3 Results and Discussion

3.2.3.1 BMP-TFSI

To gain an overview about the cathodic and anodic processes and for comparison of our measurements with previous studies on the interaction of BMP-TFSI with a Au electrode,[33,117,123,133] we show a CV (Figure 9) of polycrystalline Au in BMP-TFSI, which ranges from -3.2 to 2.9 V vs. Ag/AgCl. At the limits of the potential window, the Faradaic current increases exponentially. For determining the electrochemical stability window of the IL we follow the definition given by Endres et al.[123]

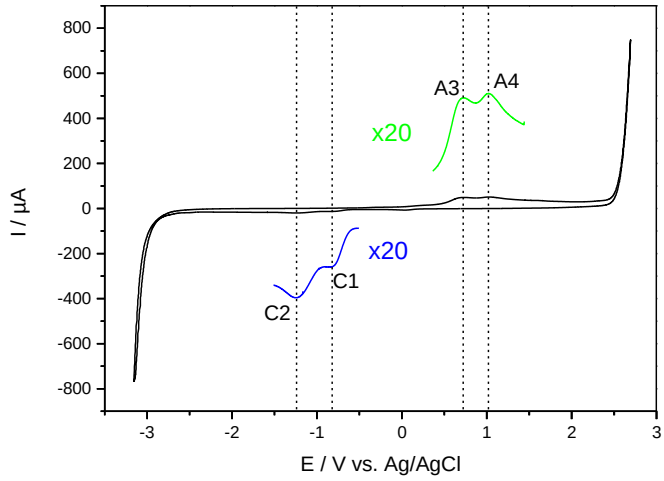


Figure 10: Cyclic voltammogram of polycrystalline Au in BMP-TFSI (scan rate 10 mVs^{-1}).

According to these authors it is determined by linearly extrapolating the cathodic and anodic currents at the cathodic / anodic limits of the scanned potential range to zero. This results in a stability window ranging from -3.0 to 2.6 V for BMP-TFSI. Additionally we observed two peaks (C1 and C2) at -0.8 and -1.2 V in the cathodic scan. Peaks in the cathodic scan of BMP-TFSI and PMP-TFSI, which are frequently discussed in the literature, were reported to occur in a region between -0.35 and -1.7 V vs. Pt,[133] in the range from -2.0 to -2.5 V vs. Fc/Fc^+ [33,35,123,134] or finally in the potential range between -1.0 and -1.5 V vs. Ag.[135] Hence, there seems to be agreement on the observation of additional peaks in the cathodic scan before the onset of massive decomposition. The exact position of these peaks, however, is not well defined. In addition to problems associated with the potential conversion between different (quasi-)reference electrodes, it apparently depends also on the purity of the respective system. Furthermore, also the interpretation of the physical origin of the different peaks and the underlying processes varied. By some authors, they were assigned to adsorption and restructuring / reordering processes of the BMP^+ adlayer / molecules at the surface of the Au electrode.[33,123,133,134] In contrast, Howlett et al. proposed that in PMP-TFSI these peaks result from the decomposition of the $TFSI^-$ anion.[35] It was also speculated by Lane[127] that the potential of these peaks matches the expected potential of the intercalation of tetraalkylammonium ions into certain metal electrodes.

Going to the anodic scan, we also observed two peaks (A3 and A4) in the potential region between 0.9 V and 1.3 V. In a previous study, peaks at these potentials were assigned to the oxidation of products formed during the decomposition of the cation in the preceding cathodic scan.[123]

To further clarify the origin of the peaks and to gain insight to the decomposition behaviour of anion and cation, we combined the electrochemical measurements with online mass

spectrometry (MS) detection. This allows a potential resolved detection of the volatile decomposition products of the IL generated at the electrified Au surface of the WE.

Figure 10 thus shows the background subtracted MS scans measured in parallel to the Faradaic current during a linear potential scan. The spectra are plotted against the potential. 32 spectra were recorded during 1 V of the potential scan. For a better picture, the number of spectra depicted in Figure 10 is reduced by only showing the average of two consecutive spectra. In order to not miss any fragments created during the potential ramp we scanned the full range of the MS of m/z 0 – m/z 300. In Figure 10 we only present those regions of the spectra where ion current signals developed during the potential scan. A full spectrum is provided in the supporting information.

The ion current signals related to the residual gas in the chamber, mainly water, nitrogen and hydrocarbons, appear as potential independent, fluctuating peaks in the spectra. The first signals related to the IL decomposition appear at a potential of -1.0 V vs. Ag/AgCl at m/z 42, 57 and 84 (blue arrows). To better resolve the evolution of these peaks at very low intensities, the signals were magnified (factors see Figure 10) in the potential regime between -1.0 and -2.0 V.

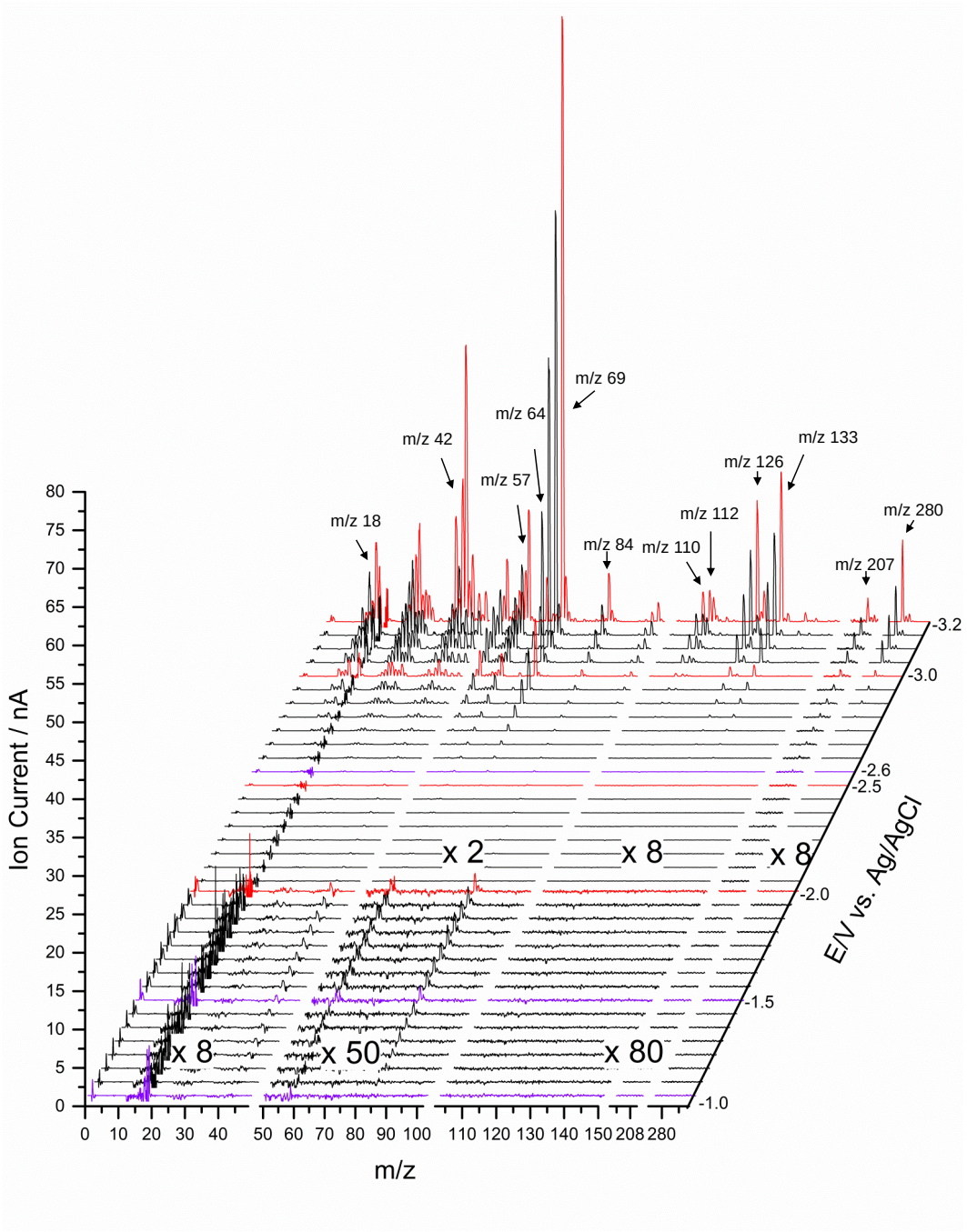


Figure 11: Sequence of mass spectra following the cathodic decomposition of BMP-TFSI during the first cathodic potential scan, plotted against the potential (scan rate 10 mVs^{-1}). The spectra cover the range 0 < m/z < 300, regions with no signals appearing are cut. The spectra marked red indicate potential steps of 0.5 V, the purple lines indicate potentials explicitly mentioned in the text.

The simultaneous evolution of these mass signals is more clearly resolved in Figure 11, which shows the Faradaic current at the WE and the ion current traces of the most intensive / significant signals (see Figure 10) of the decomposition products plotted against the potential. First of all these current traces show a low constant current for the fragments with m/z 42, 57 and 84 between -1.5 and -2.6 V. The finding of a current plateau instead of an exponential increase as observed at more negative potentials appears surprising. This could be due to a passivation process taking place at the electrode with the decomposition products inhibiting

further reaction. As will be discussed below, SEI formation via decomposition of ILs was reported on various electrodes.[125,136-139] Another possible explanation would be that the current is related to the reduction of impurities (possibly methylpyrrolidine residues from the synthesis) and therefore is diffusion limited by their low concentration. We slightly favor the former explanation since we did observe the phenomenon with two different batches of BMP-TFSI.

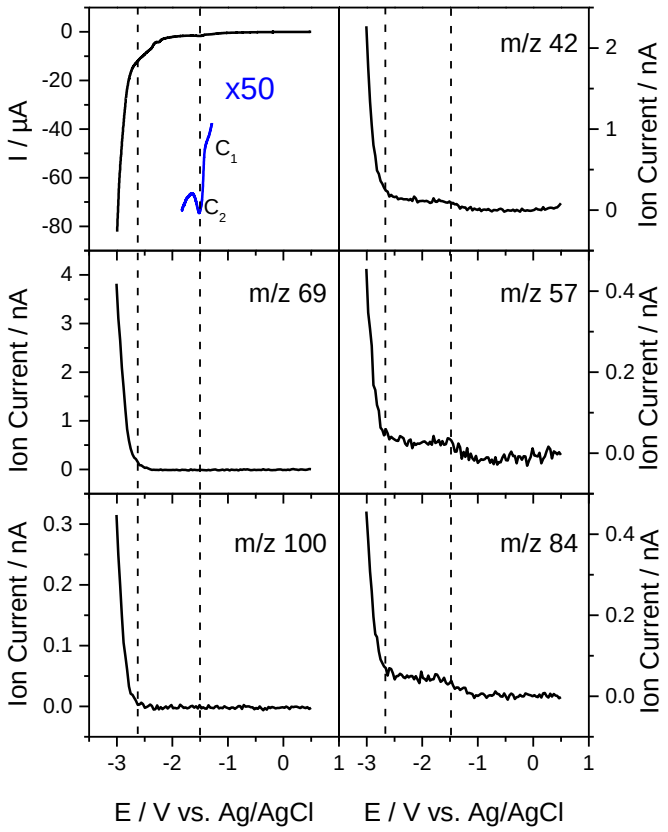


Figure 12: Faradaic current (top left) and ion currents (m/z = 42, 57, 69, 84 and 100, see figure) recorded during the first cathodic potential scan in BMP-TFSI (scan rate 10 mV s 1).

For potentials more negative than -2.6 V, all ion currents and the Faradaic current increase exponentially. The m/z 42, 57 and 84 species were reported to be the main fragments of methylpyrrolidine,[140] indicating that methylpyrrolidine is formed upon reduction of BMP^+ by breaking the bond between the ring and the butyl side chain.

It should also be noted that Duffield et al. found about similar intensities for these fragments, whereas in our measurements the signals of m/z 42 and 57 appear with a higher ion current than that at m/z 84. The higher intensities of the former signals may be due to contributions from the butyl side chain which has been split off ($C_3H_6^+$, $C_4H_9^+$). These results agree with the findings of Kroon et al.,[46] who investigated the decomposition behaviour of the BMP^+ cation

by a combination of quantum chemical calculations and electrochemical measurements. These authors reported that massive electrochemical decomposition of the IL was achieved when applying a potential difference of 8 V between two glassy carbon electrodes for 3 h. Afterwards they extracted the decomposition products with toluene and analyzed them by GC-MS [46]. They state that a one-electron process takes place at the cathode, generating a radical from the BMP^+ cation. Based on their calculations the radical is not stable and decomposes rapidly via three different decomposition routes. The most probable route proceeds via the formation of methylpyrrolidine and a butyl radical. The second favored mechanism leads to N-butyl-N-methylbutan-1-amine via a ring opening reaction, the third and most unlikely one involves the elimination of the methyl group. In their GC-MS measurements they found fragments which are in agreement with all three of the decomposition routes. Considering that we only detect fragments related to the formation of methylpyrrolidine and a butyl moiety, our measurements indicate that at potentials higher than -2.6 V only the first decomposition route is active.

In parallel to the appearance of signals in the MS spectra (Figures 10/11), there is a small cathodic peak in the Faradaic current at -1.5 V vs. Ag/AgCl. As discussed above (see Figure 9), residual water in the IL has been proposed as origin of Faradaic current peaks in this potential regime.[34,35,131] Also structural changes in the BMP adlayer were reported to occur in this potential range, as evidenced by high-speed *in situ* scanning tunneling microscopy.[133] The observation of decomposition products of the BMP^+ cation at said potential might be interpreted such that the Faradaic current peaks are due to the BMP^+ decomposition. However, considering the very different peak shape in the Faradaic current trace and in the ion currents of m/z 42, 57 and 84, which only show a slight increase of the signal at this potential, it is questionable whether and in how far these different features are correlated. In that case it remains open whether the structural changes observed by Wen et al. are induced by the beginning of BMP^+ decomposition, and whether and in how far this is influenced by residual amounts of water in the IL. We have no evidence, however, that these peaks are related to the decomposition of $TFSI^-$ anions, as it had been suggested by Howlett et al.[35]

At potentials more negative than -2.6 V additional peaks develop in the scans in Figure 10. A peak at m/z 100 is attributed to the formation of N-butyl-N-methylbutan-1-amine (main fragment: M = 100 $gmol^{-1}$ [141]). Thus, at this potential we can also observe the ring opening as proposed by Kroon et al.[46] Further peaks with m/z values between 12 and 59 represent the typical fragmentation pattern of various hydrocarbons in the ion source of the MS.[142] This fragmentation hampers a clear assignment to specific molecules originating from the

electrochemical reaction, therefore it remains unclear to which extent and in which way the carbon chains are decomposed during the electroreduction.

At these potentials also the ion current signals at m/z 64, 69, 133 and 280 (red arrows) rapidly increase in intensity, with m/z 69 even surpassing the signal of m/z 42. The ion currents of m/z 64 and 69 are most plausibly assigned to CF_3^+ and SO_2^+ fragments of the $TFSI^-$ anion, respectively. The signal m/z 133 seems to result from $SO_2CF_3^+$, whereas m/z 280 is attributed to the molecular ion of $TFSI^-$. While the intensity of these peaks increases with decreasing potential, their ratio does not change with decreasing electrode potential, indicating that the peaks result from the fragmentation of intact TFSI molecule ions in the ion source of the MS. Another possible explanation could be that the selectivity of the electroreduction of $TFSI^-$ towards the formation of CF_3, SO_2 and SO_2CF_3 moieties is independent of the electrode potential.

The finding of $TFSI^-$ decomposition products at such negative potentials appears surprising, since the anion should be repelled from the cathode surface. A possible way for the $TFSI^-$ decomposition might be the attack by reactive reaction intermediates (radicals) formed by the BMP^+ reduction. An alternative explanation would be a direct electrochemical reduction of TFSI. This is supported by molecular dynamics and density functional theory calculations from Ong et al.[129] on the very similar IL PMP-TFSI. Since the calculated density of states indicates that the lowest unoccupied molecular orbital (LUMO) is dominated by the anion, they conclude that the $TFSI^-$ anion is even less stable against reduction than the PMP^+ cation (which is very similar to the BMP^+ cation used in the present study). However, the calculated difference in cathodic stability between PMP^+ and $TFSI^-$ becomes smaller when Ong et al. apply a polarizable continuum model. In another computational study, Tian et al.[143] calculated that the reduction of both, the anion and the cation take place at very similar potentials. They assume depending on the experimental conditions either the cation or the anion decomposition could start at less negative potentials.

There are also numerous experimental studies reporting the $TFSI^-$ decomposition at cathodic potentials in various $TFSI^-$ containing electrolytes, evidenced by both the formation of volatile $TFSI^-$ decomposition products and the finding of $TFSI^-$ decomposition products in electrode surface layers. Studying the volatile reaction products via IR spectroscopy, Markevich et al.[125] showed for Li(TFSI) containing BMP-TFSI on Li and graphite surfaces, that the anion as well as the cation break down at cathodic potentials, especially on the Li surface. In contrast to Howlett et al., which claimed that the cleavage of the N-S bond is the first step,[35] Markevich et al. proposed that the breaking of the S-C bond is the first reduction step. They also

demonstrated, that the electrode material plays an important role since the graphite surface shows a catalytic activity in the reductive decomposition of BMP^+, occurring along the BMP^+-intercalation into graphite.[125]

Xiong et al.[136] observed by XPS measurements a SEI consisting manly out of anion decomposition, for BMP-TFSI electrolytes with and without polysulfides, which they conclude is being formed via the decomposition mechanism proposed by Markevich et al.[125]

In contrast to this Nguyen et al.[137] reported that the first step of the $TFSI^-$ decomposition is most likely the cleavage of the C-F bond and the formation of LiF in the solid electrolyte interphase (SEI). This was found for Li(TFSI) solutions in PMP-TFSI on an amorphous silicon-copper electrode, studied by ex situ ATR FTIR spectroscopy and XPS,

Further investigations of the SEI were performed by Howlett et al.[139] who used XPS, FTIR, Raman and EIS techniques. They investigated Li(TFSI) solutions in the ILs BMP-TFSI and PMP-TFSI. The SEI consists mainly of salts composed from decomposition products of the anion and Li^+ (e.g. LiF, Li_2O, $LiSO_3CF_3$). Next to that they also found some hints for the IL cation or its decomposition products being present in the SEI layer, which could either be due to cation reduction or due to the cation being trapped in the anion decomposition products.[139]

These results fit quiet good to the observations of Aurbach et al.[138] They investigated the behaviour of Li(TFSI) solutions in aprotic organic solvents and found $TFSI^-$ decomposition products via IR spectroscopy on Pt and Ni electrodes.[138]

However, in contrast to the measurements stated above, in our experiments a model system with neat ILs without any Li^+ ions on a noble metal (Au) electrode was used. The influence of different experimental conditions such as the nature of the electrode and the presence of other electrolyte components have to be considered, when comparing our model studies to real battery systems. As showed before, under our experimental conditions we first detect volatile decomposition products related to the cation reduction, so it appears that BMP^+ is reduced first. Our experimental observations that at more negative potentials products of both, anion and cation decomposition are detected, fit well to the theoretical predictions[129,143] and the experimental findings of cathodic TFSI decomposition named above.[125,136-139]

In addition to the peaks discussed so far, also peaks at m/z 110, 112, 126 and 207 develop, which so far could not be unambiguously identified yet. Especially for m/z 207, which is heavier than the molecular ion of BMP and cannot be a simple fragment of TFSI, we assume that some new bonds must have formed. All ions which are explained above and the assigned fragments are listed in Table 1.

Table 1: Assignment of the m/z values to possible fragments of BMP-TFSI.

m/z	Ion	Origin
2	H_2^+	BMP
28	$C_2H_4^+$, CH_2N^+, N_2	BMP
42	$C_2H_4N^+$	BMP
57	$C_4H_9^+$, $C_3H_7N^+$	BMP
84	$C_5H_{10}N^+$	BMP
100	$C_6H_{14}N^+$	BMP
64	SO_2^+	TFSI
69	CF_3^+	TFSI
133	CF_3SO_2	TFSI
280	$(CF_3SO_2)_2N$	TFSI

The Faradaic current signal during an anodic scan (first scan) in BMP-TFSI is shown in Figure 12, together with the ion current signals of m/z 42, 57, 64, 69, 84 during a linear potential sweep from -0.5 to 2.9 V. The respective MS scans between m/z 0 and 300 are available in the supporting information. Except for the anodic breakdown there is no characteristic feature visible in the Faradaic current. Compared to the full CV in Figure 9, where the positive going scan followed a preceding cathodic scan, the two peaks A3 and A4 that were found the latter case are absent here. This confirms that these peaks result from a further oxidation of decomposition products formed during the cathodic decomposition of the IL in the preceding cathodic scan, as it was already reported by Atkin et al. [33]. The signals of m/z 64 and 69, which can be correlated to the SO_2^+ (M = 64 gmol^{-1}) and CF_3^+ (M = 69 gmol^{-1}) fragments, increase immediately with the onset of the Faradaic current at 2.2 V. Also at m/z 133 and 280 signals develop (not shown, see supporting information). This demonstrates that the $TFSI^-$ anion is decomposed at anodic potentials. This result fits to the theoretical predictions of Ong et al.[129] who found employing a polarizable continuum model that the $TFSI^-$ anion should be oxidized first at anodic potentials; however, there are only small differences in the potentials of the oxidation of the PMP^+ cation and the anion.

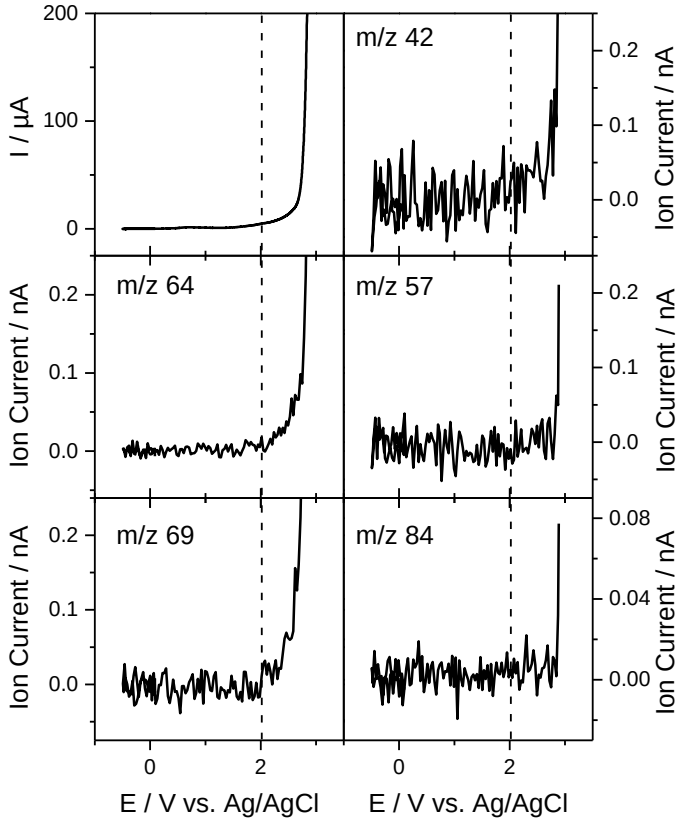


Figure 13: Faradaic current (top left) and ion currents (m/z = 42, 57, 64, 69 and 84, see figure) recorded during the first anodic potential scan in BMP-TFSI (scan rate 10 mVs^{-1}).

Similar to the cathodic scan, the ratio between the TFSI fragments is constant, independent of the applied potential. Moreover, the ratios are similar to those during the cathodic scan. To our belief this further supports the explanation that these signals arise from the fragmentation of intact TFSI (possibly volatile neutral TFSI radicals formed by removing an electron from $TFSI^-$) in the ion source. Although we cannot rule this out, a $TFSI^-$ decomposition reaction with similar product distribution independent of the potential and both at cathodic and anodic potentials appears unlikely. This would require that at cathodic potentials $TFSI^-$ is oxidized by chemical reaction with reactive BMP^+ reduction intermediates (radicals), forming a volatile TFSI radical.

At potentials more positive than 2.5 V also the evolution of BMP^+ fragments takes place. This is the reverse finding of the processes during the negative scan. Hence, at moderate cathodic or anodic potentials, first the cation (cathodic scan) or the anion (anodic scan) is electrochemically decomposed, followed at more extreme conditions by the decomposition of the respective counter ion.

In summary, the results presented for the electrochemical decomposition of BMP-TFSI show that at anodic potentials the anion is decomposed forming a neutral volatile TFSI species,

while at cathodic potentials the cation is decomposed, predominantly by splitting the bond between the butyl side chain and the ring. At the highest potentials, both anodic and cathodic potentials, fragments of both ions can be detected.

3.2.3.2 EMIM-TFSI

The interaction of EMIM-TFSI with a polycrystalline Au electrode was investigated in the same way as described above for BMP-TFSI. Figure 13 shows the CV of EMIM-TFSI on a polycrystalline Au electrode, providing an overview of the cathodic and anodic processes. In the anodic and cathodic scan the peaks E2 (E < -2.2 V) and D3 (E > 2.2 V) are due to the massive decomposition of the IL. The peaks D1 and D2 at 1.3 and 1.7 V in the anodic scan, are associated with the dissolution of relatively weakly bound gold at defects and step edges, as had been proposed by Atkin et al.,[33] who had studied the interaction of same IL with Au(111) electrodes. However, since we do not observe the peaks D1 and D2 without a preceding potential excursion to the cathodic EMIM-TFSI decomposition, we conclude that both peaks are related to the oxidation of products formed in a preceding cathodic scan at E2. For peak E1 in the cathodic scan there is no equivalent in the CV presented by Atkin et al. However, the peak is increasing with continuous cycling which leads to the assumption that this peak is due to the further reduction of products formed in the anodic scan before.

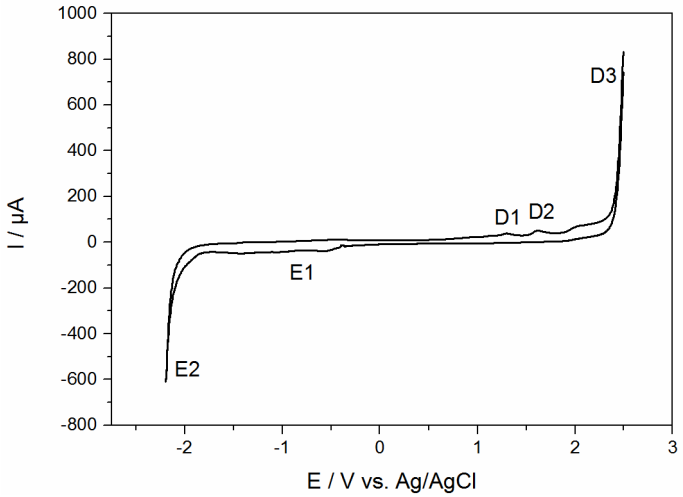


Figure 14: Cyclic voltammogram of polycrystalline Au in EMIM-TFSI (scan rate 10 mVs^{-1}).

Next we present (background subtracted) mass spectrometric scans recorded during the first cathodic scan in Figure 14. Similar to Figure 10 fluctuations in the residual gas spectrum (e.g., at m/z 2, 18, 28) result in fluctuating peaks of the respective masses in the background corrected spectra in Figure 14. The ion current of m/z 2 shows an additional potential dependent increase, which means that at potentials more negative than -1.75 V the signal

includes increasing contributions from reaction products. Figure 15 shows the Faradaic current and the ion currents of the masses m/z 64, 280, 69, 83 and 111, which are the most prominent and informative signals developing in the MS measurements, plotted against the potential at the WE. All ion currents which start to increase at a potential more negative than -1.75 V, parallel to the steep increase of the Faradaic current, can be correlated with the decomposition of the cation. Several peaks around m/z 18, 28, 42 and 58 starting at that potential lead to the assumption that the main fragment at these masses contains more than one hydrogen atom, which can be removed during ionization in the MS. Following this argument, following assignments are possible: m/z 18: H_2O, m/z 28: $C_2H_4^+$, m/z 42: $C_2H_6N^+$ and m/z 58: $C_2H_6N_2^+$. Other mass signals starting at this potentials are m/z 83, 96, 110, 111 and 112, where m/z 83 is correlated to $C_3H_7N_2$, i.e., an $EMIM^+$ cation without the ethyl group, and m/z 96 to $EMIM^+$ without the methyl group ($C_5H_8N_2$).[144] The signal at m/z 111 can be directly correlated with the $EMIM^+$ cation (M = 111 g mol^{-1}). The intensity ratios between the fragments 83, 96 and 111 are constant during the potential scan, indicating that the aromatic radical, which is formed at the cathode in a first step, is stable and volatile, and in contrast to the BMP radical it does not decompose before ionization in the MS.

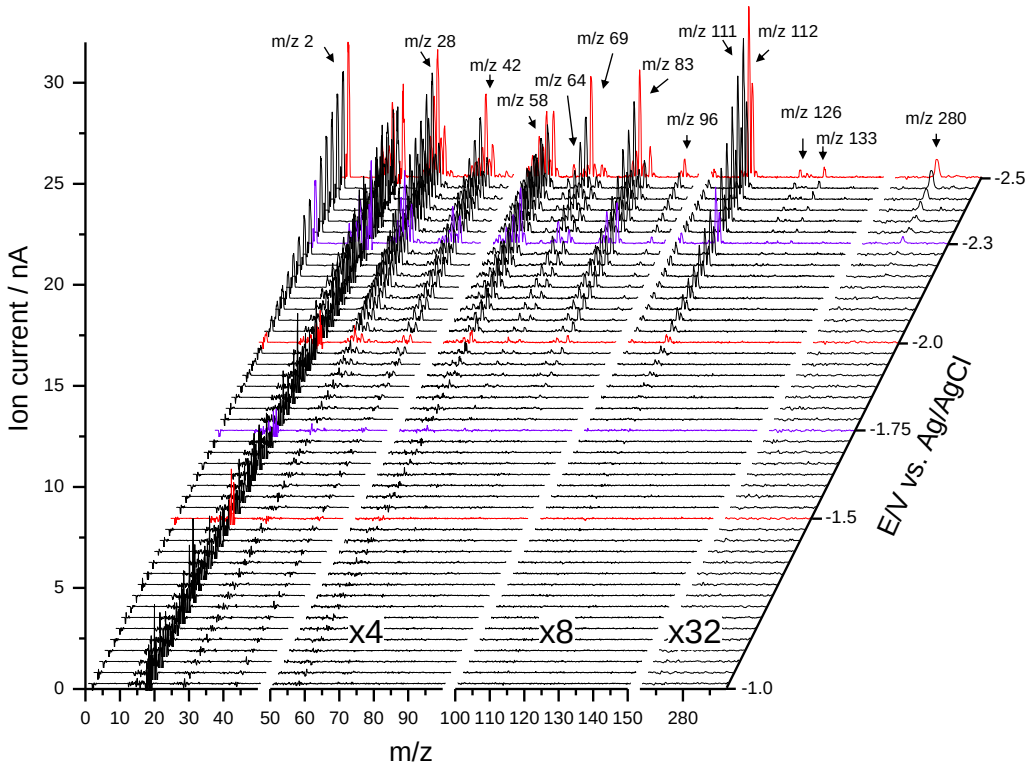


Figure 15: Sequence of mass spectra following the cathodic decomposition of EMIM-TFSI during the first cathodic potential scan, plotted against the potential (scan rate 10 mVs^{-1}). The spectra cover the range 0 < m/z < 300, regions with no signals appearing are cut. The spectra marked red indicate potential steps of 0.5 V, the purple lines indicate potentials explicitly mentioned in the text.

A rather similar aromatic radical, which has a butyl side chain instead of the ethyl side chain with tetrafluoroborate as anion (BMIM-BF_4), was suggested to be stable by Kroon et al.[46] based on the results of quantum chemical calculations. According to their calculations two radicals either form a dimer or, by exchanging an H-atom, disproportionate into a carbene (M = 110 $gmol^{-1}$) and a compound with a saturated C2 carbon (M = 112 $gmol^{-1}$). ^{1}H NMR analysis after electrolysis of BMIM-BF_4 showed that the H-atom attached to the C2 carbon atom is no longer connected to an aromatic C-atom in the decomposition product, in agreement with the radical structure (M = 111 $gmol^{-1}$). ^{13}C NMR results supported the disproportionation since changes in the NMR spectra after BMIM-BF_4 decomposition point to the presence of a C or CH_2 carbon atom but dimer formation could not be excluded.[46]

Xiao et al. also studied the electrochemical decomposition of BMIM-BF_4 and analyzed the products with NMR spectroscopy.[132] In agreement with the results of Kroon et al. they also concluded that the C2 carbon atom is no longer part of an aromatic system. However, they proposed another route for the formation of the carbene via elimination of hydrogen from the radical.[132] Lane[127] proposed in his review paper in general that the 1,3-dialkylimidazoliums, which have alkyl sidechains, would be reduced to the radical which can further react via dimerization or disproportionation reactions.

The ions detected at m/z 110 and 112 in our measurements could be attributed to the disproportionation products proposed by Kroon et al. as discussed above supporting their suggested mechanism. The low relative intensity of the m/z 110 signal, which is only one tenth of the m/z 112 signal intensity instead of the expected 1:1 ratio, seems to contradict this interpretation, but these differences could also be due to differences in the volatility of the two species.

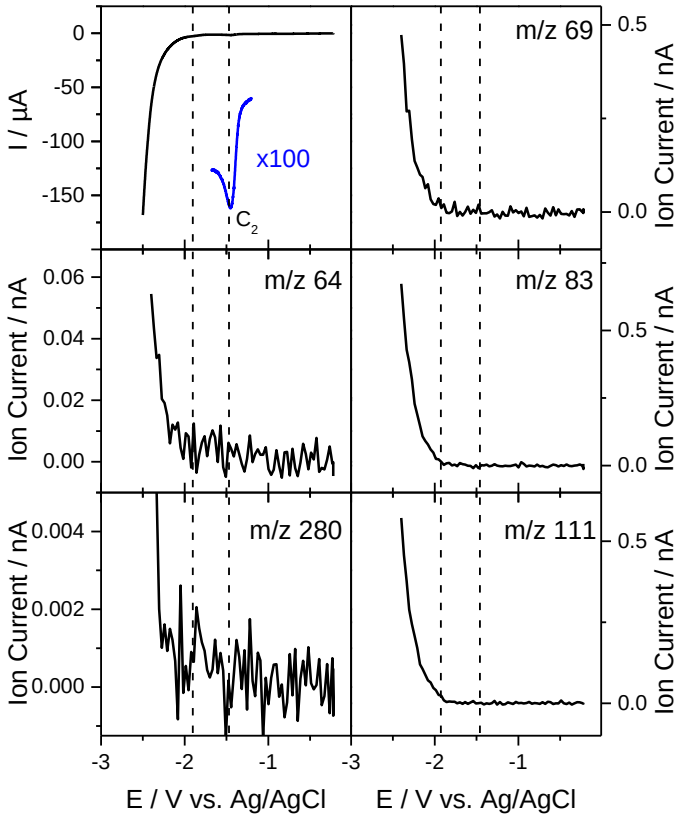


Figure 16: Faradaic current (top left) and ion currents (m/z = 64, 69, 83, 111 and 280, see figure) recorded during the first cathodic potential scan in EMIM-TFSI (scan rate 10 mVs^{-1}).

Formation of the carbene via H_2 elimination, as proposed by Li et al.,[132] could be an explanation for the H_2 signal in our mass spectra. However, this should further enhance the m/z 110 signal in comparison to the m/z 112 signal.

Masses which can support the formation of a dimer, as it had been proposed by Kroon et al.,[46] could not be detected in our measurements. It is possible, however, that the dimers are not volatile enough or decompose during ionization in the MS.

The magnification of the Faradaic current signal (×100) in Figure 15 shows a similar peak at about -1.5 V (C2) for EMIM-TFSI as discussed above for BMP-TFSI. In contrast to BMP-TFSI we did not detect any signals of volatile reaction products by mass spectrometry at this potential. This further support that in the case of BMP-TFSI these peaks in the Faradaic current appeared only incidentally together with the onset of the detection of the first BMP decomposition products (see our discussion in section 3.1.3.1).

The masses 64, 69, 133 and 280 in Figure 14 can again be attributed to the $TFSI^-$ anion and its decomposition products, respectively. These signals start increasing at a potential more

negative than -2.3 V, except of m/z 69, which was assigned to the CF_3 group and which starts growing already at -1.75 V, together with essentially all fragments of the cation. (We relate apparent discrepancies in the onset potentials to the different intensities of different fragments.) This leads to the assumption that a fragment of the cation has the same mass-to-charge ratio in the MS, e.g. $C_3H_5N_2$.[144] In that case the decomposition behaviour of EMIM-TFSI at cathodic potentials is similar to the behaviour of BMP-TFSI in the sense that the anion decomposition at $E \leq -2.3$ V is due to a chemical reaction of the $TFSI^-$ anion with decomposition products of the cation, which had been formed in the cathodic scan starting at -1.75 V. All masses which are explained above and the assigned fragments are also listed in Table 2.

Table 2: Assignment of the m/z values to possible fragments of EMIM-TFSI.

m/z	Ion	Origin
2	H_2^+	EMIM
28	$C_2H_4^+$, CH_2N^+, N_2	EMIM
42	$C_2H_4N^+$	EMIM
58	$C_2H_6N_2^+$	EMIM
69	$C_3H_5N_2^+$	EMIM
83	$C_4H_7N_2^+$	EMIM
96	$C_5H_8N_2^+$	EMIM
111	$C_6H_{11}N_2^+$	EMIM
112	$C_6H_{12}N_2^+$	EMIM
64	SO_2^+	TFSI
69	CF_3^+	TFSI
133	CF_3SO_2	TFSI
280	$(CF_3SO_2)_2N$	TFSI

In a second experiment, the decomposition was followed in a first anodic scan in EMIM-TFSI ramping the potential from -0.5 V to 2.7 V (mass scans see supporting information). The Faradaic current signal and the ion currents of the most prominent m/z 64, 69, 83, 111 and 280 signals derived from the mass spectra are shown in Figure 16.

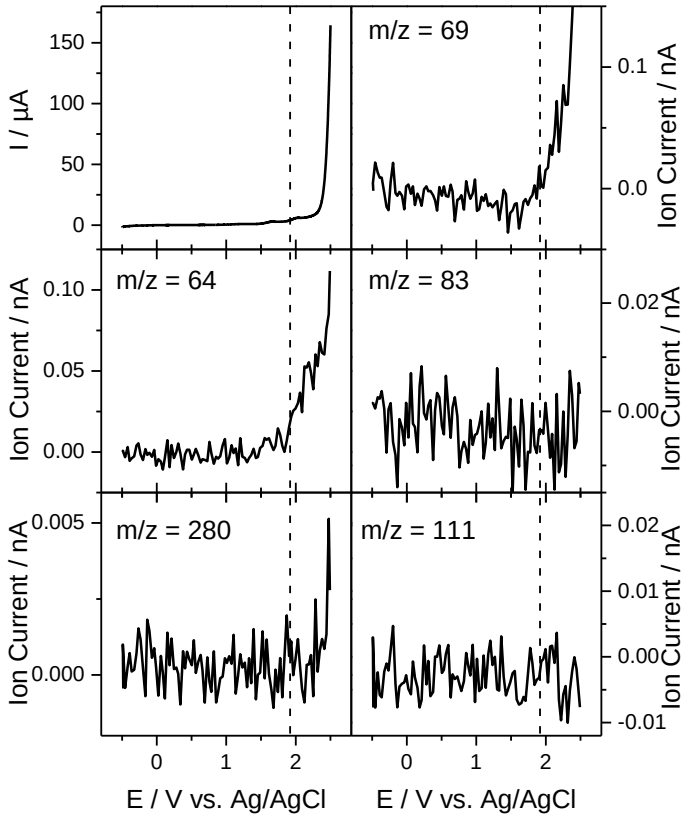


Figure 17: Faradaic current (top left) and ion currents (m/z = 64, 69, 83, 111 and 280, see figure) recorded during the first anodic potential scan in EMIM-TFSI (scan rate 10 mVs^{-1}).

In the Faradaic current signal we find no distinct peaks before the onset of the exponential increase, at around 1.5 V. The decomposition of the anion seems to follow the same trend as that in BMP-TFSI, although it seems to start at slightly lower potential. (As mentioned before the exact definition of the onset potential depends somewhat on the intensity of the signal.) The signals of the masses 64, 69 and 280, which can be correlated to the $TFSI^-$ anion, increase simultaneously with the onset of the Faradaic current. This means that the decomposition of the anion at anodic potentials starts first and it is independent of the cation in the IL. The intensity ratio of the signals at m/z 64 and 69 is constant, i.e., independent of the potential and similar to that observed for the anodic decomposition of BMP-TFSI.

In summary, the results of the electrochemical decomposition of EMIM-TFSI resemble those of BMP-TFSI at anodic potentials, where the anion is decomposed. At cathodic potentials the $EMIM^+$ cation is reduced resulting in the formation of a stable volatile radical and the related species with a saturated C2 atom as well as a carbene.

3.2.4 Conclusions

We developed a novel DEMS setup for investigating the electrochemical stability and decomposition of ionic liquids and ionic liquid based electrolytes in an open cell under vacuum conditions. Employing this setup, which allows the simultaneous online detection of volatile reaction products during electrochemical measurements, for studying the electrochemical decomposition behaviour of the ILs BMP-TFSI and EMIM-TFSI at a polycrystalline Au electrode, resulted in the following conclusions:

The DEMS set-up allows us to identify volatile reaction products with high sensitivity and, despite the viscosity of the electrolyte, reasonable time resolution. It can clearly separate between products formed at the counter electrode and at the working electrode.

At cathodic potentials the decomposition of both ILs starts via decomposition of the cations, at a potential of -1.0 V. for BMP^+ and at -1.75 V for the $EMIM^+$ cation. At potentials more negative than -2.6 V in BMP-TFSI and -2.3 V in EMIM-TFSI also the anion starts to decompose, probably mediated by reactive reaction intermediates of the cation decomposition.

At anodic potentials the $TFSI^-$ anion decomposes, starting at 2.2 V for BMP-TFSI at 1.8 V for EMIM-TFSI.

MS detection supports previous proposals / reports that cathodic BMP-TFSI decomposition starts by cleaving the bond between the ring and the butyl side chain, which results in the formation of methylpyrrolidine and a butyl moitey. At more negative potentials, a ring opening reaction leads to the detection of dibutylmethylamine. Anodic BMP-TFSI decomposition most probably proceeds via oxidation of $TFSI^-$ to a neutral volatile TFSI species.

The decomposition behaviour of EMIM-TFSI in the cathodic scan differs from that of BMP-TFSI, as $EMIM^+$ reduction results in a rather stable radical which is detected in the MS. Further reactions of the radical result in the formation of a carbene and a compound with a saturated C2 carbon. The anodic EMIM-TFSI decomposition starts with the oxidation of the $TFSI^-$ anion, similar as the anodic BMP-TFSI decomposition.

3.2.5 Supporting Information

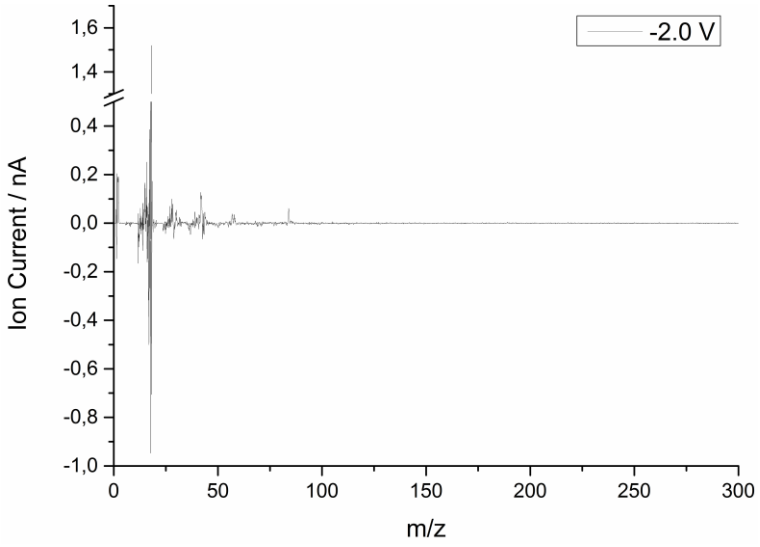


Figure 18: Mass spectrum of BMP-TFSI decomposition recorded during the first cathodic potential scan at – 2.0 V vs Ag/AgCl.

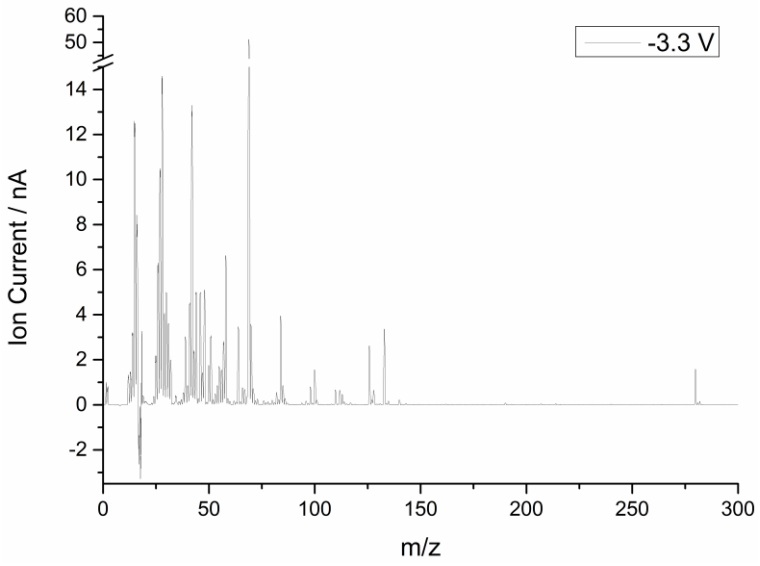


Figure 19: Mass spectrum of BMP-TFSI decomposition recorded during the first cathodic potential scan at – 3.3 V vs Ag/AgCl.

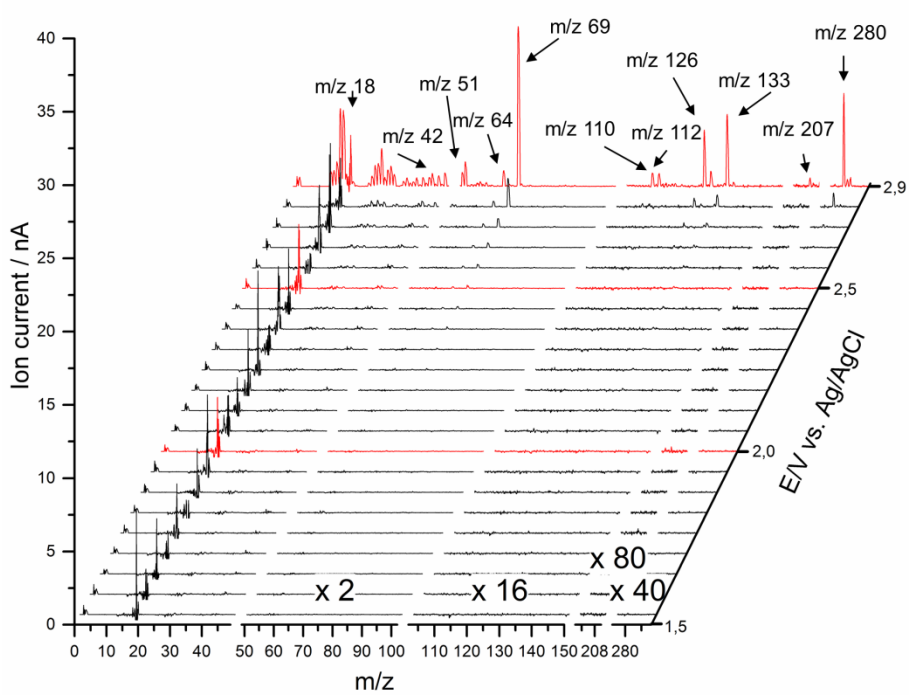


Figure 20: Sequence of mass spectra following the anodic decomposition of BMP-TFSI during the first anodic potential scan, plotted against the potential (scan rate 10 mVs^{-1}). The spectra cover the range 0 < m/z < 300, regions with no signals appearing are cut. The spectra marked red indicate potential steps of 0.5 V.

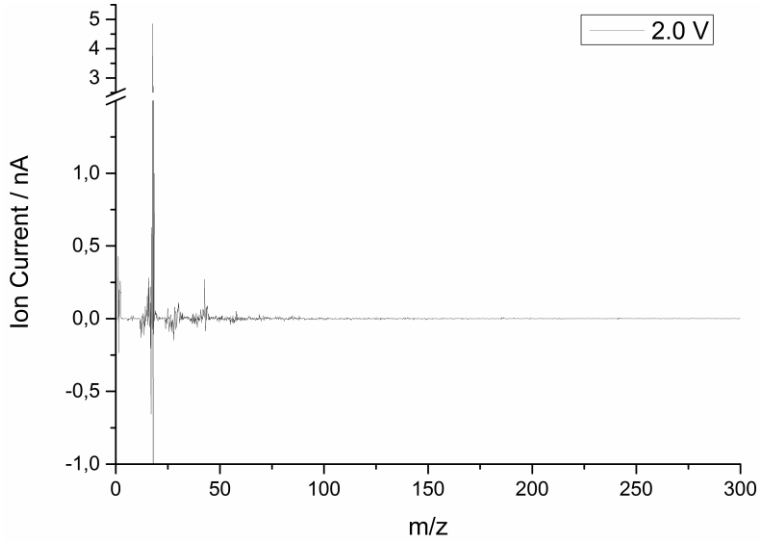


Figure 21: Mass spectrum of BMP-TFSI decomposition recorded during the first anodic potential scan at 2.0 V vs Ag/AgCl.

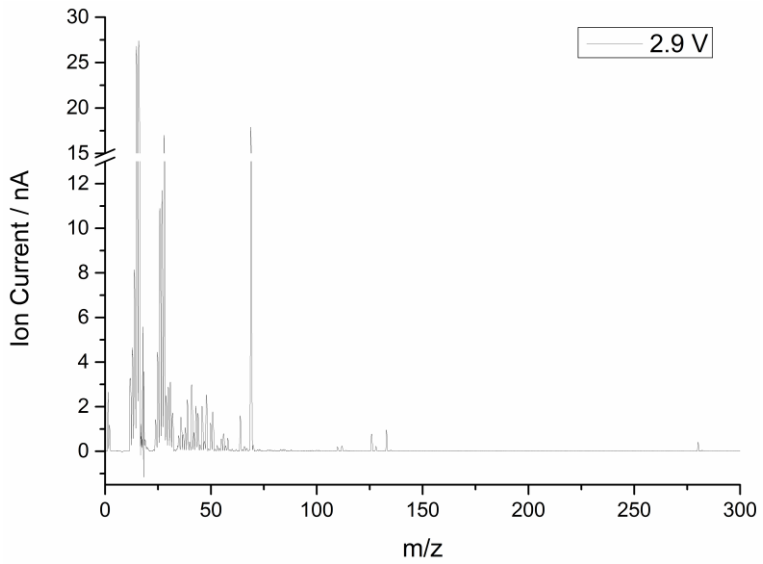


Figure 22: Mass spectrum of BMP-TFSI decomposition recorded during the first anodic potential scan at 2.9 V vs Ag/AgCl.

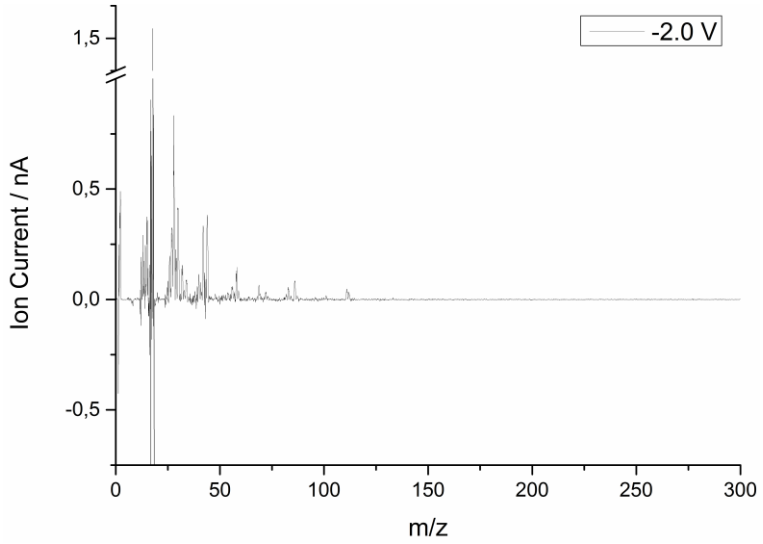


Figure 23: Mass spectrum of EMIM-TFSI decomposition recorded during the first cathodic potential scan at – 2.0 V vs Ag/AgCl.

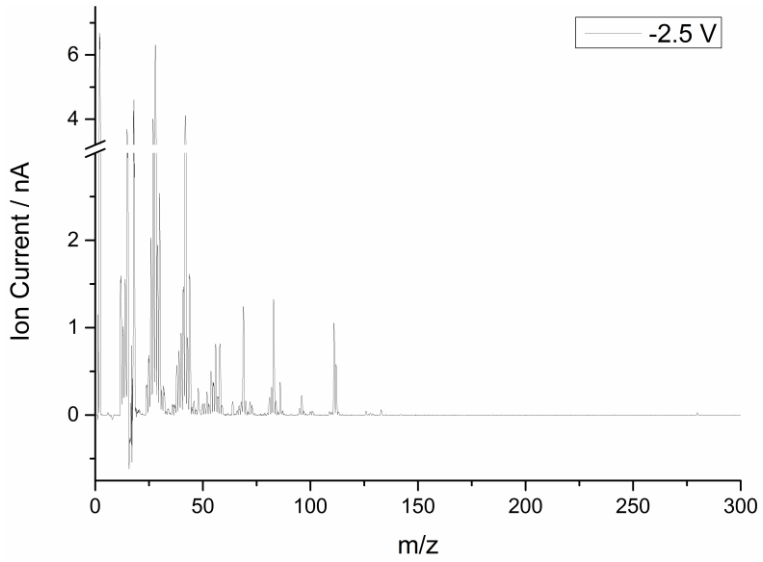


Figure 24: Mass spectrum of EMIM-TFSI decomposition recorded during the first cathodic potential scan at – 2.5 V vs Ag/AgCl.

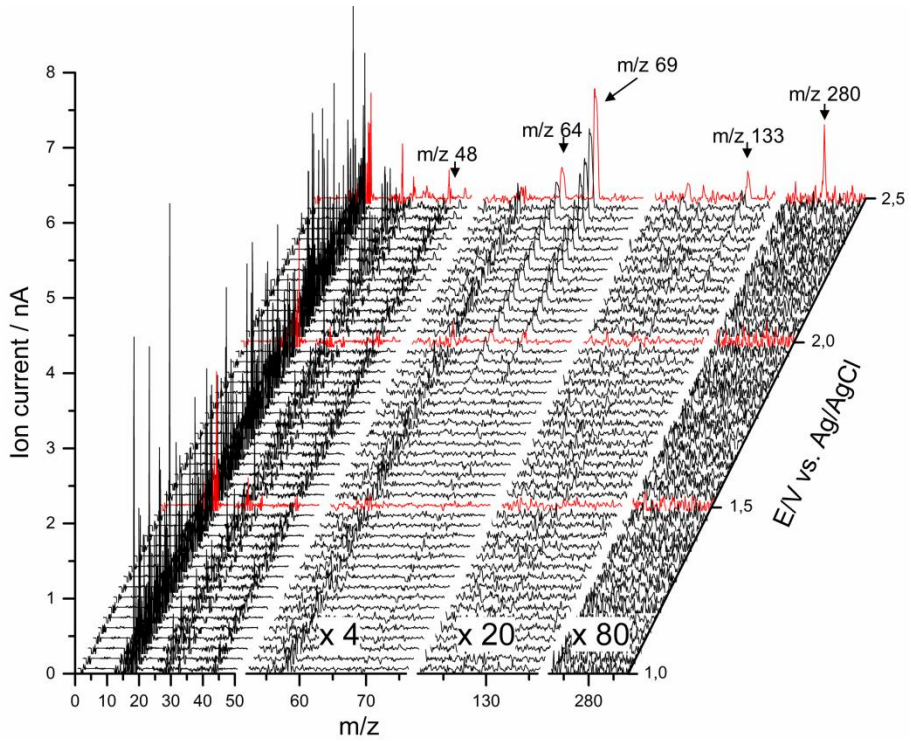


Figure 25: Sequence of mass spectra following the anodic decomposition of EMIM-TFSI during the first anodic potential scan, plotted against the potential (scan rate 10 mVs^{-1}). The spectra cover the range $0 < m/z < 300$, regions with no signals appearing are cut. The spectra marked red indicate potential steps of 0.5 V.

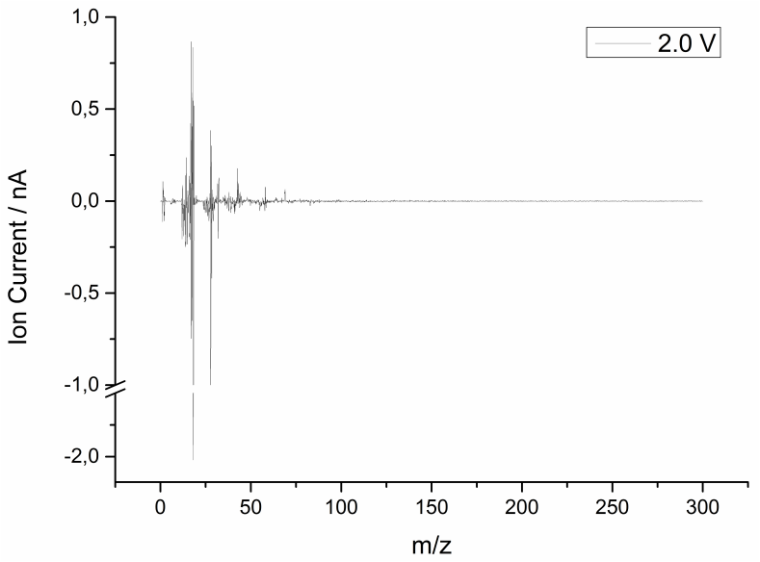


Figure 26: Mass spectrum of EMIM-TFSI decomposition recorded during the first anodic potential scan at 2.0 V vs Ag/AgCl.

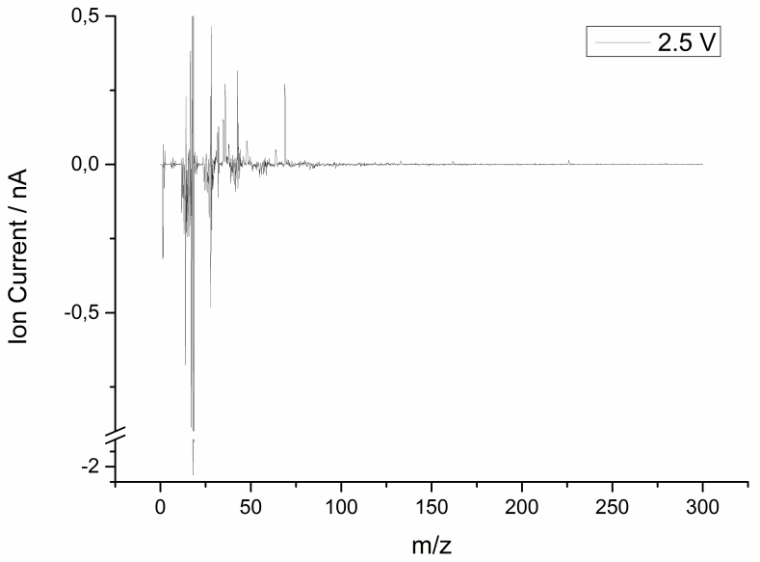


Figure 27: Mass spectrum of EMIM-TFSI decomposition recorded during the first anodic potential scan at 2.5 V vs Ag/AgCl.

3.3 Effect of Li^+ and Mg^{2+} on the Electrochemical Decomposition of the Ionic Liquid 1-Butyl-1-methylpyrrolidinium bis(trifluoromethanesulfonyl)imide and Related Electrolytes

The content of this chapter was published in reference [145] and is reprinted with permission by ChemElectroChem / John Wiley and Sons (ChemElectroChem 2019, 12, 3009 / 10.1002/celc.201900371). The experimental section was removed and the information was added to the experimental part in chapter 2 of this work. The style and numbering of the references and the figures have been adapted to fit the layout of the thesis. All experiments in this work were planned by me. The electrochemical measurements on the GC electrode were conducted by Kurtus Hancock and on Au with added Li^+ and Mg^{2+} ions by Gülsah Yetis in her Bachelor thesis, both under my supervision. I performed the full data evaluation and prepared all figures. Furthermore, I was strongly involved in the creative process of the publication. This work was financially supported by the German Federal Ministry of Education and Research (BMBF) in the projects 03X4636C ("Li-EcoSafe – Entwicklung kostengünstiger und sicherer Lithium-Ionen-Batterien") and 03EK3027B ("Perspektiven für wiederaufladbare Mg-Luftbatterien"). This work contributes to the research performed at CELEST (Center for Electrochemical Energy Storage Ulm-Karlsruhe).

3.3.1 Abstract

We investigated the decomposition of 1-butyl-1-methylpyrrolidinium bis(trifluoromethane-sulfonyl)imide (BMP-TFSI) based electrolytes on Au and glassy carbon (GC) in the absence and presence of Li(TFSI) and $Mg(TFSI)_2$. Detecting the volatile reaction products via differential electrochemical mass spectrometry (DEMS) measurements allowed us to gain insight into the decomposition mechanisms. In neat ionic liquid (IL) and on Au electrodes both ions are decomposed at reductive potentials. The $TFSI^-$ anion mainly decomposes by releasing CF_3, while for the BMP^+ cation ring opening and scission of either the methyl or the butyl side chain occur in parallel. At oxidative potentials the decomposition of the anion is the predominant process. Changing to the GC electrode increases the fraction of $TFSI^-$ decomposition products at both cathodic and anodic potentials. The addition of Li^+ largely hinders the formation of volatile BMP-TFSI decomposition. In contrast, addition of Mg^{2+} promotes the $TFSI^-$ decomposition at the expense of the BMP^+ decomposition.

3.3.2 Introduction

Ionic liquids (ILs) have attracted considerable interest in recent years for potential application as electrolyte in novel battery systems[32,111,146-150] or as additive in electrolyte mixtures[151] because of a number of interesting properties such as very low vapour pressure, low flammability and high thermal and electrochemical stability, and inherent ionic conductivity. For these applications the electrochemical stability is a key aspect, since the high cell voltages of such systems are likely to exceed the stability range of traditional organic electrolytes. Hence, the development of stable electrolytes or the formation of suitable, ion conducting passivation layers (solid electrolyte interphase, SEI),[35,39,129,152] is imperative for the successful introduction of new battery technologies.[153]

Starting point for a systematic approach to these problems is a detailed understanding of the decomposition behaviour of ILs as solvents or electrolytes. Recently, we developed a novel, membrane free set-up for differential electrochemical mass spectrometry (DEMS) for identifying the volatile decomposition products of ionic liquids. This was employed for characterizing the volatile products formed during anodic and cathodic decomposition of 1-butyl-1-methylpyrrolidinium bis(trifluoromethanesulfonyl)imide (BMP-TFSI) on Au.[110] In the present paper we expand on this preliminary study, investigating the influence of the electrode material by monitoring the formation of volatile reaction products in linear sweep half-cell measurements. In addition to our Au model system, we chose glassy carbon as model system for carbon based electrode materials, which are found in many battery electrodes, either as intercalation material or as additive to enhance the conductivity. Furthermore, we studied the influence of typical metal cations on the decomposition behaviour, which act as charge carrier in battery electrolytes. Aiming at lithium-ion batteries (LIBs) and considering that Mg^{2+} is discussed as interesting charge carrier for next generation batteries because of its natural abundance,[154,155] we selected Li^+ and Mg^{2+}. Finally, triggered by unclear results of our initial study, we also explored possible effects of trace impurities by comparing the ILs from two different suppliers.

Before presenting and discussing our results, we will briefly summarize results of previous studies relevant for this work. Employing Raman spectroscopy, Giffin et al. concluded on a strong coordination of TFSI with Li^+ and Mg^{2+} in BMP-TFSI.[156] Also using Raman and NMR spectroscopy, Jeremias et al. showed for Mg^{2+} that TFSI anions are coordinated in bidentate and bridging configurations, with an increasing fraction of bidentate species at higher Mg^{2+} concentrations.[157] Sodeyama et al. studied the influence of Li^+ on the decomposition of Li(TFSI) in acetonitrile solutions theoretically, employing density functional theory based

molecular dynamics simulations. They calculated that for highly concentrated electrolytes TFSI anions accept the reductive electron, leading to TFSI decomposition.[158] Rajput et al. investigated $Mg(TFSI)_2$ containing electrolytes by using quantum chemistry and molecular dynamics simulations and reported that ion pairs are formed. If an electron is added to the ion pair, the Mg cation centre is reduced; however, the ion pair stabilizes by splitting the C-S bond of the TFSI anion.[159] Experimental confirmation of these results is, however, still largely missing, and it would be interesting to know whether these metal cations have an effect on the product distribution and / or the decomposition pathway of anion and / or cation.

In the following we will first present the results of potential sweeps of a Au model electrode in neat BMP-TFSI IL, comparing the characteristics of ILs from two suppliers, where we aim at identifying possible effects from trace impurities (section 3.2.3.1). Next we focus on possible effects of the electrode material, comparing the decomposition behaviour at Au and glassy carbon electrodes (section 3.2.3.2). Finally we examine the effect of both Li(TFSI) and $Mg(TFSI)_2$ in 0.1 and 1 M concentration on the decomposition of BMP-TFSI at Au electrodes (section 3.2.3.3). The results are summarized in section 3.2.4.

3.3.3 Results and discussion

3.3.3.1 Influence of impurities

We start with showing the Faradaic current measured at the Au electrode and the ion currents of m/z = 57, 64, 69, 84, 100, 133 and 280 during a linear potential sweep from 0.5 to -3.2 V in Figure 28. These specific mass-to-charge ratios were chosen from mass spectra measured between m/z = 0 and 300 because of their distinct signals during the decomposition. They are attributed to anion or cation decomposition/fragmentation products:[110] The fragments related to cation decomposition (m/z = 57, 84, 100) are displayed in the left side of the panel and the fragments related to anion decomposition (m/z = 64, 69, 133, 280) in the right side. A detailed discussion of the assignment of the fragments is given later in this chapter. The red (Solvionic) and black (Merck) curves are measurements of BMP-TFSI from two different suppliers, which were measured via exactly the same procedure. The data for the Merck IL were already presented previously,[110] but are included here for comparison. In the beginning only capacitive currents (upper left panel) are detected for both electrolytes, before a cathodic current appears at -1.2 V (Merck) or -1.4 V (Solvionic) (see magnified current trace in the inset), which results in a small peak at -1.52 V (Merck) or at -1.56 V (Solvionic). Peaks in this

potential region have previously been attributed to a rearrangement of adsorbates on the surface[33,123,133,134,160] or to decomposition of the $TFSI^-$ anion.[139]

The small difference of 0.04 V between the peak positions for the two ILs, may be due to (different) impurities in the two ILs. Another possible reason is the variation in the potential of the quasi-reference electrode, which turned out to be around ± 0.1 V in repeated measurements with Fc/Fc^+.[110] At more cathodic potentials, in the Merck electrolyte the exponential increase of the cathodic current starts at -2.4 V, which is about 0.2 V more positive in comparison to the red (Solvionic) curve. This difference in the onset of decomposition, which for the Merck IL is at 0.2 V more positive potential than for the Solvionic IL, cannot be explained by the instability of the potential of the quasi-reference electrode alone. Overall we find in both cases a small peak in the cathodic current at rather similar potentials for the two ILs, at -1.52 V (Merck) and -1.56 V (Solvionic), and an exponential increase, where the differences in the onset potential are more pronounced (-2.4 V (Merck) vs. -2.6 V (Solvionic)). After reversal of the scan direction at the lower potential limit (not shown), the current trace largely follows the trace of the preceding cathodic scan (see also [110]).

Further information on the physical origin of these discrepancies and the nature of the processes contributing to the decomposition current can be obtained from the mass signals presented in Figure 28. We will start with the BMP^+ cation decomposition during the cathodic scan. An overview about the possible reductive decomposition pathways of BMP^+, which is based on the results of density functional theory type calculations and molecular dynamics simulations by Haskins et al. and Kroon et al., is given in Figure 29.[39,46] In addition, we also list the m/z values of the main fragments of the decomposition products, which are expected after ionization of the calculated decomposition products in the MS according to the NIST database.[106] According to Kroon et al., the first step of the BMP^+ ion reduction at the electrode is the formation of an unstable $BMP^\bullet$ radical.[46] The $BMP^\bullet$ radical can either decompose into i) butylpyrrolidine, with the main fragment m/z = 84, and a methyl radical (R1), into ii) methylpyrrolidine (fragments m/z = 84, 57, 42 in about similar ratio) and a butyl radical (R2) or iii) via a ring opening reaction into a dibutylmethylamine radical, with the main fragment at m/z = 100 (R3).

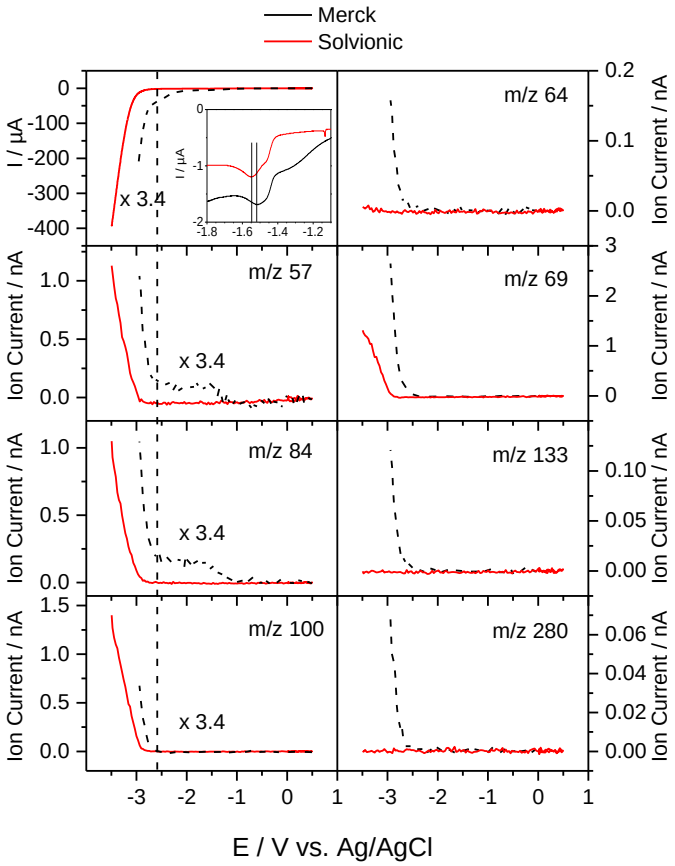


Figure 28: Faradaic current (top left) and ion currents attributed to cation (left: m/z 57, 84, 100) and anion (right: m/z = 64, 69, 133, 280) decomposition recorded during the first cathodic potential scan in BMP-TFSI (scan rate 10 mV s^{-1}) on a Au electrode. Inset: magnification of Faradaic current.

For the BMP-TFSI from Merck, the ion currents at m/z = 57 and 84 start to increase at about -1.5 V and then form a plateau, which reaches down to -2.6 V (indicated by the dashed line in Figure 28). Subsequently these signals increase steeply, with an onset at about -2.6 V. At the same potential, also the m/z = 100 signal rises steeply, which was at the background level so far. In contrast, the ion currents recorded in the Solvionic IL do not start to grow before -2.9 V. In both cases this goes along with a drastic increase in the Faradaic current, as expected for the onset of the reductive decomposition of BMP^+. Based on the comparison, the ion currents measured between -1.0 and -2.6 V seem to be due to the reduction of impurities in the Merck IL rather than to an inherent slow decomposition of the IL in this potential range. This conclusion differs from our previous assignment, where we had tentatively favored an initial reduction of the BMP cation via the scission of the bond between the pyrrolidinium ring and the butyl chain along reaction path R2, since we had made the same observations in two different batches of BMP-TFSI.[110]

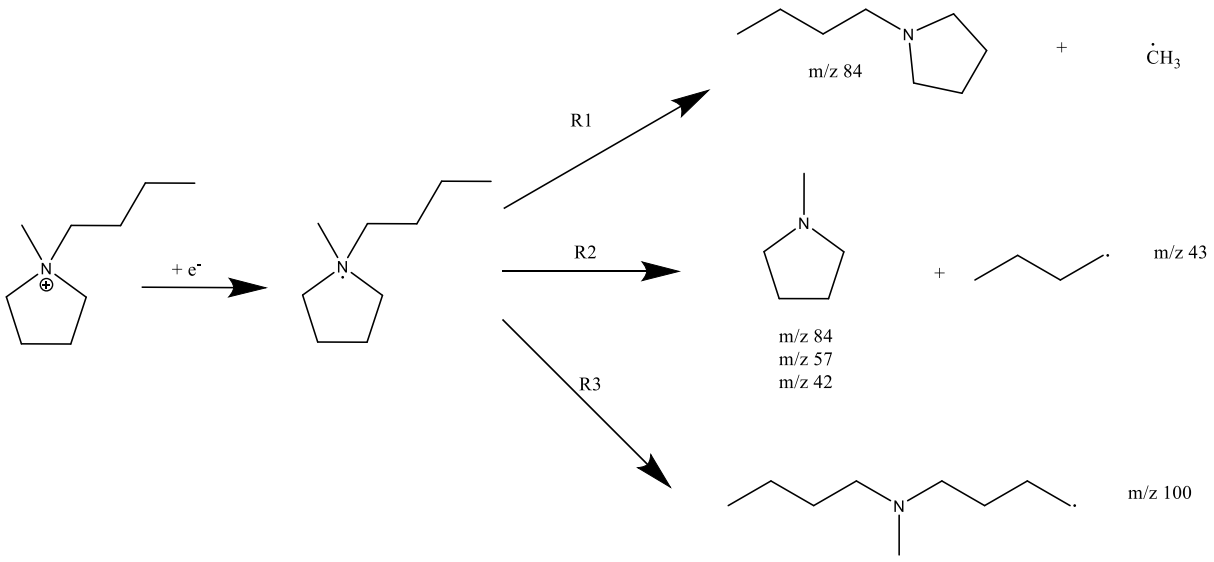


Figure 29: Possible decomposition mechanisms of BMP^+ and the expected m/z ratios.[39,46]

Compared to the potential difference of the small peak at about -1.5 V discussed above, which was of the order of 0.04 V, this difference of 0.2 V seems to be significant. This indicates that the impurities could also catalyze the decomposition. In addition to the differences in the potential range -1.0 – -2.6 V, there are also differences in the distribution of the cation decomposition products between the two ILs: In the Merck IL, the ion currents of m/z = 57 and 84 are rather similar in magnitude, while the m/z = 100 is only about half of those. For the Solvionic IL, in contrast, all three fragments have about similar intensities and their intensity ratios are constant when scanning to more negative potentials (see section 3.3.3.2 and Figure 32 for a more detailed discussion). Hence, in the Merck IL the ring opening pathway (R3) is less probable than in the Solvionic IL. Based on *ab initio* molecular dynamics simulations and density functional calculations of BMP-TFSI decomposition on a negatively charged Li electrode, Haskins et al. found rather similar reductive bond dissociation energies for the different decomposition pathways (between 94.1 and 98.3 kcal/mol) resulting in methylpyrrolidine, butylpyrrolidine and dibutylmethylamine.[39] Thus, not considering kinetic effects, the simultaneous formation of the three products in Solvionic IL is not in contrast to the computational results.

The ion current signals related to cathodic anion decomposition are collected in the right panels in Figure 28. Though it seems to be counterintuitive, reductive decomposition of the $TFSI^-$ anion had been indicated by *ab initio* molecular dynamics simulations[38] and by experimental findings.[125,136,161] Similar as for cation decomposition, we start by giving an overview of possible reductive decomposition pathways for the $TFSI^-$ anion based on the calculations by Haskins et al.,[39] and of the resulting m/z ratios, which were actually detected in the mass spectrometer, in Figure 30.

In the first step in reaction pathway R4, the $TFSI^-$ anion is reduced to the metastable dianion, which can then decompose in three different ways, i.e., via splitting a C-F, a C-S or a N-S bond. Among those, splitting the C-F bond has been calculated to exhibit the highest Free Energy for bond dissociation (BDFE), but subsequently the residual molecule is stabilized by a structural rearrangement, leading to an in total negative value of the BDFE in this pathway (R5).[39] Nevertheless, this pathway is likely to exhibit a considerable kinetic barrier. The rearrangement also weakens the bond between the N and the S atom of the SO_2 group,[39] which might lead to the separation of the SO_2 group and therefore explain the observation of SO_2 (m/z = 64) species in our mass spectra. Splitting the C-S bond (R6) is calculated to have a slightly positive BDFE.[39] On the other hand, there has been some experimental evidence for this pathway by Markevich et al.,[125] who detected CF_3 moieties upon reductive decomposition of BMP-TFSI in the gas phase above the electrochemical cell by *in situ* FTIR spectroscopy. The lowest BDFE was calculated for the third pathway (R7), the breaking of the N-S bond of the molecule.[39]

For the Merck IL, the ion currents of m/z = 64 (SO_2^+), 69 (CF_3^+), 133 ($SO_2CF_3^+$) and m/z = 280 ($TFSI^+$), which are related to the TFSI anion, show an exponential increase, starting at a potential of -2.6 V. For the latter signal we previously speculated that this fragment originates from a chemical reaction between reactive BMP^+ reduction intermediates (radicals) and the $TFSI^-$ anion, forming volatile, neutral $TFSI^\bullet$ radicals.[110] In the Solvionic IL, in contrast, we do not find any increase in the m/z = 64, 133 and 280 signals in the potential range covered. Only the ion current at m/z = 69 shows a significant increase, which starts at -2.9 V. This implies that the reaction pathway R6 is favored in this system, in agreement with observations by Markewich et al.[125] In summary, in Solvionic IL the cation decomposition starts in parallel with the electrochemical decomposition of the anion at -2.9 V. The former proceeds via simultaneous formation of methylpyrrolidine, butylpyrrolidine and dibutylmethylamine, while anion decomposition starts with the scission of the bond between the C atom of the CF_3 group and the neighboring S atom.

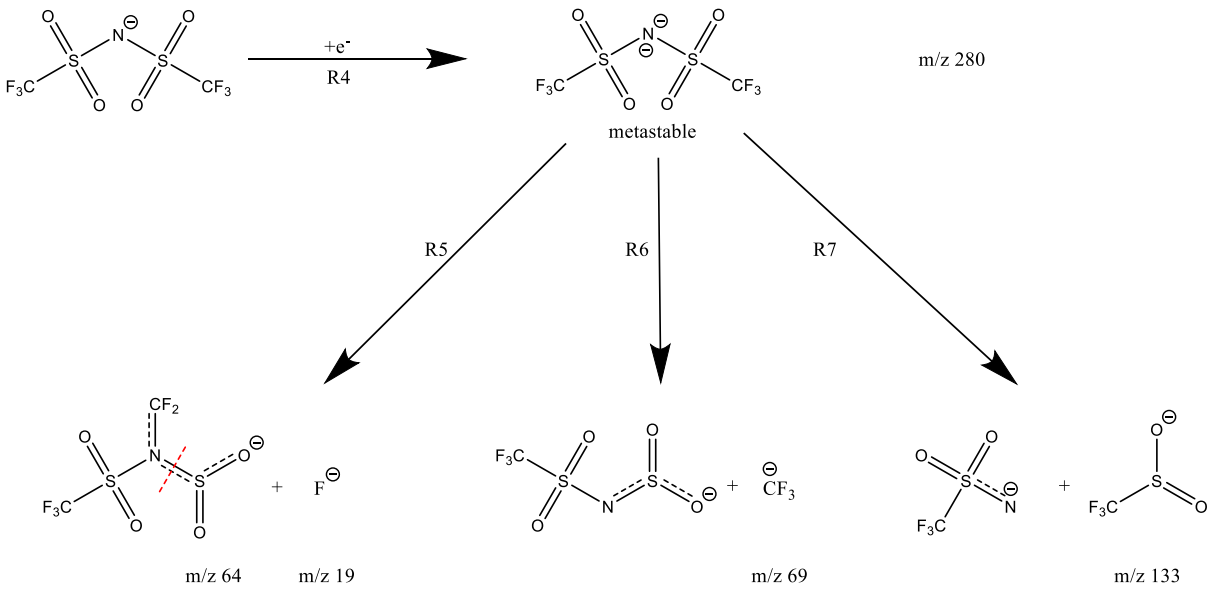


Figure 30: Decomposition pathways for $TFSI^-$ decomposition at reductive conditions as proposed by Haskins et al.,[39] and the expected m/z ratios.

Although the simultaneous decomposition of BMP^+ and $TFSI^-$ may just be a coincidence, we tentatively assume that the radicals formed in the BMP^+ reduction trigger the decomposition of $TFSI^-$. For the Merck IL all fragments are observed, including the molecular ion at m/z = 280 and hence all reaction pathways seem to contribute to the anion decomposition. Based on the

presence of the molecular ion, the signals at m/z = 64, 69 and 133 might (at least in part) also be a result of the fragmentation of the molecule ion, via electron impact ionization in the MS. Most likely, the trace impurities present in this IL or the cation decomposition products formed in the potential range of -1.0 – -2.6 are responsible for the difference in anion decomposition. Additionally, the ratio of the ion currents 69 to 84 is about five times higher in Merck IL. Apparently, not only the product distribution resulting from anion or cation decomposition, but also the relative amounts of anion and cation reduction are affected by the trace impurities.

In the anodic scan we did not observe any significant differences in the decomposition behaviour of the ILs of both suppliers. Therefore, we concluded that the TFSI anion is decomposed first and results mainly in the formation of CF_3, before also some fragments related to BMP^+ degradation occurs (see also [110]). The respective trace for the anodic decomposition of Solvionic IL is displayed below in Figure 33. For the further investigations only Solvionic IL was used.

3.3.3.2 Effect of the electrode material

In order to investigate the influence of the electrode material, we compared the decomposition of BMP-TFSI at a Au wire (as in the previous figures) and at a glassy carbon rod electrode at cathodic potentials. The resulting Faradaic current and ion current signals are plotted in Figure 31. Note that the Faradaic currents obtained on both electrodes in this measurement setup may vary somewhat due to differences in the wetted surface area (equivalent to the height of the wetted electrodes), which limits quantitative comparisons. The Faradaic currents depicted in the upper left panel are very similar for both working electrode materials, except for the peak at -1.5 V, which is not clearly resolved on the GC electrode (see inset). This is in line with the interpretation of this peak as being due to a rearrangement of the adsorbed ion species at a Au(111) surface.[133] However, for the GC electrode it may also just be hidden in a continuous increase of the Faradaic current (onset at about -0.7 V). The difference in the onset potential of the exponential increase between Au (-2.6 V) and GC (-2.7 V) electrodes is only 0.1 V, which is within the uncertainty of the quasi-reference electrode potential.

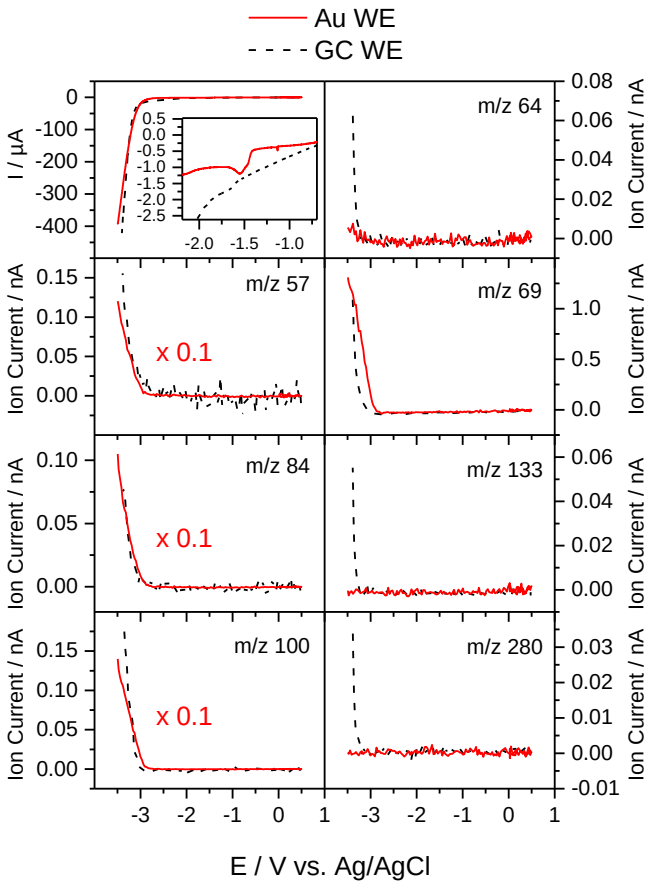


Figure 31: Faradaic current (top left) and ion currents attributed to the cation (left: m/z 57, 84, 100) and the anion (right: m/z = 64, 69, 133, 280) decomposition recorded during the first cathodic potential scan in BMP-TFSI (scan rate 10 mV s^{-1}) on Au and GC electrodes.

Continuing with the ion currents resulting from BMP^+ decomposition, we find them to increase in parallel with the Faradaic current, indicating that the BMP^+ cation is also decomposed at cathodic potentials, but with higher ion currents on the Au electrode.

More information on the preferred decomposition pathway and its possible variation with the applied potential can be gained by comparing the potential dependence of the different ion currents. From the similar behaviour of the signals of the BMP^+ fragments m/z = 57, 84 and 100 in Figure 31, with a constant intensity ratio throughout the cathodic potential scan, we conclude that the relative contributions of the different pathways for BMP^+ decomposition are independent of the applied potential. This can be rationalized if we assume that the first step is the electron transfer to the BMP^+ cation forming a radical, which then disintegrates in different fragments. This resembles recent interpretations by Goodwin et al., who concluded from the similar onset and shape of the respective ion currents that the oxidative decomposition of trifluoromethanesulfonate ions does not proceed via different pathways occurring at different potentials, but only via a single process, which can result in different products and whose rate increases with potential.[40]

Returning to BMP^+, the potential independent ratios of the m/z = 57 / m/z = 84 and 100 / 84 signals, which represent the reaction pathways R2 and R3 and the main fragment of pathway R1 (m/z = 84), are plotted in Figure 32 for all systems investigated (the Mg^{2+} containing electrolytes will be discussed in the following chapter). The different points with different colors show repeated measurements performed in the same way. This also gives an impression in how far variations of the decomposition behaviour are characteristic for the different electrode materials or reflect the scatter in the data.

As discussed above, we assume that i) the m/z = 84 signal evolves after the electrochemical elimination of one of the alkyl-chains (R1 and R2) and that ii) the m/z = 57 fragment is mainly a product of further methylpyrrolidine fragmentation in the ion source of the mass spectrometer, and to a minor extent of the fragmentation of N,N-dibutyl-N-methylamine after a ring opening reaction. On the Au electrode the splitting of the alkyl side chains and the ring opening occur in parallel, showing similar intensities of their characteristic main fragments, as discussed in the previous section. Considering the variations in these measurements, there is no significant difference in the relative intensity of the m/z = 100 signal, which is related to the ring opening pathway R3, for the Au and GC electrode. Thus, we conclude that neither of the two electrode materials especially promotes this pathway. In contrast, for the signal of m/z = 57 (indicative of pathway R2) we find a higher relative intensity (normalized to the m/z = 84 signal) on the GC electrode, indicating that this electrode promotes the scission of

the bond between the N atom and the butyl side chain. Hence, the electrode material has little impact on the electron transfer to the BMP^+ cation, which results in the instable $BMP^\bullet$ radical, while the second step, the decomposition of the radical, is indeed affected by the nature of the electrode.

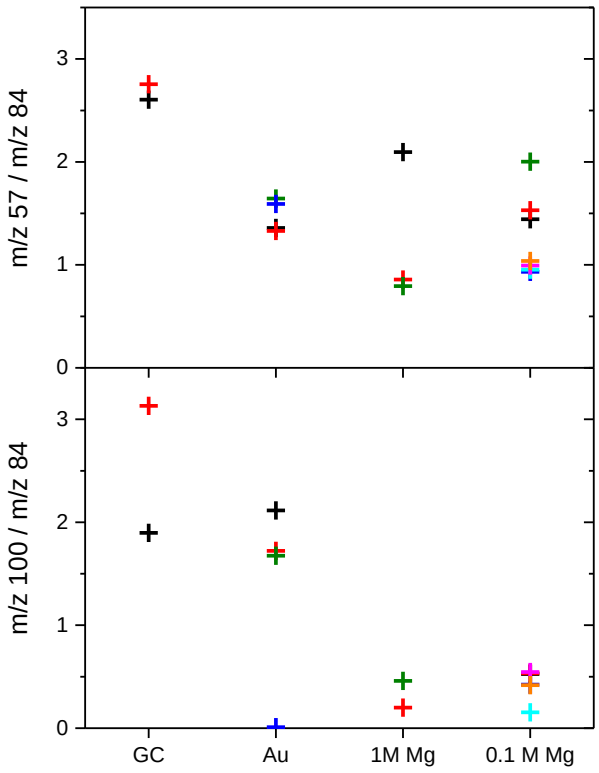


Figure 32: Ratios of the m/z = 57 and m/z = 100 signal intensities to that of the m/z = 84 signal on the Au and GC electrodes in pure BMP-TFSI as well as in 1 M and 0.1 M Mg(TFSI)2 containing BMP-TFSI on a Au electrode, measured at -3.0 to -3.4 V. The points show repeated measurements under allegedly identical conditions, similar colours in the upper and lower panel indicate that the points are related to the same measurement.

Going to the $TFSI^-$ decomposition at cathodic potentials, the only significant signal observed on the Au electrode was that at m/z = 69, starting at a potential of -2.9 V, which was assigned to the splitting of the C-S bond via pathway R6 (see section 3.3.3.1). Also on the GC electrode, the signal at m/z = 69 shows by far the highest intensity. Hence, also for this electrode the splitting of the C-S bond is the dominant pathway for the reductive decomposition of $TFSI^-$. In addition, however, also the other fragments attributed to anion decomposition start to evolve in parallel at -3.2 V. Since of all these m/z signals appear simultaneously, including the molecular ion, we assume that similar to the proposal for the Merck IL on a Au electrode the $TFSI^-$ anion reacts with a BMP^+ reduction product, leading to volatile, neutral $TFSI^\bullet$ radicals, which are partly fragmented by the ion source of the MS. Thus, there is another viable cathodic $TFSI^-$ decomposition pathway on the GC electrode, which does not occur on Au, at least not for the Solvionic IL.

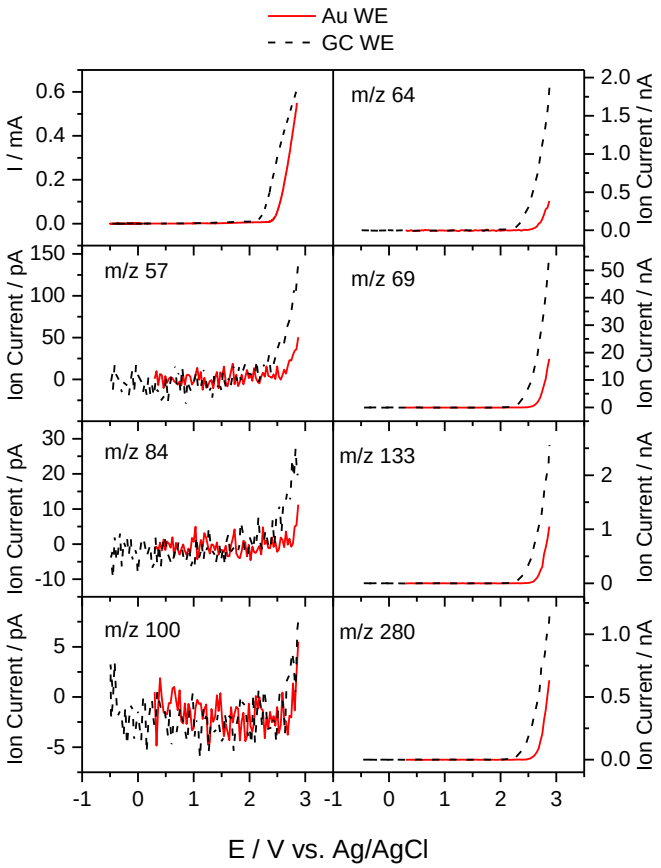


Figure 33: Faradaic current (top left) and ion currents attributed to cation (left: m/z 57, 84, 100) and the anion (right: m/z = 64, 69, 133, 280) decomposition recorded during the first anodic potential scan in BMP-TFSI (scan rate 10 mV s-1) on Au and GC electrodes.

Similar linear scan measurements were performed in the anodic potential range, showing both the Faradaic and the ion currents related to the different decomposition products and fragments discussed before, are presented in Figure 33. For the Faradaic current, the onset for the anodic decomposition is at around 2.1 V for the GC electrode, while it is at around 2.4 V for the Au electrode, where the difference is beyond the uncertainty in the reference electrode potential. Considering, however, the variation of ± 0.1 V in onset potentials between repeated measurements, this difference and hence the influence of the electrode material on the anodic onset of the decomposition is not significant. This might be due to small deviations in the water content between the measurements, because water impurities are known to reduce the stability of the electrolyte and thus narrow the accessible potential window.[35,40,162,163]

For all measurements, both on the GC and on the Au electrode, the $TFSI^-$ anion related currents (m/z = 64, 69, 133, 280) start to increase in parallel to the increase in the Faradaic current. At higher potentials (ca. 2.8 V) also BMP^+ fragments start to evolve, but with very low intensity and thus very low rate. Considering the signal-to-noise ratio, there is no significant difference between the onset potentials of the two electrode materials. As proposed recently,[110] the decomposition of BMP^+ at these anodic potentials might be induced by

reaction with active species that are formed during the electrochemical oxidation of the $TFSI^-$ anion.

The reaction pathways for $TFSI^-$ decomposition proposed from the results of the DFT calculations for the cathodic decomposition[39] (Figure 30) cannot directly be transferred to the anodic decomposition as the latter tests the decomposition induced by the removal of an electron, whereas the former calculate the decomposition upon addition of an electron. Nevertheless, the electrochemical oxidation results in the same decomposition products and / or related fragments, indicating that the decomposition pathways are likely the same as for cathodic decomposition.

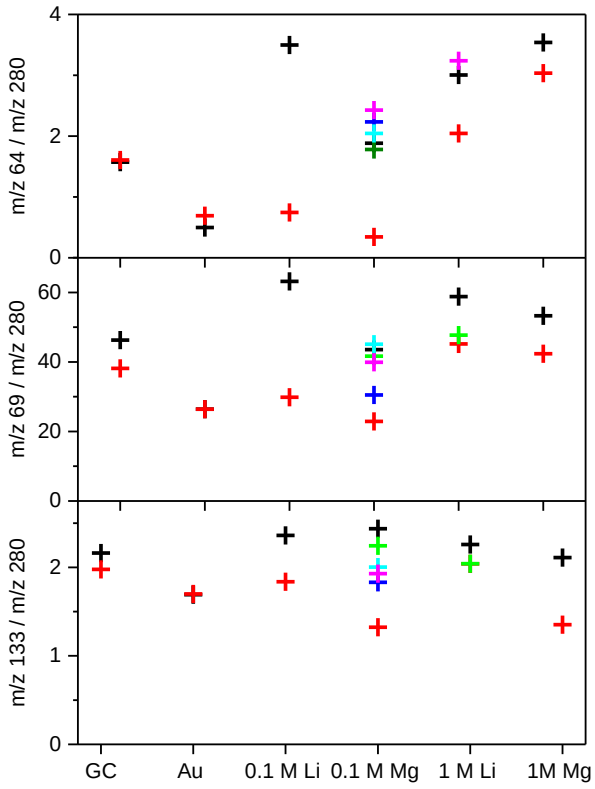


Figure 34: Relative intensities of m/z = 64, 69 and 133 to m/z = 280 on Au and GC electrodes as well as in Li(TFSI) and Mg(TFSI)2 containing BMP-TFSI on an Au WE, measured at that anodic potential, the value was stable. The points show repeated measurements under allegedly identical conditions, similar colours in the upper and lower panel indicate that the points are related to the same measurement.

Figure 34 shows the relative intensities of the different $TFSI^-$ fragments or decomposition products (m/z = 64, 69, 133), relative to that of the TFSI molecule ion (m/z = 280). These relative intensities are constant throughout the anodic decomposition, indicating that the potential dependence of the different reaction pathways is identical. Therefore, we assume that also the reaction pathways do not change with potential. For all signals, however, the relative intensities are higher on the GC electrode than on the Au electrode. Since the fragmentation in the ion source for incoming $TFSI^-$ ions (m/z = 280) should be independent of

the electrode material, the additional amounts of fragments at m/z = 64, 69 and 133 are due to the previous electrochemical decomposition. Obviously, the GC electrode is (relatively) more active for catalytic decomposition of the molecule ion than the Au electrode. The most pronounced difference is found in the intensity ratio of the m/z = 64 and m/z = 280 signals, which is 2.5 times higher on GC than on Au. Hence, the pathway leading to the SO_2 fragment (m/z = 64), possibly via separation of one F^-, forming a CF_2 group, and subsequent stabilization of the reaction intermediate by shifting the CF_2 group to the central N, and finally bond breaking between N and the S of the SO_2 group,[39] is especially enhanced on the GC electrode. The difference in the relative intensity the m/z = 69 fragment indicative of the splitting of the CF_3 group is less pronounced (1.6 times more on GC).

Summing up, at cathodic potentials reaction pathway R6 (formation of CF_3) is favored for both electrode materials compared to the other pathways. Furthermore, on GC also the $TFSI^-$ molecular ion is observed, indicating that this is getting volatile as well, most likely via formation of a volatile molecular species. At anodic potentials, reaction pathway R5 (resulting in SO_2 formation) is especially enhanced on the GC electrode.

3.3.3.3 Influence of the addition of Li^+ and Mg^{2+} salts

In the third part, we present our results on the influence of Li^+ and Mg^{2+} on the stability / decomposition of BMP-TFSI at a Au electrode, using two different concentrations (0.1 M and 1 M).

Figure 35 shows the cathodic scan in 0.1 M and 1 M $Mg(TFSI)_2$ as well as in 0.1 and 1 M Li(TFSI) containing BMP-TFSI. For comparison, we also include the measurement in neat BMP-TFSI without added salts (see section 3.3.3.1). Interestingly, the results varied much more between different measurements when Li(TFSI) and $Mg(TFSI)_2$ were added to the electrolyte than in the absence of these salts. Also the potential of the reference electrode, which in neat IL varied only by ± 0.1 V at most, became less stable after the addition of the Li^+ and Mg^{2+} salts. This is tentatively attributed to variations in the water content introduced by the respective salts, as these are known to carry water, which cannot be removed by pumping as easily as for the pure IL. For better visibility, we only show a single set of representative data in Figure 35 and Figure 36. Note that the determination of the normalized intensities, normalized to the ion current of the molecular m/z = 280 ion (see Figure 34), is not affected by the reference electrode potential, since they were approximately potential independent.

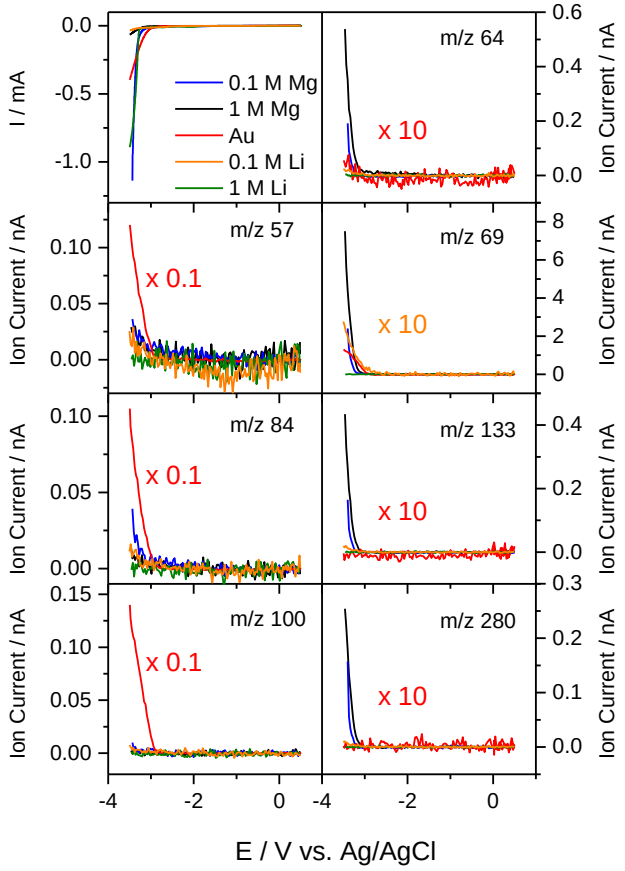


Figure 35: Faradaic current (top left) and ion currents attributed to the cation (left: m/z 57, 84, 100) and the anion (right: m/z = 64, 69, 133, 280) decomposition recorded during the first cathodic potential scan in BMP-TFSI (red), 0.1 M Mg(TFSI)2 in BMP-TFSI (blue), 1 M Mg(TFSI)2 in BMP-TFSI (black), 0.1 M Li(TFSI) in BMP-TFSI (orange) and 1 M Li(TFSI) in BMP-TFSI (green) (scan rate 10 mV s-1) on a Au electrode.

For pure BMP-TFSI the Faradaic current is due to the electrochemical decomposition of the IL (mainly BMP^+). This is indicated by the related ion currents, which appear simultaneously with the onset of the Faradaic current (see also section 3.2.3.1). In Li^+ containing IL deposition of Li takes place as well,[47] which is evidenced by the Faradaic deposition and stripping currents (see Supplementary Information). Surprisingly, the signals for BMP^+ decomposition products are either drastically smaller in the presence of Li^+ ions, e.g., by at least by a factor of ~50 for m/z = 57 in 0.1 M Li^+ containing electrolyte, than in the measurements in neat BMP-TFSI, or cannot be detected at all in the 1 M Li^+ containing electrolyte. Considering the rather high Faradaic currents at high Li^+ concentration, we conclude that BMP^+ decomposition is strongly hindered by the presence of Li(TFSI) in the electrolyte. The decomposition of the $TFSI^-$ anion, which is indicated by the m/z = 69 signal in neat BMP-TFSI, can also be found in the 0.1 M Li^+ containing electrolyte, although with lower intensity. The influence of the Li^+ addition is, however, much less than for the BMP^+ cation. For the higher Li^+ concentration (1 M), also the signals for the $TFSI^-$ fragments are below the detection limit.

In contrast to the addition of Li(TFSI), we do not find any indication for significant amounts of reversible Mg deposition (plating) and stripping from $Mg(TFSI)_2$, as indicated by the lack of corresponding anodic currents. This agrees fully with previous findings that Mg^{2+} deposition from $Mg(CF_3SO_3)_2$ salts is inhibited in BMP-TFSI.[164] Both in 0.1 M and 1 M $Mg(TFSI)_2$ solution the ion currents of BMP^+ and $TFSI^-$ decomposition products go along with the onset of the Faradaic current, but the signals related to BMP^+ degradation are much lower compared to the experiment in neat BMP-TFSI and resemble more the measurements in Li^+ containing electrolyte. Also in this case the metal cation hinders the BMP^+ decomposition. The $TFSI^-$ related fragments, on the other hand, are even higher in intensity when Mg^{2+} ions are added, i.e., they promote the $TFSI^-$ decomposition. Thus, the relative intensities of the BMP^+ and $TFSI^-$ fragments are changed drastically in the presence of Mg^{2+}. Whereas in neat BMP-TFSI the highest signal for BMP^+ decomposition, the m/z = 84 ion current, is of the same order of magnitude as the most prominent TFSI fragment signal (m/z = 69), the latter is by two orders of magnitude higher than the m/z = 84 signal in Mg^{2+} containing electrolyte.

We suggest that this change in decomposition behaviour is likely related to the $TFSI^-$ coordination with the metal cations. Using Raman spectroscopy, Giffin et al. found that in BMP-TFSI based solutions the Mg^{2+} cation is coordinated to 3 to 4 $TFSI^-$ anions, while Li^+ is coordinated only to two $TFSI^-$ ions.[156,165] As predicted in theoretical studies, the coordination of the $TFSI^-$ anion to the metal cations decreases the stability of the anion against decomposition at reducing potentials: Rajput et al. determined from MD and quantum chemistry calculations that the Mg^{2+} cation forms a contact ion pair with the $TFSI^-$ in various solvents. At negative potentials, the Mg^{2+} cation of the ion pair is reduced at the Au electrode, which can activate the anion decomposition, most likely via splitting the C-S bond.[159] Breaking this bond was proposed to result in the release of CF_3, which is in good agreement with our finding that the m/z = 69 ion current has by far the most intense signal. In the case of Li^+, DFT-MD simulations showed that the $TFSI^-$ anion accepts electrons in the σ^* CF_3-S orbital and stabilizes by dissociation of CF_3. This is possible because of the formation of a specific chained network structure and a resulting shift of the electron affinity of the anions. By doing this, a stable SEI layer in highly concentrated Li(TFSI) containing acetonitrile is formed and the acetonitrile decomposition is suppressed.[158] This anion reduction hinders further decomposition of the electrolyte and thus increases the electrochemical stability,[158] which fully agrees with our observation that a small signal for m/z = 69 indicates some $TFSI^-$ degradation but that both BMP^+ and other $TFSI^-$ fragments are essentially absent in the mass spectra. Investigating the SEI formation formed in electrochemical measurements in Li(TFSI)

containing ILs via XPS subsequent analysis, Tulodziecki et al. found decomposition products of the $TFSI^-$ anion (LiF, Li_2CO_3, Li_2S, LiS_2O_4, $LiSO_3CF_3$, Li_2SO_3) on a Pt electrode surface after negative polarization.[162] Based on these results they concluded that the anion is destabilized by the presence of Li^+ in the electrolyte. The formation of a stable SEI with similar composition was also reported by Howlett et al., who investigated the Li plating and stripping from Li(TFSI) containing BMP-TFSI by XPS.[47] Yildirim et al. determined a strong interaction between $TFSI^-$ and the surface in an *ab initio* molecular dynamics study on the interplay between BMP-TFSI and a Li(100) surface, which they proposed to lead to the $TFSI^-$ reduction.[38] So, the absence of $TFSI^-$ decomposition products in our experiments in Li^+ containing BMP-TFSI is most likely not due to the stability of the $TFSI^-$ ion, but due to surface blocking by the formation and deposition of non-volatile decomposition products, which result in a passivation layer (possibly on top of some deposited Li), which hinders further IL decomposition.

The lower amount of BMP^+ decomposition products compared to neat BMP-TFSI found in our linear sweep voltammetry experiments, both in Li^+ and Mg^{2+} containing electrolytes, points to the existence of competing reduction pathways, where electron transfer occurs to the metal cations or to the $TFSI^-$ anion (due to the lower lying orbitals in the contact ion pairs) rather than to the BMP^+ cation. Nevertheless, in Mg^{2+} containing IL some BMP^+ decomposition is observed. To learn more about the influence of Mg^{2+} on the decomposition pathways, we plotted the ion currents of selected fragments of the Mg^{2+} containing electrolytes, relative to the m/z = 84 ion current, which is the main fragment of reaction pathway R1, in Figure 32. For the m/z = 57 ion current, there is little difference in this ratio between the Mg^{2+} containing BMP-TFSI and that in neat BMP-TFSI, considering the relatively large variations for the Mg^{2+} containing electrolytes in repeated measurements (see also above). The probability of splitting either the bond between the pyrrolidinium-ring and the methyl group or the butyl chain in the BMP^+ decomposition (pathways R1, R2) does not seem to be influenced by the presence of Mg^{2+} ions. In contrast, the decomposition pathway via ring opening (R3), is significantly less probable than in pure BMP-TFSI, indicated by the lower relative intensity of the fragment at m/z = 100.

For cathodic potentials we can compare only the relative intensities for the decomposition of 0.1 M and 1 M Mg^{2+} containing BMP-TFSI on Au (Figure 35) on the one hand and for the decomposition of neat IL on GC on the other hand (Figure 34), since they are the only ones showing sufficient signal intensity for a comparison of the relative intensities. For all of these measurements, despite variations in the absolute signal intensities, the relative ones are the

same within the precision of the measurements. For instance m/z 69 is about 15 times higher than m/z 64. Therefore, we conclude that there is only minor influence of the metal cation or the nature of the WE on the cathodic $TFSI^-$ anion decomposition pathways.

In summary, the addition of $Mg(TFSI)_2$ and Li(TFSI) hinders the cathodic decomposition of BMP^+. In the presence of Li^+ there is also only little formation of volatile $TFSI^-$ degradation products, whereas with Mg^{2+} their formation is largely enhanced. While the presence of Li^+ ions leads to the formation of a stable passivation layer, protecting the system against further reductive decomposition, we have no indication for this in the presence of Mg^{2+} ions. Finally, the data indicate that reversible Li deposition and dissolution is possible, while the corresponding processes are inhibited for the case of Mg^{2+} containing electrolyte.

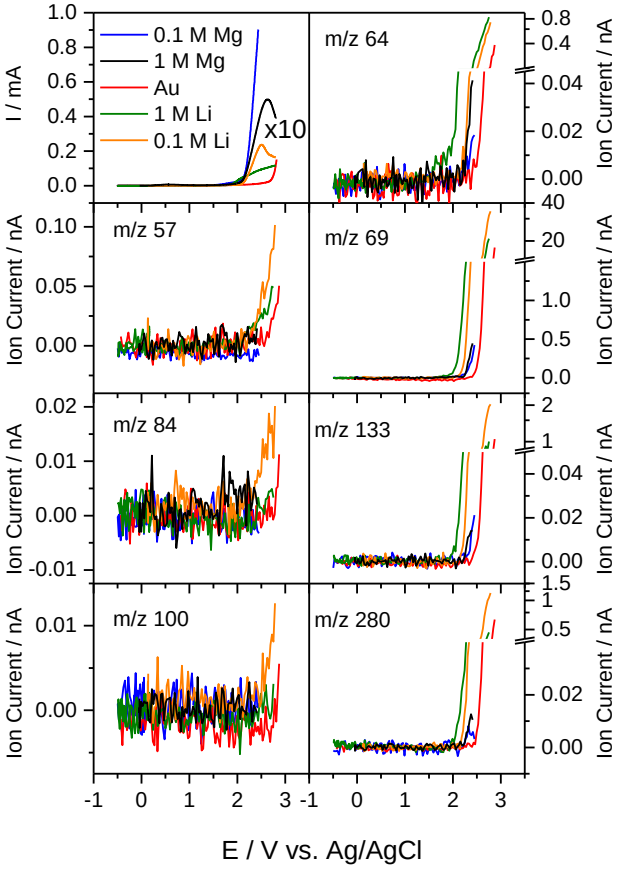


Figure 36: Faradaic current (top left) and ion currents attributed to the cation (left: m/z 57, 84, 100) and the anion (right: m/z = 64, 69, 133, 280) decomposition recorded during the first cathodic potential scan in BMP-TFSI (red), 0.1 M Mg(TFSI)2 in BMP-TFSI (blue) and 1 M Mg(TFSI)2 in BMP-TFSI (black)), 0.1 M Li(TFSI) in BMP-TFSI (orange) and 1 M Li(TFSI) in BMP-TFSI (green) (scan rate 10 mV s-1) on a Au electrode.

Figure 36 displays the anodic decomposition of $Mg(TFSI)_2$ and Li(TFSI) containing BMP-TFSI and, for comparison, that of the neat IL at a Au electrode. Different from the results in pure IL, we find a Faradaic current peak with a maximum in the potential region between 2.5 – 2.6 V both in Mg^{2+} and in Li^+ containing electrolyte. The height of the peak, however, does

not seem to correlate with the concentration of the added salt, i.e., it is 2.5 times higher when increasing the salt concentration by a factor of 10. Therefore, we tend to exclude that this peak is caused by the oxidation of impurities in the salts, since in that case one would expect a more pronounced increase of the peak height with increasing salt / impurity concentration.

For more information on the nature of this peak, we again look at the ion currents in this potential region. Since the onset of both BMP^+ and $TFSI^-$ related decomposition products is at higher potentials than the onset of the Faradaic current and since the peak shape is not reflected in the shape of the ion currents, we conclude that the peak in in the Faradaic current is dominated by other processes than the decomposition of the IL.

Considering the anodic decomposition of the IL cation or anion, we obtained pronounced signals for the $TFSI^-$ related fragments at m/z = 64, 69, 133 and 280. For BMP^+ decomposition (m/z = 57, 84, 100), in contrast, we obtained only small ion currents in Li^+ containing electrolyte, and they are below the detection limit in Mg^{2+} containing electrolyte. Obviously, the decomposition of TFSI is the predominant process at high potentials. This observation is in line with our previous finding for the decomposition of neat BMP-TFSI at anodic potentials, which was dominated by decomposition of the anion, and the small currents of the BMP^+ cation related fragments were supposed to result from radical reactions induced by the $TFSI^{\bullet}$ radical formed at highly positive potentials.[110]

For more detailed and accurate statements about the decomposition mechanism at anodic potentials, we included in Figure 34 also the relative intensities of the m/z ion currents related to $TFSI^-$ decomposition, normalized to that of the m/z = 280 molecule ion, within the same measurement. For the relative intensity of the m/z = 133 signal, the values are in the same range in all different electrolytes, considering all measurements. Apparently, the scission of the N-S bond is either not affected by the addition of the metal salts or this bond is only split by the electron impact in the ion source of the MS. The relative intensity of the m/z = 69 signal is similar for all metal salt containing electrolytes, but higher than for the pure IL. In this case, the separation of a CF_3 group seems to be enhanced by the presence of Li^+ and Mg^{2+} at anodic potentials. For the m/z = 64 signal the addition of both Li^+ or Mg^{2+} salts leads to an increase of its intensity, and this depends also on their concentration. Higher metal ion concentrations result in higher m/z = 64 ion currents, on a relative scale. Apparently, the metal ions promote the reactivity for the oxidative decomposition along the reaction pathway R5 (Figure 30).

In summary, the presence of Li^+ and Mg^{2+} destabilizes the $TFSI^-$ anions towards the anodic decomposition, which results in an earlier onset of the Faradaic current and a relative amount of smaller decomposition products/fragments.

3.3.4 Conclusions

Aiming at an improved mechanistic understanding of the electrochemical decomposition of BMP-TFSI in battery relevant electrolytes, in the absence and presence of Li^+ and Mg^{2+} ions on Au and GC electrodes, we have investigated this process in linear sweep voltammetry half-cell measurements, using a DEMS setup specifically designed for studies of Ionic Liquids. Based on these data we arrive at the following conclusions:

1. The reductive decomposition of BMP-TFSI on Au results in the simultaneous formation of both BMP^+ and $TFSI^-$ decomposition products with about equal intensities of the respective main fragments. The BMP^+ degradation proceeds via splitting of the alkyl side chains and via ring opening at the same potentials. Also at anodic potentials both BMP^+ and $TFSI^-$ decompose, but in this case the decomposition of $TFSI^-$ is the predominant process, which proceeds mainly by splitting the C-S bond.
2. Varying the electrode material (Au and GC) has only a minor effect on the stability window of the IL. It does, however, affect the decomposition mechanism and the relative amount of the different decomposition products: At cathodic potentials the GC electrode promotes the $TFSI^-$ decomposition, which becomes the dominant process. Within the $TFSI^-$ decomposition products, CF_3 prevails, but in contrast to Au also other fragments such as SO_2 are formed and also the molecular ion can be detected. For the BMP^+ decomposition GC enhances the scission of the bond between the N atom and the butyl side chain. Similar to Au, $TFSI^-$ degradation is the main process. At anodic potentials on the GC electrode, SO_2 formation is enhanced compared to the other $TFSI^-$ decomposition products.
3. The addition of Mg^{2+} not only destabilizes the $TFSI^-$ anion against the reductive decomposition, so that the product distribution is shifted from mostly BMP^+ fragments in neat BMP-TFSI to mostly $TFSI^-$ fragments, but it additionally hampers the BMP^+ decomposition. Furthermore, Mg^{2+} deposition is inhibited by strong interactions between $TFSI^-$ anions and Mg^{2+} ions. The addition of Li^+, in contrast, largely hinders the formation of volatile BMP-TFSI decomposition products and thus the formation of a stable SEI layer, while Li deposition / dissolution is possible.

Overall, these data demonstrate the potential of spectro-electrochemical studies such as this DEMS study for an in depth understanding of the electrochemical stability and decomposition of battery electrolytes, which is essential for the systematic development of improved electrolyte systems.

3.3.5 Supporting information

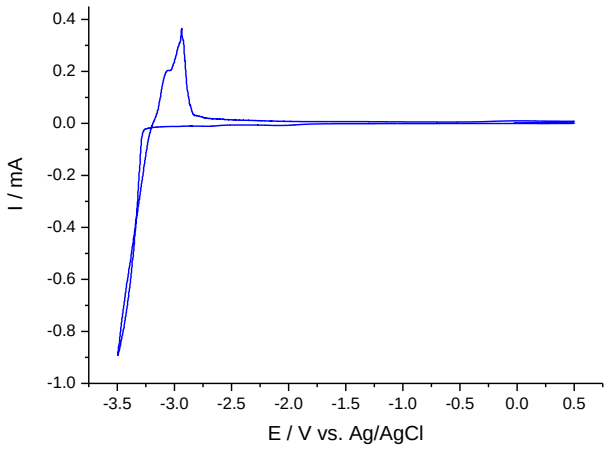


Figure 37: CV of 1 M Li(TFSI) in BMP TFSI on a Au electrode.

3.4 Influence of additives on the reversible ORR / OER in the magnesium containing ionic liquid N-Butyl-N-methylpyrrolidinium bis(trifluoromethane-sulfonyl)imide

The content of this chapter was published in reference [166] and is reprinted with permission by ChemSusChem / John Wiley and Sons (ChemSusChem 2020, 13, 3919-3927 / 10.1002/cssc.202000672). The experimental section was removed and the information was added to the experimental part in chapter 2 of this work. The style and numbering of the references and the figures have been adapted to fit the layout of the thesis. All measurements were planned by Markus Eckardt and me. DEMS measurements were performed by Markus Eckardt, Monja Schilling, Cecilia Flores and me. The evaluation of the DEMS data as well as the creative process of the publication was done by Markus Eckardt and me. The Karl Fischer titration was performed by Hanno M. Schütz and me. The SEM and EDX measurements were performed by Alexander Minkow. This work was financially supported by the Deutsche Forschungsgemeinschaft via project Be 1201/22-1 and the German Federal Ministry of Education and Research (BMBF) in the project 03X4636C ("Li-EcoSafe – Entwicklung kostengünstiger und sicherer Lithium-Ionen-Batterien") and 03EK3051C ("Verbundvorhaben LuCaMag: Wege zu sekundären Mg/Ca ' Luftbatterien"). This work contributes to the research performed at CELEST (Center for Electrochemical Energy Storage Ulm-Karlsruhe).

3.4.1 Abstract

The influence of different additives on the oxygen reduction reaction/oxygen evolution reaction (ORR/OER) in magnesium-containing *N*-butyl-*N*-methylpyrrolidinium bis(trifluoromethanesulfonyl)imide (BMP-TFSI) on a glassy carbon electrode was investigated to gain a better understanding of the electrochemical processes in Mg-air batteries. 18-Crown-6 was used as a complexing agent for Mg ions to hinder the passivation caused by their reaction with ORR products such as superoxide and peroxide anions. Furthermore, borane dimethylamine complex (NBH) was used as a potential water-removing agent to inhibit electrode passivation by reacting with trace impurities of water. The electrochemical processes were characterized by differential electrochemical mass spectrometry to monitor the consumed and evolved O_2 in the ORR/OER and determine the number of transferred electrons. Crown ether and NBH efficiently masked Mg^{2+}. A

stochiometric excess of crown ether resulted in reduced formation of a passivation layer observed but if the concentration was too high the reversibility of the ORR/OER was reduced.

3.4.2 Introduction

The physical limitations of Li-ion battery systems have motivated the search and development of new batteries with potentially higher energy densities and based on more abundant materials. Most prominent, secondary metal-air batteries are seen as the next step for increasing energy density, ecology, and economy of energy storage compared with Li-ion batteries.[20,167,167-176] Using air-based cathodes can increase the theoretical energy density by replacing the commonly used cathode materials that contain large amounts of, for example, cobalt and nickel, with lighter materials. Here, the oxygen is provided by the ambient air while discharging, during which it is reduced to superoxide or peroxide species in the oxygen reduction reaction (ORR) and released again during charging by the oxygen evolution reaction (OER).[20,174-176]

Promising next generation battery systems are secondary Mg-air batteries in which the lithium is replaced by magnesium, which is not only more abundant than lithium but also has advantages regarding safety aspects.[14,154,155] Additionally, the volumetric capacity of magnesium exceeds that of lithium by almost a factor of two.[155] However, the slow reaction kinetics of magnesium intercalation/insertion in the Mg-air battery reactions are largely caused by the slow diffusion of Mg in the anode.[154] Furthermore, the formation of stable magnesium oxides in the presence of water strongly limit the reversibility of Mg-air batteries.[14] This “breathing” and therefore open battery system causes specific demands for the electrolyte, which should neither evaporate from the battery nor be sensitive to air. Furthermore, the stability of the electrolyte towards reduction products that are formed during the ORR is a key factor.[177-179]

Ionic liquids (ILs) seem to be a good choice as electrolytes as they provide the required stability and a low vapor pressure.[1,111-114] However, applying ILs as electrolytes for Mg-air batteries (IL containing Mg^{2+}) has been shown to result in a slow deposition/ dissolution of Mg on the anode and a strong passivation on the cathode, whereby the latter results in a strongly limited ORR/OER reversibility.[51,63,64,78,164,180] Furthermore, on the anode side, strong interactions between Mg^{2+} and bis(trifluoromethanesulfonyl)imide ($TFSI^-$) were speculated to cause a high overpotential for Mg deposition, resulting in the decomposition of the electrolyte, which in turn leads to the formation of a passivating film on the anode.[145,164] It is well known from previous studies that the Mg plating and stripping characteristics can be

improved by the use of additives.[13,15,181] However, their influence on the cathode reactions (ORR/OER) is largely unknown. For Li-air batteries, the addition of barium ions to the Li^+-containing electrolyte was reported to show promising effects on the discharge capacity, which was attributed to the incorporation of Ba^{2+} in the Li_2O_2 lattice.[182] For Mg-air batteries, we are not aware of any data on the influence of additives on the cathode reactions in aprotic electrolytes. In the present study, we investigated the influence of additives on the cathode reactions in Mg-containing electrolytes, more specifically, on their impact on the passivation of the electrode and the ORR/OER reversibility.

We characterized the influence of the complexing agent 18-crown-6 and the water-removing additive borane dimethylamine complex (NBH) on the ORR/OER in 0.1 M $Mg(TFSI)_2$-containing *N*-butyl-*N*-methylpyrrolidinium bis(trifluoromethanesulfonyl)imide (BMP-TFSI) on a glassy carbon (GC) electrode. The measurements were performed in an electrochemical flow cell, employing online mass spectrometry analysis (differential electrochemical mass spectrometry (DEMS))[51,78,183] of the O_2 content of the electrolyte. This allowed us to determine the amount of O_2 consumed and evolved in the ORR and the OER, respectively, and calculate the number of electrons transferred per O_2 molecule in the reaction, which provides detailed insights into the processes on the electrode.[51,78,183]

The solubility of $Mg(TFSI)_2$ in THF-based electrolytes has been improved with the addition of 18-crown-6, which also leads to an increase in the ion conductivity.[184] Using the IL *N*-methyl-*N*-propylpiperidinium-TFSI (PMP-TFSI), a promoting effect on the Mg plating was reported by Sagane et al. for a $Mg(TFSI)_2$/PMP-TFSI=1:5 mol electrolyte.[181] However, little is known about the influence of 18-crown-6 on the ORR/OER reversibility and the passivation of the cathode surface. Complexing Mg^{2+} on the cathode side might help "masking" of the magnesium ions for the ORR, mimicking a Mg^{2+}-free electrolyte and, thus, hindering or even suppressing the formation of a passivation layer. This would allow a reversible ORR/OER, as observed in neat BMP-TFSI.[49,51,78,183] In that electrolyte, the ORR proceeds in two reaction steps, forming superoxide first, followed by the formation of peroxide at lower potentials.

Considering the effects of trace impurities of water, residual water in the electrolyte was shown to have a promoting effect on ORR in aprotic electrolyte.[24,183,185,185] It also enhances the formation of non-oxidizable magnesium peroxides and oxides in Mg^{2+}-containing electrolyte in the ORR, thus passivating the electrode.[14] Therefore, we also explored the effect of boron hydride as a water removing additive in the electrolyte. Boron hydride is known to

react with H_2 and form borate in contact with water, and this way efficiently removes traces of water.

In the following, after a brief description of the experimental set-up and the used electrolytes, we start with a short description of the influence of $Mg(TFSI)_2$ on the ORR/OER in BMP-TFSI, which will be used as a reference for the following systems (first section). Next, we present and discuss the results obtained on the influence of the 18-crown-6 complexing agent (second section) and the water-removing NBH additive (third section). Finally, in the last section, we summarize the most important findings obtained in this work.

3.4.3 Results and discussion

3.4.3.1 Influence of $Mg(TFSI)_2$ on the ORR in BMP-TFSI

The addition of magnesium in the form of $Mg(TFSI)_2$ to BMP-TFSI introduces significant changes in the ORR/OER behavior on GC electrodes, as shown earlier by our group.[51,63,64,78] This is illustrated in Figure 38, which shows results of a potentiodynamic DEMS measurement performed in a potential window of -1.4 to 1.4 V versus Mg/MgO in neat BMP-TFSI (a-c) and in 0.1 M $Mg(TFSI)_2$ containing BMP-TFSI (d-f). Both times we show the 1st and the 4th cycle. In the cyclic voltammogram (CV) (Figure 38) we find distinct ORR currents starting at potentials below 0.4 and 0.7 V, respectively. In the positive-going scan, low faradaic current densities starting at approximately 0.4 V were observed. However, the charge transferred in the OER was much lower than that transferred in the ORR. This was mainly caused by the experimental conditions, because in the flow cell setup the products of the ORR are transported away from the electrode and, thus, cannot be oxidized again in the OER.[51] Therefore, this setup is not well suited to reproduce the ORR/OER reversibility in real battery systems, in which the ORR products can diffuse back to the electrode surface for further oxidation in the absence of any electrolyte flow. In the present experiments, it was not possible to detect the O_2 evolution by mass spectrometry owing to the low amounts of O_2 formed in both pure and $Mg(TFSI)_2$-containing BMP-TFSI. This is in contrast to results in our previous study,[51] in which we used a lower flow rate. As already discussed earlier,[51,63,78,183] two plateaus were observed in the measured ORR signal in pure BMP-TFSI, whereas the consumption of O_2 does not change in the measured potential window of the ORR (see Figure 38). The first plateau appeared between 0.25 and 0 V, which we assumed to correspond to a one-electron transfer, as shown in Figure 38. Therefore, in this potential range

superoxide is formed during O_2 reduction.[49,186,187] Between -0.6 and -1.2 V a second plateau appeared with approximately twice the current density, which corresponds to a two-electron transfer and thus related to the formation of a peroxide.[51,183,188] Decreasing the potential further resulted in an increase in the current density with unchanged oxygen consumption. Therefore, we attribute the current increase to side reactions such as the decomposition of the IL or reduction of residual water impurities in the electrolyte.[51,145,183]

Comparing the ORR in pure BMP-TFSI with the ORR in $Mg(TFSI)_2$-containing IL, a much lower ORR current density was observed in the first cycle. However, there seemed to be two current plateaus, one between 0 and -0.5 V and the other appears to start at -0.9 V. However, in this case the current quickly decayed at more negative potentials. The oxygen consumption stayed approximately constant in the ORR potential window. In the presence of $Mg(TFSI)_2$, the number of electrons transferred was approximately 1.5 in the potential region of the first plateau, indicating that the product at least partly consisted of superoxides. We cannot specify whether the additional electrons come from partial formation of peroxides or other side reactions with the electrolyte. In the lower potential range below -0.5 V the electron transfer rapidly increased up to > 4 e^- per O_2 molecule. The side reactions clearly played a role and seem to result in a passivation of the electrode surface. These results agree with findings in previous studies, which have reported that magnesium superoxide and magnesium peroxide are formed in this electrolyte, with the latter the dominant product under most reaction conditions.[51,63,64,78] Even though a quantitative comparison of the current densities was not possible because of the differences in the O_2 content in the electrolyte in different measurements, the current densities in the $Mg(TFSI)_2$-containing electrolyte were much smaller than in the Mg-free electrolyte. In both electrolytes, in the presence and absence of $Mg(TFSI)_2$, superoxide species were formed at lower overpotentials in the ORR whereas at more negative potentials more electrons were transferred, indicating peroxide formation. After 4 cycles, the ORR was barely visible in the CV in Figure 38, and the *m*/*z* 32 signal for O_2 does not show any oxygen consumption in the fourth cycle. Apparently, the ORR was inhibited by the formation of an ORR- and OER-inactive passivation layer on the electrode. This passivation of the electrode is a major drawback of this IL electrolyte for Mg-air batteries. Interestingly, passivation seems to be less of a problem in other aprotic electrolytes such as perchlorate in DMSO[65] and in Mg^{2+}-containing THF, in which peroxide is predominantly formed upon reduction, presumably by an electrochemical one-electron reduction to superoxide, followed by a chemical reduction step to peroxide.[189-191]

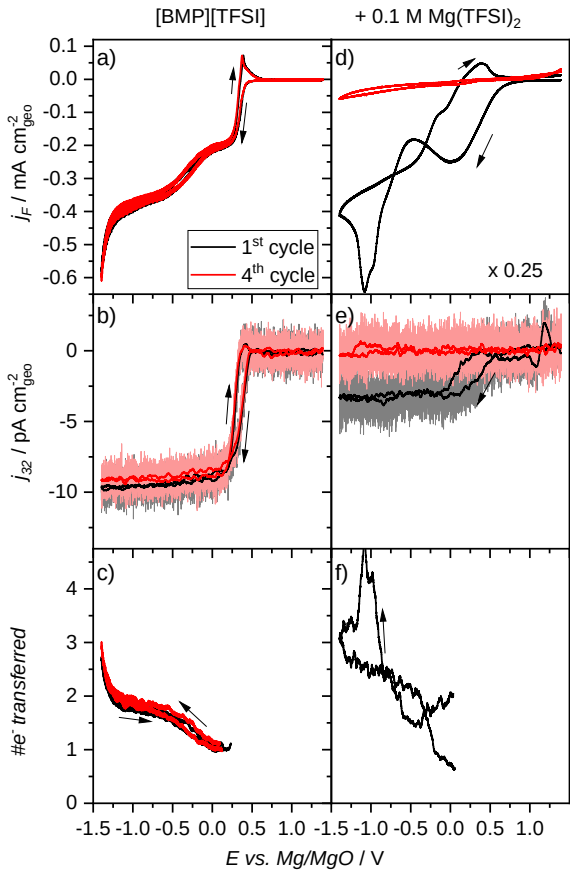


Figure 38: ORR / OER on glassy carbon in O_2 saturated (a-c) neat BMP-TFSI and (d-f) 0.1 M $MgTFSI_2$ containing BMP-TFSI.

3.4.3.2 ORR/OER in the presence of crown ether additive

Additives such as crown ethers can help mask the magnesium by complexation and possibly suppress or even inhibit the formation of a passivation layer. ORR/OER measurements in electrolytes containing 18-crown-6 as complexing agent are presented in Figure 39. The ORR/OER in a 1:1 $Mg(TFSI)_2$/18-crown-6 electrolyte is shown in Figure 39. Theoretically, this should result in full complexation of Mg^{2+}, provided every Mg^{2+} ion is complexed by one crown ether molecule, for 0.1 M 18-crown-6 and 0.1 M $Mg(TFSI)_2$.[184] In contrast to an improved ORR/OER performance and reversibility we expected, we obtained a faster passivation, with the electrode fully passivated in the second cycle. Additionally, we obtained a peak at approximately -0.2 V in the first cycle, which is correlated with O_2 consumption and corresponds to the ORR. Such a peak was not observed in the 0.1 M $Mg(TFSI)_2$ electrolyte without addition of crown ether. In this peak the number of transferred electrons was approximately 1, in agreement with superoxide formation (Figure 39). At more negative potentials, below approximately -0.5 V, the current passes through a minimum and then

increases slowly up to the negative potential limit. In this range the number of electrons transferred per O_2 slowly increased to approximately 2. This is compatible with a slow transition from superoxide formation to peroxide formation, although reductive side reactions are also likely, causing the extended passivation of the electrode surface in this electrolyte. Different from the case of additive-free electrolyte, there is no indication of an OER signal in the positive-going scan (Figure 39), indicating the formation of a stable passivation layer. Clearly, stoichiometric amounts of 18-crown-6 accelerate the passivation of the glassy carbon electrode instead of lowering it.

The effect of the crown ether changed if its concentration was increased to a $MgTFSI_2$/18-crown-6 ratio of 1:2 (Figure 39). Most noticeable is the high current density in the first cycle, which exceeds that obtained in the crown ether free 0.1 M $MgTFSI_2$ electrolyte (see Figure 38) by more than a factor 5. This is likely to be related to an efficient complexing and masking of the Mg ions, resulting in a less efficient passivation, at least in the first cycle. This high current density in the first cycle is followed by a pronounced decay below -0.7 V. In the second cycle, the current densities are small compared with the first cycle, but they do not change much after the second cycle up to the fourth cycle. The number of transferred electrons in the negative-going scan of the first cycle is between 3 and 4, indicating preferential formation of (su)peroxide plus some contributions either from magnesium oxide formation or other side reactions. In the subsequent cycles, the transfer of only approximately 2 electrons per O_2 molecules in the negative-going scan points to the formation of peroxides (Figure 39). The observation of peroxide formation without continuing passivation could be a consequence of Mg^{2+} complexation, hindering the formation of magnesium peroxide, although peroxides are formed continuously. Clearly, at these high concentrations, the crown ether can efficiently complex the Mg ions, which are no longer directly coordinated to peroxide ions. Therefore, mainly peroxides without direct coordination to Mg^{2+} ions are formed, as it was the case in pure BMP-TFSI, which do not passivate the electrode surface. Considering the number of transferred electrons of up to 3 in the potential region 0 to -0.7 V, the strong passivation in the first negative-going scan at potentials < -0.7 V, which is evident both from the Faradaic current and from the mass spectrometric O_2 signal, can be tentatively explained by the formation of magnesium oxide. Presumably, the formation of magnesium oxide is not suppressed by the crown ether because of a stronger binding of O^{2-} to Mg^{2+}, and hence a lower solubility product as compared with binding to the crown ether, whereas for MgO_2 formation this seems to be opposite.

The reversibility of the ORR/OER benefits greatly from the addition of higher concentrations of the crown ether. In the positive-going scan of the first cycle, the OER appears as a sharp peak at 0.5 V, which is getting broader and shifts to about 0.7 V in the next cycle where it remains in the following cycles. Our interpretation is confirmed by the mass spectrometric data, which show a clear *m*/*z* 32 signal in parallel to these peaks (Figure 39). Interestingly, the total charge in the OER related peaks is almost constant in the different cycles, indicating that the absolute amount of re-oxidizable ORR products remains constant.

The presence of the OER signal points to the formation of a partly oxidizable layer on the electrode after the reductive scan. This can be explained by the formation of oxidizable peroxide species in the ORR rather than the formation of the passivating magnesium peroxide species. Integration of the Faradaic ORR and OER current signals in the second and fourth cycle show a ratio of approximately 2:1 (ORR/OER). Therefore, despite the electrolyte flow, approximately half of the reduced oxygen species is essentially deposited on the electrode in this layer. The remaining part is either transported away with the flowing electrolyte or it is present in an inert, nonoxidizable state. Because the passivation stops after the first cycle, we favor the former explanation, at least after the first cycle. In the OER peak, the number of transferred electrons is about 1.3, which is a comparable order of magnitude as the number of electrons transferred per O_2 in the ORR (>1). The reversibility of the ORR/OER process indicates that there are indeed contributions from reversible peroxide formation and re-oxidation in the ORR/OER.

The addition of stoichiometric excess of 18-crown-6 to the electrolyte improves the ORR/OER characteristics. Therefore, we further increased the relative amount of the crown ether to a $MgTFSI_2$/18-crown-6 ratio of 1:10, which again resulted in significant changes in the ORR/OER (Figure 39). The main difference is the absence of the passivation peak in the first cycle. The current densities in the second cycle are similar to those in the first cycle, and they are of similar order of magnitude as in the first cycle in the crown-ether-free electrolyte. The resulting CV closely resembles that obtained in pure BMP-TFSI, showing also a two-plateau system (green bars in Figure 39), a largely reduced passivation, and a clear OER signal. For the first plateau, the calculated number of electrons is approximately one. This number steadily increases with decreasing potential, reaching a value of approximately 2 in the range of the second plateau. In contrast to the measurements of the samples with lower amounts of crown ether in the electrolyte, the two-plateau structure is also remained in the subsequent cycles. Therefore, the presence of a high stoichiometric excess of crown ether in the electrolyte leads to a similar ORR behavior as in neat BMP-TFSI. In both electrolytes,

there is an increase in the electron transfer per O_2 with increasing overpotential in the ORR, which, in contrast to the electrolytes with no or lower concentrations of crown ether, persists after multiple cycles. Therefore, we expected that the same transition from superoxide to peroxide formation observed for the ORR in neat BMP-TFSI occurs in 1:10 $MgTFSI_2$/18-crown-6-containing electrolyte when scanning to more negative potentials. In contrast to the situation in 0.2 M 18-crown-6, we did not detect the formation of magnesium oxide (electron number above 2). Under these conditions, Mg^{2+} complexation appears to be sufficiently efficient to fully inhibit MgO formation. Similar to the reaction in neat BMP-TFSI, only peroxide and superoxide are formed, without formation of a passivating layer. In the second cycle, a distinct peak is observed at approximately -0.7 V in the negative-going scan, which was not present in the mass spectrometry O_2 signal. Therefore, it is most probably not part of the O_2 reduction itself. This peak vanishes after further cycling. Therefore, we attribute the peak to the reduction of impurities in the crown ether.

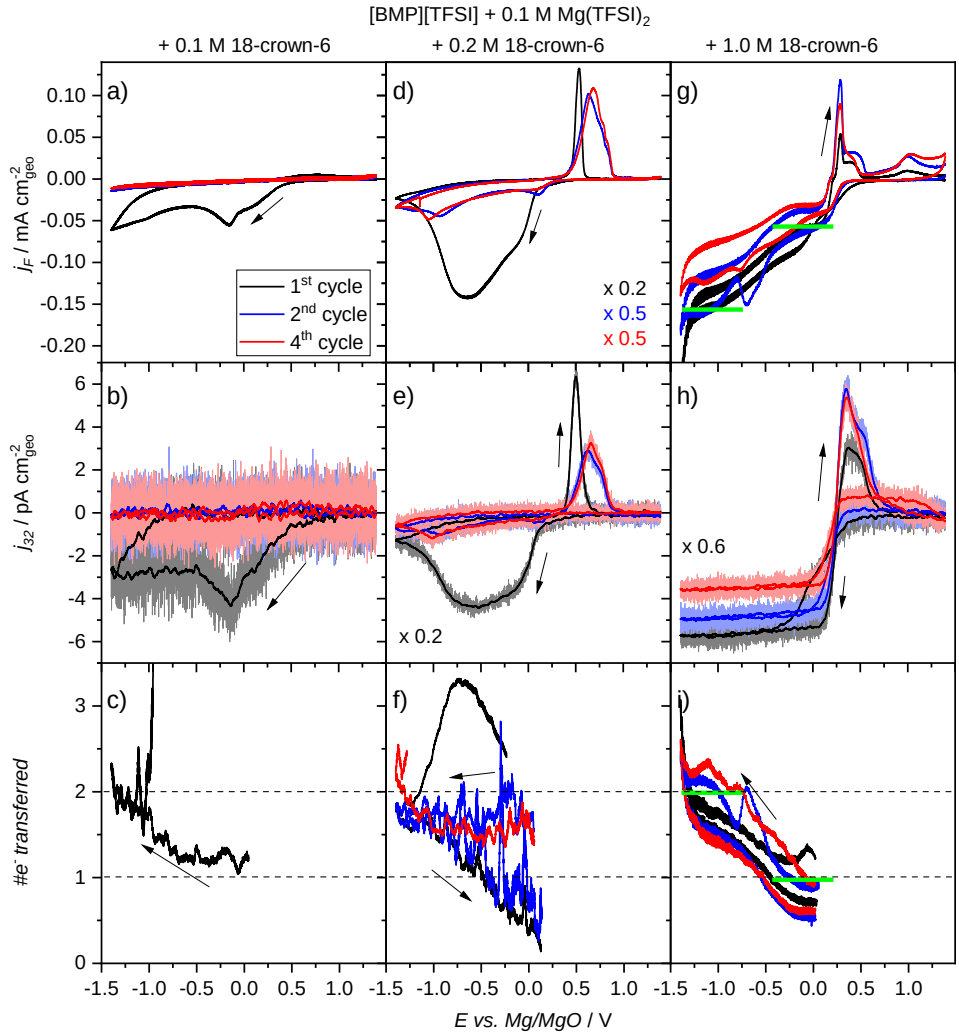


Figure 39: ORR / OER on glassy carbon in O_2 containing BMP-TFSI with 0.1 M $Mg(TFSI)_2$ and the complexing additive 18-crown-6 (a,b,c) 0.1 M, (d,e,h) 0.2 M, (g,h,i) 1.0 M.

A strong discrepancy between the integrated charges was observed at a ratio of approximately 10:1 (ORR/OER). This is much larger than the ratio of 2/1 that we obtained for the electrolyte with 0.2 M crown ether, but lower than for neat BMP-TFSI (300:1). We attribute the distinct difference between the two electrolytes, 0.1 M $Mg(TFSI)_2$ in BMP-TFSI and 1.0 M crown-ether-containing 0.1 M $Mg(TFSI)_2$ in BMP-TFSI, to the strongly suppressed formation of a surface layer containing Mg-superoxide, peroxide, and oxide, to the efficient complexation of the Mg^{2+}. This allows the ORR products to be flushed away more easily, thus, decreasing the amount of oxidized ORR products in the OER. Therefore, a high stoichiometric excess of crown ether is helpful for decreasing the passivation but also reduces the reversibility of the OER in the flow-cell. The latter aspect does not apply in the case of battery applications, in which electrolyte flow is absent and the ORR products can reach the electrode surface by diffusion. Positive effects of the addition of crown ether to IL-based electrolytes with TFSI

anions were also reported for Mg plating and stripping.[181,192] In that case, both plating and stripping are enhanced and the tendency for passivation is lowered, equivalent to an improved reversibility. This was explained by the (partial) displacement of TFSI anions from the Mg^{2+} coordination shell by the (stronger interacting) crown ether. This inhibits the formation of Mg^{2+}-$TFSI^-$ species, which were proposed to lead to TFSI decomposition upon electron transfer to the Mg^{2+} ion.[159] For the ORR, the stronger interaction between crown ether and Mg^{2+} is also favorable, as it reduces the formation of stable Mg^{2+} (su-)peroxide species. Finally, the calculated number of transferred electrons in the OER is approximately one, indicating that superoxide species are oxidized to O_2.

For further information on the influence of the crown ether on the electrolyte layer, we recorded SEM images of the surface obtained after 10 cycles ORR/OER in the absence and presence (1.0 M 18-crown-6) of crown ether (Figure 40). In the low-magnification images (Figure 40a), a distinct highly structured surface morphology is obtained when a 18-crown-6-free 0.1 M $Mg(TFSI)_2$ electrolyte was used, which is different from that of the GC substrate and, therefore, associated with a layer of magnesium oxide species on top of the GC. This is consistent also with the observation of Mg and O signals in EDX images (see the Supporting Information). Higher magnification reveals the formation of lengthy, rod-like structures (Figure 40b). Similar structures were reported by Bozorgchenani et al.[64] for 0.1 M $Mg(TFSI)_2$ in BMP-TFSI on a Pt surface. Adding the crown ether (1.0 M) resulted in different structures (Figure 40c). At higher magnification, a surface layer is observed, which seems to be thinner than the one obtained with the former electrolyte. This correlates well with the lower tendency for passivation and the increasing ORR/OER reversibility, supporting our previous claim that masking the Mg ions with crown ether reduces the amount of MgO_x in the surface layer and thus its passivating properties. Nevertheless, EDX measurements revealed the presence of oxidic magnesium species on these surfaces (Figure 40d), but significantly less than in the crown-ether-free electrolyte (Figure 42, Supporting Information).

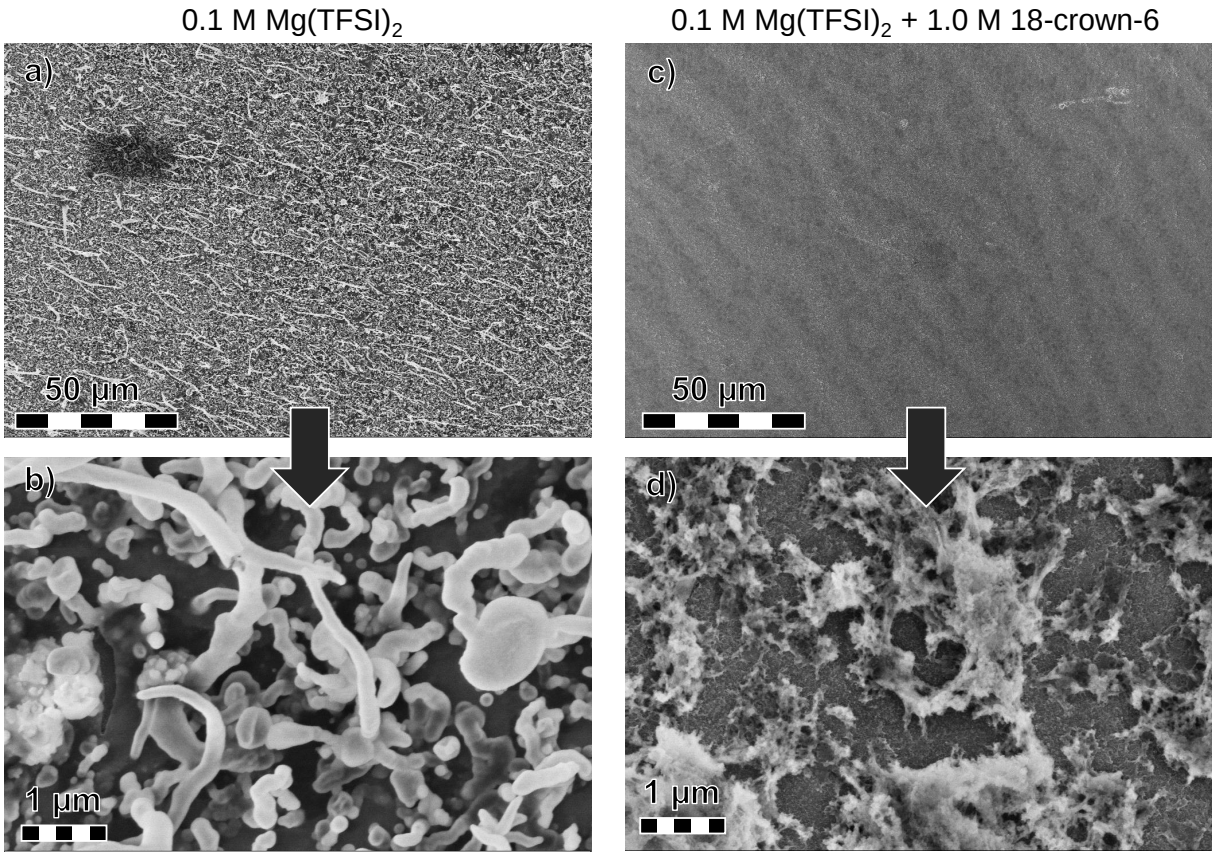


Figure 40: SEM images of the electrode surface after 10 ORR cycles (-1.4 – 1.4 V) in (a,b) 0.1 M Mg/TFSI)2 and (c,d) 0.1 M Mg(TFSI)2 and 1.0 M 18-crown-6 in BMP TFSI (4.00 kV).

Overall, the addition of crown ether in excess concentrations strongly influences the ORR/OER behavior in $Mg(TFSI)_2$-containing BMP-TFSI. The most important positive effect is the decreasing tendency for passivation as compared with only $Mg(TFSI)_2$-containing IL. The passivation process is slowed down considerably when crown ether is added in a tenfold excess to $Mg(TFSI)_2$. On the other hand, although high concentrations of crown ether are beneficial for suppressing the passivation, too high amounts (1.0 M) also lower the formation of oxidizable species such as Mg superoxides at or close to the electrode surface, which reduces the reversibility of the ORR and OER.

3.4.3.3 Drying agents

A major factor that contributes to the passivation of an electrode is residual water in the electrolyte; traces of water in magnesium-containing electrolytes are known to promote the formation of a nonoxidizable, passivating electrode layer in the ORR, consisting of magnesium oxide and peroxide.[14] Therefore, for the experiments presented in the previous sections, the electrolyte was dried before use in a UHV chamber to decrease the water

content. Efficient ways to keep the electrolyte dry are needed, especially for metal-air batteries, in which the electrolyte is in contact with air. In these cases, self-drying electrolytes are highly desirable. Such effects can be achieved by the addition of drying agents such as borohydrides to the electrolyte. We explored the effect of adding such a drying agent on the reversibility of the ORR/OER and on the electrode passivation. In the first step, we added 0.01 M NBH to the $Mg(TFSI)_2$-containing BMP-TFSI. In these cases, the electrolyte was used as-is, without prior drying in vacuum. The CVs recorded in NBH-free and in NBH-containing electrolyte are presented in Figure 41. Karl Fischer titration demonstrated that the addition of NBH reduced the water content of (non-dried) BMP-TFSI to 20 ppm, as compared with $Mg(TFSI)_2$-containing BMP-TFSI (25 ppm) and 0.1 M 18-crown-6+0.1 M $Mg(TFSI)_2$-containing BMP-TFSI ((35 ppm). The CVs in Figure 41 clearly illustrate the strong influence of the addition of NBH in the first cycle in the ORR (Figure 41a,d). The removal of water results in a significant increase of the ORR and OER current densities in the first cycle as compared with 0.1 M $Mg(TFSI)_2$ in BMP-TFSI electrolyte (see first section). However, for addition of 0.01 M NBH already the second cycle shows a similar extent of passivation as obtained in NBH-free electrolyte (Figure 38d). Furthermore, in the first cycle the ORR also shows a rather high number of transferred electrons of approximately 2 and above, whereas in the second cycle this decreases to approximately one transferred electron per O_2 molecule. This indicates the formation of magnesium peroxide, causing the strong passivation during the first cycle, but not to the same degree as the NBH-free electrolyte (see Figure 38d). The high current density in the first cycle could be owed to interactions between the $Mg(TFSI)_2$ and the NBH, which could lead to complexation of Mg^{2+}, similar to the behavior of crown ether discussed in the previous section. Interestingly, in the subsequent OER, there is only one electron transferred per O_2, which is consistent with a mechanism in which only the superoxide species can be re-oxidized. O_2 formation was not be observed for the oxidation of peroxide species to superoxides.

Increasing the concentration of NBH (Figure 41d,e,f) results in even higher current densities of the ORR, but not for the OER, in the first cycle. The first cycle is also dominated by the formation of peroxide (two-electron transfer), whereas in the subsequent cycles a one electron transfer to superoxide prevails. For this electrolyte, the lower potential limit was set to -1.1 instead of -1.4 V in the previous experiments (Figures 38-40) to not exceed the current density limitation of the flow cell. Significantly lower current densities are observed in the second cycle compared with the first cycle, indicative of surface passivation. Even though strong passivation is also observed for the 0.1 M NBH-containing electrolyte, the overall rate

of passivation is decreased significantly. This is illustrated by the measurable ORR currents even in the sixth cycle of the 0.1 M NBH-containing electrolyte (Figure 41d), in contrast to the essentially complete passivation in the 0.01 M NBH-containing electrolyte (Figure 41a). Furthermore, there is also an improved ORR/OER reversibility compared with the 0.01 M NBH-containing electrolyte, with a more pronounced OER peak at approximately 1.0 V, which appears in the second cycle, in contrast to the 0.01 M NBH electrolyte, for which the peak only appears in the first cycle. The measurable OER peak in the latter case is most likely related to stronger ORR signal the second cycle than in the 0.01 M NBH-containing electrolyte.

Integration of the ORR and the OER signals reveals an increase in the reversibility of these reactions with increasing cycle number, as indicated by their current densities, with a ratio of the ORR/OER charge of 3:1 in the second cycle, which changes to 1.7:1 in the sixth cycle. This is in agreement with a change in the number of transferred electrons in the OER from 1.4 in the second cycle to approximately 1 in the sixth cycle. This ORR/OER charge ratio is similar to that obtained for the 0.2 M 18-crown-6 containing dried electrolyte without the addition of NBH (see previous section). Additionally, the 0.1 M NBH electrolyte also shows an electron transfer number below one in ORR and OER in the fourth and sixth cycle. The reasons for such behavior, such as O_2 trapping and release in an interphase layer, can only be speculated upon.

The addition of borohydride shows a potential for improving the ORR/OER reversibility and for decreasing the rate of passivation. However, passivation is still pronounced and limits the improved reversibility to only a few cycles and short times. Most likely, this results from the lower amount of residual water in the electrolytes, which changes the composition of the surface layer formed on the electrode during the ORR, making it more oxidizable and, thus, suppressing the passivation of the electrode layer. However, we cannot rule out that NBH also acts as a complexing agent that could mask the Mg ions, similar to the crown ether. This is supported by the fact that 0.01 M NBH is sufficient to remove the residual water; therefore, there should be no major difference in the ORR/OER reaction behavior between the two NBH-containing electrolytes if it only acts as a water-removing additive. The ability of borohydrides to complex Mg ions has been reported.[193] Shao et al. have shown that the Mg plating and stripping behavior in different electrolyte strongly depends on the coordination of the electrochemically active Mg^{2+} species in the solution.[194] They reported enhanced Mg stripping when a combination of a chelating solvent and an increased BH_4^- concentration was used and explained this by synergetic effects.[194] Similar effects could be expected after the

addition of NBH to $Mg(TFSI)_2$-containing electrolyte, in which NBH adopts both roles, that of the complexing agent and that of the water-removing agent.

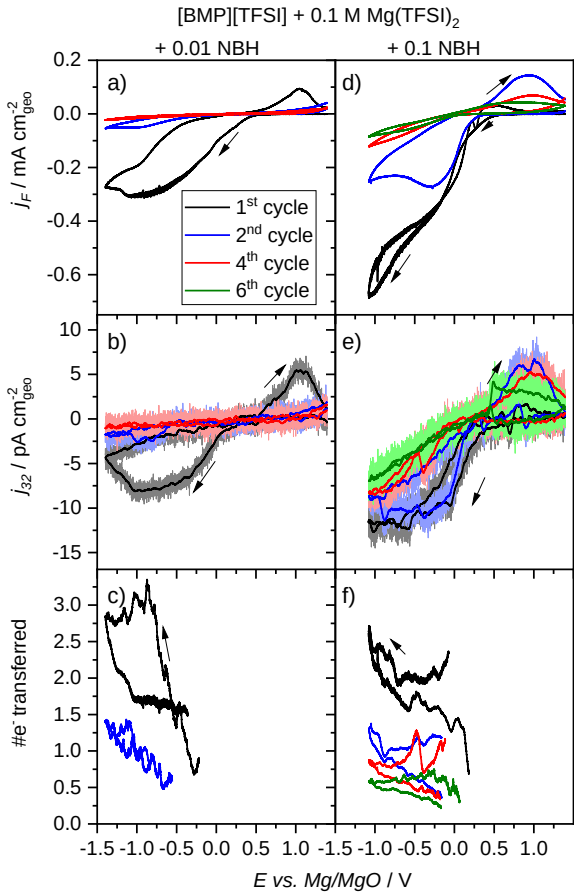


Figure 41: ORR / OER on glassy carbon in O_2 containing BMP-TFSI with 0.1 M $Mg(TFSI)_2$ and the NBH additive (a,b,c) 0.01 M, (d,e,f) 0.1 M.

Overall, the data indicate that a balance is required between minimizing the passivation (slow formation of the passivation layer at the electrode) and maximizing the reversibility (efficient formation of a layer of oxidizable ORR products on or close to the electrode surface). The lowest passivation was found for the 1 M crown-ether-containing electrolyte; however, the reversibility is rather limited (ORR/OER charge: 10:1). In contrast, the highest reversibility, with an ORR/OER charge of 1.7:1, was found in 0.1 M NBH-containing electrolyte; however, the passivation was much faster. Among the electrolytes investigated in this study, the 0.2 M crown-ether-containing electrolyte, with a Mg/crown ether ratio of 1:2, was the optimum choice, combining reasonable reversibility and limited passivation.

Finally, on a quantitative scale, the reversibility is expected to be different in a realistic battery cell as compared with the present flow cell measurements, as there would be no convection-induced off-transport of oxidizable ORR products. Additionally, compared with

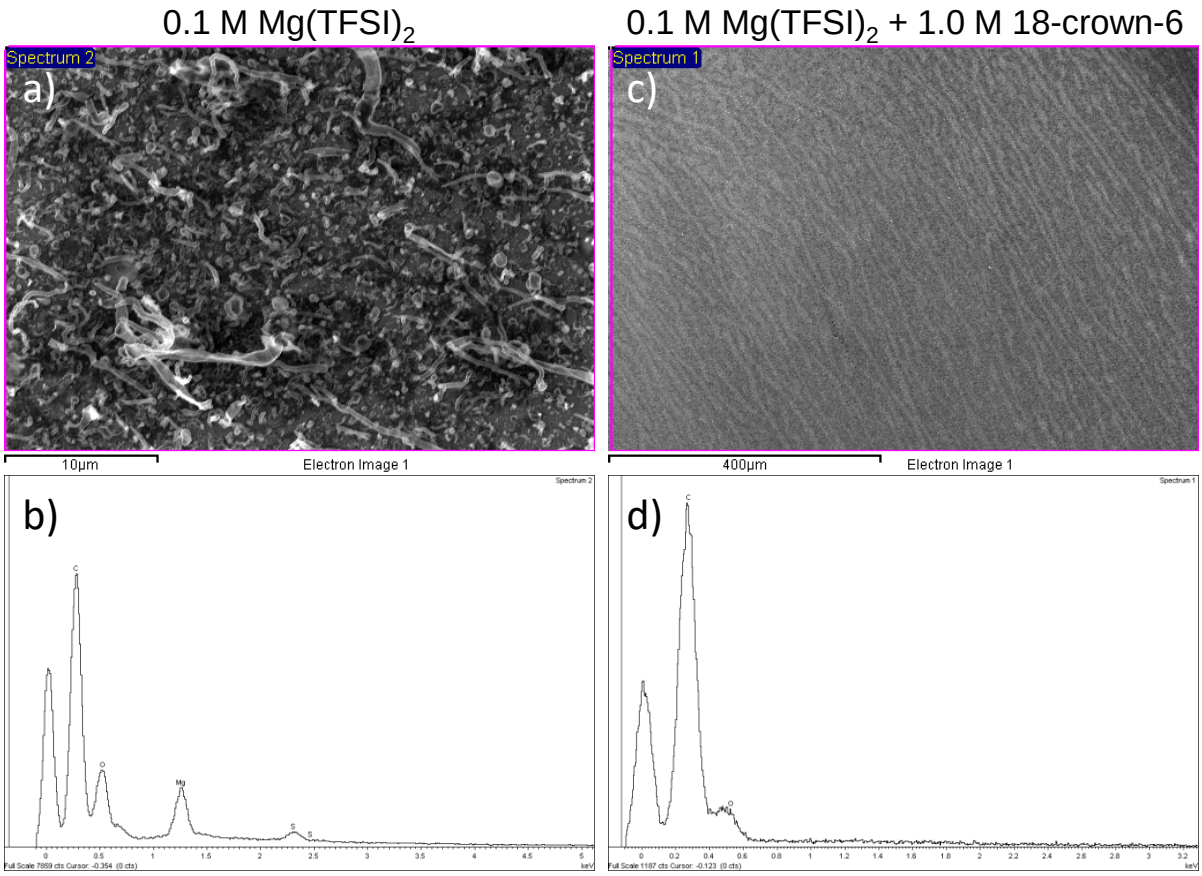
real batteries, the potential scan rate is much faster in the present measurements. Under realistic operation conditions, charging and discharging times would be longer than in the present experiments, resulting in much more extended accumulation of ORR products and electrolyte decomposition products before these are re-oxidized. This will be the subject of future studies.

3.4.4 Summary

The effect of adding crown ether as a typical complexing additive and borane dimethylamine complex (NBH) as an electrolyte drying additive to magnesium-containing *N*-butyl-*N*-methylpyrrolidinium bis(trifluoromethanesulfonyl)imide (BMP-TFSI) electrolytes was investigated to gain a better understanding of the influence of additives on the oxygen oxidation reaction (ORR)/oxygen evolution reaction (OER) in Mg-air batteries. The addition of a high stoichiometric excess of 18-crown-6 resulted in an increasingly effective masking of the Mg ions by complexation, which lowered the tendency for electrode passivation through the formation of nonoxidizable and passivating Mg (per-)oxides, to the extent observed in Mg-free BMP-TFSI electrolyte if 1.0 M 18-crown-6 ether is added to 0.1 M $Mg(TFSI)_2$. On the other hand, the complexation of Mg ions resulted in reduced formation/stabilization of re-oxidizable ORR products close to the electrode, which diminished the OER current/charge as the ORR products were rinsed away by the constant electrolyte flow. Under the present conditions, in a flow cell system, such an interphase layer is needed for a reversible ORR/OER even though it might result in some degree of passivation. Under the present reaction conditions and for the electrolytes investigated in this study, the best balance between passivation and reversibility was obtained for the 0.2 M crown-ether-containing electrolyte with a Mg/crown ether ratio of 1:2.

The addition of NBH also resulted in a slower passivation and a better reversibility when it was added at a concentration of 0.1 M. This was most probably not only caused by its water-removing properties, but also by complexation of Mg^{2+}, similar to the role of the crown ether additive. Accordingly, if the concentration of NBH is too high, the reversibility of the ORR/OER is reduced. Overall, this work revealed a complex role of different additives, which should be considered in further efforts to improve the ORR/OER performance of Mg-air batteries.

3.4.5 Supporting Information



Element	C	O	Mg	S
Spectrum 2 in at%	74.79	22.43	2.37	0.41

Element	C	O	Mg	S
Spectrum 1 in at%	88.34	11.49	0.09	0.07

Figure 42: SEM images (a, c) and EDX measurements (b, d) of the electrode surface recorded after 10 ORR cycles (-1.4 – 1.4 V) in (a,b) 0.1 M Mg/TFSI)$_2$ and in (c,d) 0.1 M Mg(TFSI)$_2$ and 1.0 M 18-crown-6 in BMP-TFSI.

3.5 Ionic Liquid Electrolytes for Metal-Air Batteries: Interactions between O_2, Zn^{2+} and H_2O Impurities

The content of this chapter was published in reference [183] and is reprinted with permission by Journal of The Electrochemical Society / Electrochemical Society (J. Electrochem. Soc. 2020, 167, 7, 070505 / 10.1149/2.0052007JES). The experimental section was removed and the information was added to the experimental part in chapter 2 of this work. The style and numbering of the references and the figures have been adapted to fit the layout of the thesis. All experiments in this work were planned by me. DEMS measurements were performed by Kaidi Zhang under my supervision. The evaluations of the DEMS data as well as the preparation of the figures were performed by me. The XRD measurements were performed by Xin Chen and the XRD-data evaluation was performed by me. Furthermore, I was strongly involved in the creative process of the publication. This work was financially supported by the Deutsche Forschungsgemeinschaft via project Be 1201/22-1 and the German Federal Ministry of Education and Research (BMBF) in the project 03X4636C ("Li-EcoSafe – Entwicklung kostengünstiger und sicherer Lithium-Ionen-Batterien"). This work contributes to the research performed at CELEST (Center for Electrochemical Energy Storage Ulm-Karlsruhe).

3.5.1 Abstract

Motivated by the potential of ionic liquids (ILs) to replace traditional aqueous electrolytes in Zn-air batteries, we investigated the effects arising from mutual interactions between O_2 and $Zn(TFSI)_2$ as well as the influence of H_2O impurities in the oxygen reduction / oxygen evolution reaction (ORR/OER) and in Zn deposition / dissolution on a glassy carbon (GC) electrode in the ionic liquid N-butyl-N-methylpyrrolidinium bis(trifluoromethanesulfonyl)-imide (BMP-TFSI) by differential electrochemical mass spectrometry. This allowed us to determine the number of electrons transferred per reduced / evolved O_2 molecule. In O_2 saturated neat BMP-TFSI the ORR and OER were found to be reversible, in Zn^{2+} containing IL Zn deposition/stripping proceeds reversibly as well. Simultaneous addition of O_2 and Zn^{2+} suppresses Zn metal deposition, instead ZnO_2 is formed in the ORR, which is reversible only after excursions to very negative potentials (-1.4 V). The addition of water leads to an enhancement of all processes described above, which is at least partly explained by a higher mobility of O_2 and Zn^{2+} in the water containing electrolytes. Consequences for the operation of Zn-air batteries in these electrolytes are discussed.

3.5.2 Introduction

The major advantage of primary Zn-air batteries is their high energy density, which is about five times higher than the one of Li-ion batteries.[20,167,168] Therefore, primary Zn-air batteries are already commercially used in applications where their low power output capability (< 10 mW) caused by the inefficiency of the air catalysts, is no significant drawback, e.g., in hearing aids.[167] This is different, however, for secondary Zn air batteries, which suffer from several drawbacks such as dendrite growth, limited solubility of the discharge product and insufficient performances of the bifunctional air electrodes.[195,196] These problems have so far precluded their technical realization. Therefore, the reversibility of the oxygen reduction reaction (ORR) and of the oxygen evolution reaction (OER) during discharge and charge of the battery is a key issue for improving Zn-air batteries.[167,169-173] The cathode side of Zn-air batteries usually consists of a porous carbon electrode covered by a catalyst layer to facilitate the ORR.[168,170] The porous electrode enables O_2 diffusion to the three-phase boundary region.[168] This, however, also allows CO_2 diffusion into and H_2O evaporation out of the cell, which are additional drawbacks since the CO_2 in the cell will react with the OH^- ions of the alkaline electrolyte and form carbonates, which reduces the lifetime of the cell.[197] Additionally, H_2O evaporation leads to drying-out of the cell.[198,199] Considering these drawbacks, ILs seem to be promising candidates for electrolytes in secondary metal-air batteries, as most of them show a very low volatility and a wide electrochemical stability window as compared to aqueous electrolytes.[16,170,200,201] The lower volatility could solve the problem of cell dry-out. Due to the wide electrochemical window H_2 evolution could be avoided, and furthermore there are ILs available which are insensitive against water and CO_2. Finally, the absence of OH^- ions precludes carbonate formation. However, the low conductivity and high viscosity are still drawbacks for the use of ILs in (metal-air) batteries. On the other hand, due to the open cell design of metal-air batteries, moisture from the air can diffuse into the cell and change the electrochemical behaviour of the electrolyte, which in the case of ionic liquids can result in an reduced viscosity and higher conductivity of the electrolyte.[202] Accordingly, the influence of water on the electrochemical properties of Zn air batteries and on the performance of the ORR/OER and the Zn plating/stripping processes, as the main processes in these batteries, in IL electrolyte is of considerable interest. These aspects are topic of the present paper, focusing on N-butyl-N-methylpyrrolidinium bis(trifluoromethanesulfonyl)imide (BMP-TFSI) based electrolytes.

There are already a number of studies on the influence of water on the Zn deposition and dissolution behaviour in various ILs, focusing mostly on the effect of water on the morphology of the resulting deposits, but also dealing with the reaction rate and the reversibility of the Zn redox couple.[200,202-205] More specifically, for BMP-TFSI Xu et al. concluded that on Pt electrodes the redox reversibility of the Zn/Zn(II) redox couple is improved and the reaction rate is increased upon addition of water.[202] At (too) high water levels this leads to a decrease of the electrochemical stability window.[202]

Furthermore, it is well known that water has an impact also on the ORR and OER in ionic liquids. For the ORR this generally results in an earlier onset of the reaction and higher currents in the presence of water.[49,206-208] For the OER the results reported so far are less clear. AlNashef et al. did not find an oxidation peak in the anodic scan after the ORR in the O_2-containing ILs 1-n-butyl-3-methylimidazolium hexafluorophosphate and 1,2-dimethyl-3-n-butylimidazolium hexafluorophosphate on a glassy carbon (GC) electrode after the addition of 3 wt% water. This they explained by a (chemical) disproportionation of the superoxide, forming O_2 ($2\ O_2^{\bullet-} + H_2O \rightarrow O_2 + HOO^- + HO^-$).[206] In contrast to this, Katayama et al. observed an anodic peak in cyclic voltammograms (CVs) in O_2-saturated, humidified (0.5 vol% of water) EMIM-TFSI after the reduction reaction and attributed this to the re-oxidation of either HO_2 or H_2O_2.[49] This anodic peak occurred at higher potentials compared to dry conditions, indicating that the addition of water hinders the OER.[49] Xiong et al. also found the OER to be hampered, but not fully inhibited in humid atmosphere (relative humidity 8 %, 25 % and 36 %) in phosphonium cation based ILs.[207] Furthermore, also the presence of metal cations is known to influence the ORR/OER in ILs and aprotic organic electrolytes.[22,51,209,210] For instance, it has been demonstrated by XRD measurements that in the presence of Zn^{2+} the ORR results in the deposition of ZnO films, which are likely to hinder the ongoing ORR / OER.[211-213]

Here we report results of a study on Zn deposition/dissolution on glassy carbon (GC) electrodes in dry and humidified BMP-TFSI, where we tried to disentangle Zn deposition and electrolyte decomposition, by using a differential electrochemical mass spectrometry (DEMS) setup, which would allow us to detect, e.g., H_2 evolution caused by the degradation of the electrolyte. These results, which are presented in the first results section, can serve also as reference for the subsequent ORR/OER measurements in the presence of Zn^{2+}. Furthermore, we used DEMS measurements to identify and quantify the consumption/evolution of O_2 in the ORR and OER, respectively, in parallel with the electrochemical measurement. This allows us

to determine the numbers of transferred electrons during the ORR from the ratio between the reduction current and the O_2 consumption, which allows the identification of the main species formed in the reactions, i.e., superoxide (O_2^-), peroxide (O_2^{2-}) or oxide (O^{2-}), if no other reactions take place in parallel (i.e. H_2 evolution; metal deposition), providing insight into the reaction mechanisms. Furthermore, the detection of O_2 during the anodic scan provides direct proof that anodic peaks are related to the OER and do not result from side reactions such as electrolyte decomposition or electrode modification. These results are presented and discussed in the second results section. Third, we studied the effect of Zn^{2+} addition on the ORR/OER by DEMS, which provides additional information on the number of transferred electrons during the cathodic scan, and on the reversibility with respect to O_2 evolution in the anodic scan. These results are presented and discussed in the third result section. Next, in the fourth section we present results on the combined effect of water impurities and Zn^{2+} on the ORR/OER in an O_2 saturated ternary electrolyte mixture containing BMP-TFSI, $ZnTFSI_2$ and H_2O. Finally the results are summarized and discussed in a comprehensive picture.

3.5.3 Results

Influence of H_2O on Zn deposition

First, we investigated the influence of H_2O on the Zn deposition by DEMS. Figure 43a shows the first two CVs recorded in 0.01 M $Zn(TFSI)_2$ containing BMP-TFSI in dried and humidified electrolyte, using a GC electrode. The CV in dry electrolyte exhibits the typical features for Zn deposition and dissolution in ionic liquid electrolytes, which are characterized by a cathodic peak due to the reduction of Zn^{2+} to Zn^0 and an oxidation peak in the anodic scan, together with a lower potential for the initial Zn^{2+} deposition.[204,213-215] This leads to an overcrossing of the current in the anodic scan with that in the cathodic one at the potential where Zn^{2+} deposition changes to Zn dissolution. Such behaviour, in particular the pronounced initial potential shift, was observed before during electrochemical deposition and it was attributed to initial nucleation processes.[204,213-215] Our CVs differ, however, from those in previous reports by the absence of a distinct cathodic peak (Zn deposition) before approaching the mass transport limited current. The absence of this peak can easily be explained by the enforced mass transport in our case.

In the second (and following) cycle(s) the reduction in the cathodic scan starts at higher potentials than in the first one. The more facile Zn deposition may be induced by residual Zn

nuclei on the surface, which promote Zn nucleation/growth in the following cycles and decrease the activation energy for further Zn nucleation.[215]

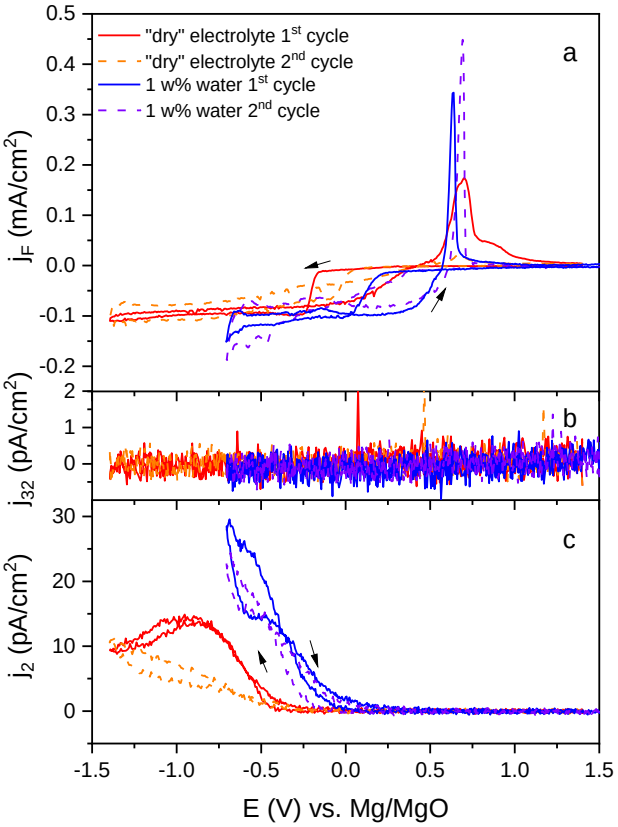


Figure 43: (a) CVs of N_2 purged "dry" (red, orange) and humidified (blue, purple) $Zn(TFSI)_2$ containing BMP-TFSI (10 mV s^{-1} 0.16 mL min^{-1}) on a GC electrode and the corresponding ion currents of (b) O_2 (m/z = 32) and (c) H_2 (m/z = 2).

The addition of water mainly causes a shift in the onset potential by 0.3 V to more positive values in the cathodic scan. This is accompanied by a sharper Zn dissolution peak in the anodic scan, whose onset occurs at slightly more negative potentials. The shift to higher potentials for Zn deposition might be attributed to changes in the nucleation behaviour during Zn deposition. These and in particular the sharper Zn dissolution peak are likely related to changes in the physicochemical properties of the electrolyte, with the addition of water leading to a decreased viscosity and increased mobility of the Zn^{2+} species. Similar observations and interpretations were reported for the effect of water on the Zn redox behaviour in different ILs,[15,203] including also BMP-TFSI.[202] The higher Zn^{2+} mobility additionally leads to a measurable increase of the mass transport limited current in the cathodic scan, resulting in a higher amount of deposited Zn during the scan.

Alternatively, the higher currents may also be attributed to H_2 evolution. The DEMS measurements resolve a clear peak at m/z = 2 (Figure 43c), indicative of H_2 evolution. This is assigned to the electrochemical degradation of H_2O from residual water traces in electrolyte

($2\ H_2O + 2e^- \rightarrow 2\ OH^- + H_2$). Both, in dry and in humidified electrolyte, the H_2 signal still increases when the Faradaic current has already reached the mass transport limited region. Thus, the H_2 evolution reaction (HER) appears to be only a minor contribution to the overall Faradaic current. As expected, the onset of the HER is at more positive potentials in the humidified electrolyte and higher HER rates are achieved.

Possible H_2 evolution from Zn corrosion in the presence of deposited Zn ($Zn + 2H_2O \rightarrow Zn(OH)_2 + H_2$)[20,168,216-218] cannot be fully excluded, but can only occur at negligible rates considering the absence of measureable m/z = 2 ion currents in the anodic scan at potentials where the Zn deposition is still in the mass transport limited region.

Finally we would like to note that the O_2 ion current (m/z = 32, Figure 43b) remains constant during cycling, indicating that there is no measurable reduction of residual O_2 in the electrolyte.

Influence of H_2O on ORR and OER

The influence of H_2O on the electrochemical stability of BMP-TFSI is widely discussed and it is known, that an increasing H_2O content leads to a smaller electrochemical window (EW).[34,163,202,219] Additionally, the presence of water was reported to have a promoting influence also on the ORR in ILs.[24,185,206,208,219] In order to model the H_2O content of a system open to air, we introduced water to the system by purging the electrolyte with O_2 which was saturated with H_2O at 23°C.

In Figure 44 we compare the CVs and the ion currents of O_2 (m/z = 32) and H_2 (m/z = 2) during the ORR/OER in BMP-TFSI on a GC electrode in the presence (purple) and absence (black) of added water. Note that in contrast to the measurements in Zn^{2+} containing electrolyte shown in the first section we found no significant difference between the first and following cycles, indicating that the electrode surface is not modified by deposition of reaction products in the Zn^{2+} free electrolyte. Therefore, only the first cycle is depicted in Figure 44.

It has been reported previously that in dry pure BMP-TFSI the first reduction step in the ORR on GC electrodes[186,187] and Au electrodes[49] is a one-electron transfer, forming a superoxide ion ($O_2 + e^- \rightleftharpoons O_2^{-\bullet}$), which is followed by a second one-electron reduction step, forming a peroxide ion ($O_2^{-\bullet} + e^- \rightarrow O_2^{2-}$) on GC[51,188] and Au[49].

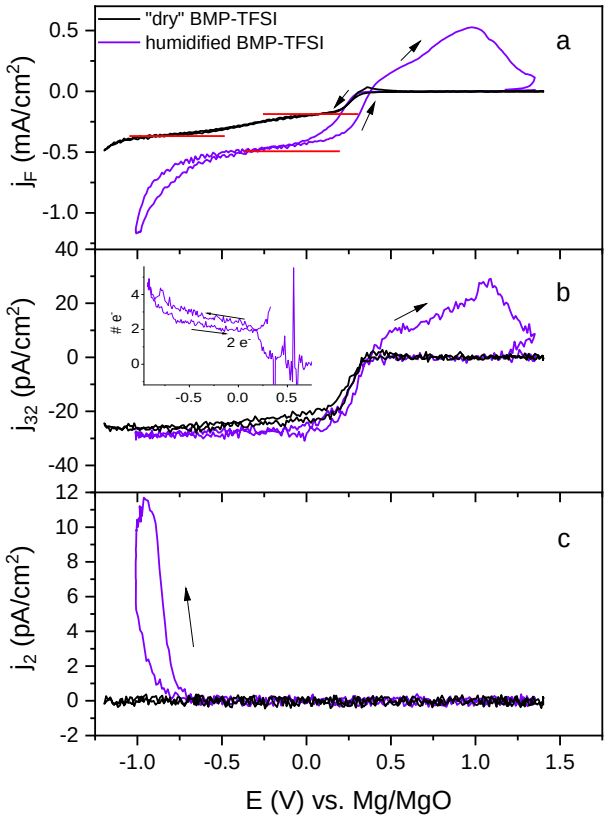


Figure 44: (a) CVs of ORR/OER in "dry" and H_2O containing BMP-TFSI and the corresponding ion currents of (b) O_2 (m/z = 32) and (c) H_2 (m/z = 2) (10 mV s^{-1}; 0.16 mL min^{-1}). Inset: number of transferred electrons in humidified electrolyte.

The Faradaic currents of the "dry" BMP-TFSI measurements show both one-electron and two-electron reduction of O_2, depending on the potential, similar to previous measurements with the same system performed in our group at a slower scan rate.[51] This allows us to calculate the intrinsic k* value ($k^* = nI_{MS}/I_F$) of the DEMS-setup. Using the reduction in the current plateau at around 0 V as reference for a one-electron transfer, the second current regime (around -0.5 V) corresponds to a two-electron transfer. This points to predominant peroxide formation at low potentials. Interestingly, the potential difference between the two reduction ranges was reported to be around 1 V for a Au electrode,[49] while for reduction on the GC electrode the potential difference between the plateaus (black curve, "dry" IL) is only 0.5 V. This may be related to the different electrode materials. We cannot rule out, however, that this discrepancy is influenced by water traces in our "dry" electrolyte. For instance, RRDE measurements by Yuan et al. showed that the addition of 0.25 wt% water leads to a shift of the two-electron reduction to more positive potentials by at least 0.2 V.[185] Moving to the humidified electrolyte, the two-electron transfer should be even more promoted, shifting its onset to more anodic potentials. Experimentally (see purple graphs in Figure 44), we

observe the onset of the ORR in the humidified electrolyte at about the same potential as in "dry" electrolyte. However, only a single reduction range is visible, where about two electrons (2.3 e^-, see inset) are transferred per O_2 molecule during the reduction. Due to the presence of only a single reduction range, there is no internal reference with a single-electron transfer for determining the number of transferred electrons like in the "dry" electrolyte measurement. Therefore, we used the k* value of the measurement in "dry" electrolyte for the evaluation (which may be slightly off due to different transport properties of O_2 in the humidified electrolyte). This results in values of the transferred electrons of about 2.3, which are rounded to 2 for further discussions. A two-electron transfer was calculated also by Yuan et al. from RRDE measurements on a Pt electrode in humidified BMP-TFSI.[220] From that number the authors concluded that after the addition of a significant amount of water (about 1 wt%) peroxide is formed upon reduction ($O_2 + H_2O + e^- \rightleftharpoons HO_2^\bullet + OH^-$; $2HO_2^\bullet \rightarrow O_2 + H_2O_2$).[185] Switzer et al. arrived at similar conclusions for the ORR in imidazolium-based trifluoromethanesulfonate electrolyte on Pt and GC electrodes, that the presence of an H^+ donor shifts the reaction to a two-electron ore even four-electron process, depending on the electrode material.[24] They observed that after the addition of different protic additives, e.g., triflic acid or acetophenone, the ORR proceeds along a two-electron pathway on the GC electrode, and along a four-electron pathway on the Pt electrode. The effect of the proton donors increases with increasing acidity / decreasing pK_a.[24] Nonetheless, we cannot completely exclude a contribution (< 15 %) from a four-electron pathway process on our GC electrode. Additionally, the Faradaic current in the mass transport limited region of our measurement was found to increase upon the addition of water, without changing any other parameter. This increase, which is in line with the observations by Yuan et al. and Katayama et al. in water containing BMP-TFSI, can be explained by a lower viscosity, resulting in a higher mobility of O_2 upon the addition of a protic solvent.[49,185,219] Also, the electrochemical window of the electrolyte is narrowed upon the addition of water to the electrolyte, as indicated by the increase of the cathodic current at potentials below ~ -0.6 V. This increase is due to the evolution of H_2, as shown by the corresponding signal in the ion current for m/z = 2. Thus, this current is due to water splitting rather than due to the decomposition of the IL. Nevertheless, we cannot rule out that part of the resulting current could also be due to the decomposition of BMP-TFSI, since it has been shown that water decreases its stability window.[34,163,202,219] Furthermore, H_2 (m/z = 2) has been found as fragment of BMP-TFSI decomposition.[110]

In the anodic scan in "dry" BMP-TFSI, a small peak appears in the Faradaic current and also in the O_2 signal. This peak is attributed to the OER, oxidizing dissolved $O_2^{-\bullet}$.[51,188] Although, the signals in the Faradaic current (0.5 % of the ORR current) and the ion current for m/z = 32 are small, the charge ratio between the two confirms a one-electron transfer during the OER. The main reason for the small signals is that the soluble superoxide and peroxide products formed in the cathodic scan are flushed away in the flowing electrolyte.

In humidified electrolyte the OER peak is much more pronounced. This result differs from part of the previous reports on the absence / appearance of an OER peak in humidified IL:[16,23,49,185,206,219,221] AlNashef et al. did not find an OER peak after the addition of 3 wt% water in an imidazolium based ILs with a hexafluorophosphate anion on a glassy carbon electrode, which they explained by a water-induced destabilization of the superoxide, resulting in an irreversible formation of peroxide ($2\ O_2^{-\bullet} + H_2O \rightarrow O_2 + HOO^- + HO^-$).[206] This is in line with the interpretation and a CV reported in two papers by Yuan et al. for 1 % water containing BMP-TFSI in O_2 atmosphere.[185,219] Unfortunately, in the second paper, these authors show another CV for the same electrolyte, but with a more negative (not specified) lower potential limit, which features two peaks in the anodic scan, where one of them appears at the expected OER potential.[219] Despite these inconsistencies, there is at least a rather constant anodic Faradaic current in the anodic scan, which might be attributed to the OER (also from peroxide species). In contrast to the results by Yuan et al., increased peaks for the OER in humidified (compared to "dry") ILs were reported by Katayama et al. (imidazolium based TFSI IL and a Au electrode)[49] and Islam et al. (imidazolium based BF_4 IL and a Hg electrode)[208], which is in line with our results for humidified BMP-TFSI on a GC electrode (see Figure 44a).

A very similar peak we found also for the m/z 32 ion current (Figure 44b), which proves that it originates from the OER. The amount of O_2 evolved as measured by DEMS (integration between 0.3 and 1.4 V) points to the transfer of in average 1.5 electrons per O_2 molecule, which is explained by the oxidation of a mixture of superoxide and peroxide. This implies that not only superoxide, but also the peroxide formed during the ORR can be re-oxidized in BMP-TFSI.

The much more pronounced OER peak in humidified IL found in our flow cell experiments is surprising because dissolved intermediates (either superoxide or peroxide) should largely be flushed away as observed in the "dry" electrolyte. Thus, we conclude that the peroxide

species formed in H_2O containing electrolyte largely remain at the working electrode and can there be oxidized again.

ORR and OER in Zn^{2+} containing BMP-TFSI

As shown in the previous sections, the ORR in BMP-TFSI on GC takes place in the same potential window as Zn deposition (which for a Zn-air cell would result in a very low or no usable cell voltage). Thus, both processes could contribute to the cathodic Faradaic current when the electrolyte contains both Zn^{2+} and O_2. Furthermore, also the influence of the Zn^{2+} ions on the ORR product formation (and their possible deposition on the electrode surface) and on the OER are key issues for Zn-air batteries. In Figure 45 we present CVs of 0.01 M $Zn(TFSI)_2$ in O_2-saturated BMP-TFSI.

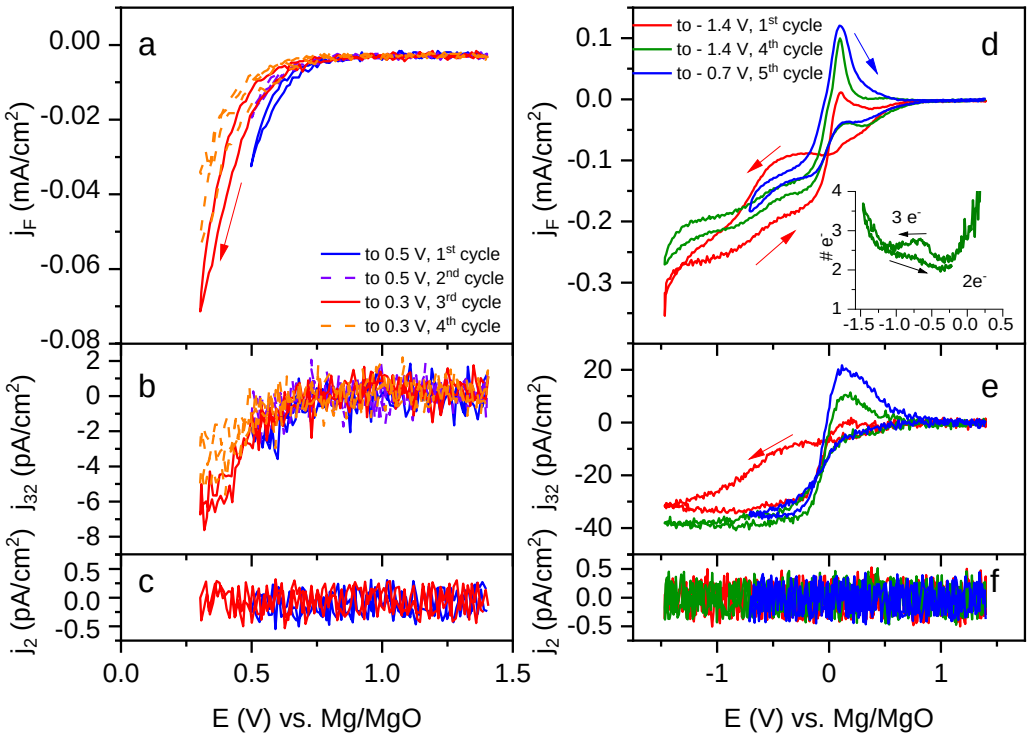


Figure 45: CVs of O_2 saturated 0.01 M $Zn(TFSI)_2$ in BMP-TFSI (10 mV s^{-1} 0.16 mL min^{-1}) on a GC electrode (top) and the corresponding ion currents of O_2 (m/z = 32) and H_2 (m/z = 2) with increasing (left) and decreasing (right) potential window. Inset: number of transferred electrons during the 4th cycle.

On the left hand side (Figure 45 a-c), we show current traces recorded during cycling, in which the lower potential limit was shifted to more negative values by 0.2 V after the first two cycles. To determine the onset of the ORR and to distinguish it from Zn deposition, we use the ion current of m/z = 32 (lower panel). The onset of the Faradaic current in Figure 45 is shifted to more positive potentials as compared to the ORR in neat BMP-TFSI (Figure 44). As indicated by the simultaneous onset of O_2 consumption (Figure 45b), the Faradaic current

results from the ORR. A similar shift of the ORR onset potential was already observed previously upon the addition of Mg^{2+} addition on a GC electrode.[51,63,64] The lower currents in the second cycle of each potential window indicate that there is some electrode passivation. During the ORR, two electrons per O_2 molecule are transferred, which points to the formation of O_2^{2-} and, in the presence of Zn^{2+}, to the formation of deposited ZnO_2. This resembles our previous DEMS results in 0.1 M $Mg(TFSI)_2$ containing BMP-TFSI, where we detected the formation of MgO_2, which passivates the surface.[51] DEMS measurements on other divalent cations (Mg^{2+}, Ca^{2+}, Sr^{2+}, Ba^{2+}) in DMSO based perchlorate electrolytes have shown that these also favour a two-electrons transfer per O_2 molecule on Au electrodes. In contrast, on GC electrodes this is only the case for Mg^{2+} and Ba^{2+}, while Ca^{2+} and Sr^{2+} were found to favour the transfer of 1 to 1.5 electrons.[209]

In the anodic scan, there is no peak in the Faradaic current, in contrast to the observations in neat BMP-TFSI. This is in line with the results of Azaceta et al. and Tulodziecki et al., who reported that the ORR is irreversible in Zn^{2+} containing BMP-TFSI[212] and EMIM-TFSI.[213] Obviously, the re-oxidation of ZnO_2 is unlikely. Again, this resembles our findings in Mg^{2+} containing BMP-TFSI, where the formation of MgO_2 is irreversible, with no features in the anodic current.[51] Cycling in the wider potential window (indicated by the blue curves), the passivation observed in the 2nd cycle persists, but higher ORR currents are visible when going to the more negative potentials. This goes along with a higher O_2 consumption (Figure 45b). Also in this case the ORR is irreversible and the 2nd cycle to low potentials shows again lower currents due to passivation.

On the right hand side of Figure 45 (d-f), the lower potential limit is even lower and first set to -1.4 V. Starting with a freshly polished electrode, we again find an initial current increase in the first cathodic scan at potentials below 0.6 V, i.e., in the range where we later see O_2 evolution in the anodic scan, which is accompanied by O_2 consumption. At more negative potentials this is followed by two plateaus in the first cathodic scan, which also go along with O_2 consumption. This resembles our observations in neat BMP-TFSI. In the following cycles the Faradaic current is slightly lower than in the first cycle, similar to the measurements in the small potential window. This indicates that the first cycle leads to some surface passivation (most likely due to the deposition of the ORR products). The number of electrons transferred per O_2 molecule starts at a value of two between 0 and -0.5 V, in agreement with the results obtained in the narrow potential window, and reaches a value of about three transferred electrons at lower potentials (see the inset of Figure 45d for the 4th cycle). Since there is no

stable oxidic species resulting from a 3 electron transfer, we expect ZnO formation in parallel to peroxide formation at lower potentials. The formation of ZnO is in agreement with previous studies, where the films deposited on different electrode materials such as fluorine doped tin oxide,[211,212] Pt, stainless steel and indium tin oxide[213] upon reduction in $ZnTFSI_2$ containing BMP-TFSI were found to mainly consist of ZnO. This is different from the addition of Mg^{2+} (0.1 M), where MgO_2 was found as the main product of the ORR.[64] However, also side processes which do not consume O_2, such as the Zn deposition (which at least in the absence of O_2 occurs at these potentials) or electrolyte decomposition could contribute to the higher number of transferred electrons. We can rule out, however, H_2 formation, which could be expected from reduction of water traces. In an attempt to characterize the deposits formed after extensive cycling, XRD measurements were performed after rinsing the electrode surface with acetone. However, the thickness of the resulting layer seems to be insufficient for this analysis and no characteristic signals were found (see supporting information).

In the anodic scan we observe a peak appearing already in the first cycle after scanning to low potentials, which increases during cycling until it reaches a steady state in the 4^{th} cycle. This peak was not observed when cycling in the narrow potential window (Figure 45a-c). In this anodic peak, O_2 formation is detected. Assuming this as the only process, this would correspond to 1.1 ± 0.05 electrons transferred per O_2 molecule (based on the integrated charges of the Faradaic current over the entire peak and of the m/z = 32 ion current), similar to observations in Mg^{2+} containing BMP-TFSI,[51] which hints to the re-oxidation of superoxide. The finding that a potential excursion to very negative values during the ORR is needed before the OER can be observed in the succeeding anodic scan, closely resembles our previous findings in Mg^{2+} containing BMP-TFSI.[51] Interestingly, after cycling in this wide potential range, and subsequently raising the lower potential limit in the cathodic scan (blue line, Figure 45d, e), the anodic OER peak is still visible and the number of electrons is still one, again similar to corresponding experiments with Mg^{2+}.

In summary, the ZnO_2 formation during the ORR in the presence of Zn^{2+} appears to be irreversible with no observed OER in the anodic scan, when scanning to potentials around 0.3 V. In contrast, when cycling to lower potentials (here -1.4 V), the formation of O_2^- is enabled and an OER peak appears.

Influence of H_2O on the ORR / OER in Zn^{2+} containing IL

Finally we also investigated the influence of water on the ORR/OER in 0.01 M $Zn(TFSI)_2$ containing BMP-TFSI. In Figure 46 we show CVs recorded in the narrow potential windows in the left column. Cycling with a cathodic limit of 0 V (red graph), we find a reductive current at E < 0.5 V, accompanied by O_2 consumption, as detected by DEMS. Hence, the ORR starts at 0.5 V, which is similar to the behaviour in "dry" Zn^{2+} containing IL.

In this case we did not observe passivation effects in the second and third cycle, in contrast to the ORR in "dry" Zn^{2+} containing electrolyte. Possibly, water hinders either the formation or the adsorption of ZnO_2, which was held responsible for the passivation in "dry" electrolyte. Since more than two electrons per O_2 molecule (based on the integrated charges of the Faradaic current and of the m/z = 32 ion current) are transferred during the ORR, peroxide formation cannot be the only process in that reaction. Instead, ZnO formation or even Zn deposition seem to occur in parallel. Whatever product is formed in the narrow potential range during reduction, its formation appears to be irreversible, as no anodic current is found in the subsequent positive-going scan. Only after cycling to lower potentials (blue), we find a current peak in the anodic scan. However, there is no corresponding peak in the mass spectrometric measurements, neither in the O_2 nor in the H_2 signal. This is also true when scanning to even slightly more negative potentials, where the anodic Faradaic current peak is more pronounced. Obviously, the peak in the Faradaic current at 0.3 V can only stem from processes which do not evolve O_2 formation, such as Zn dissolution.

Figure 46d-f shows a CV recorded in an expanded potential window, with a lower limit of -1.2 V, using a freshly polished electrode. Since the first and the following cycles do not differ, which is in contrast to our finding for the ORR in "dry" Zn^{2+} containing BMP-TFSI, we show only the first cycle. Going to cathodic potentials, there is only a single plateau in the cathodic current, which is also in contrast to the "dry" electrolyte. At even lower potentials, we detect H_2 evolution. In the potential range of the plateau two electrons are transferred per O_2 molecule, again pointing towards peroxide formation. H_2 evolution, indicative of electrolyte decomposition (including possible water trace impurities), starts at -1 V, i.e., at 1 V lower potential compared to O_2-free electrolyte (see the first section). Obviously, the HER from water splitting is hindered in the presence of O_2.

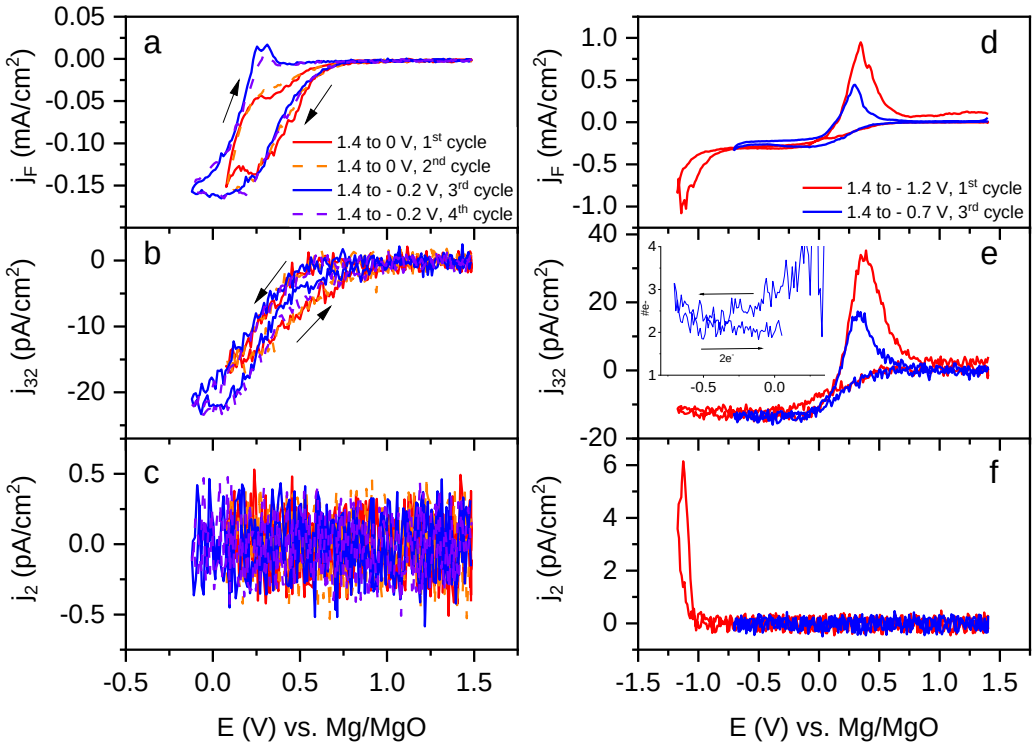


Figure 46: CVs of O_2 saturated 0.01 M $Zn(TFSI)_2$ with 1.1 wt% H_2O in BMP-TFSI (10 mV s^{-1} 0.16 mL min^{-1}) on a GC electrode (top) and the corresponding ion currents of O_2 (m/z = 32) and H_2 (m/z = 2) with increasing (left) and decreasing (right) potential window. Inset: number of transferred electrons during the 3rd cycle.

Going to anodic potentials, a current peak appears at around 0.3 V, which is paralleled also the O_2 signal. Also after narrowing the potential window, in order to cycle in a potential range where no electrolyte decomposition takes place (blue), the OER is still visible. It is again connected with a two-electron transfer per O_2 molecule, as expected for a re-oxidation of peroxide. This is different to the measurements in Zn-free electrolyte, where only one electron per O_2 molecule is transferred during the OER, as discussed in the second section.

Additionally, after the cycling experiments (start/end of the cycle at 1.4 V vs. Mg/MgO), we again performed XRD measurements in order to identify irreversibly deposited products on the GC electrode. In contrast to the "dry" electrolytes, the results shown and discussed in the supporting information indicate mainly the formation of zinc-oxide species. Additional formation of ZnO_2 cannot be excluded, however. Nevertheless, assuming that the formation of ZnO_2 is reversible, only a small amount of this is expected to remain on the electrode surface as the CV experiment was stopped at the upper potential limit, where ZnO_2 should largely be consumed in the OER.

3.5.4 Discussion

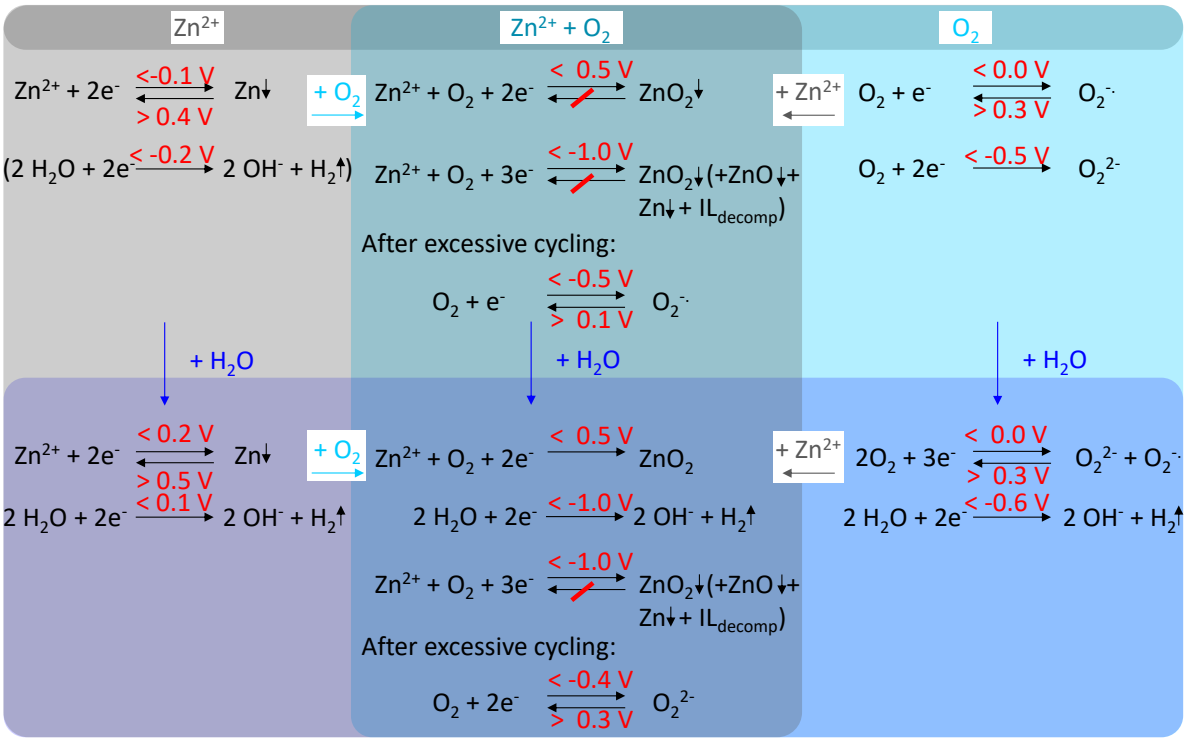


Figure 47: Schematic overview of the ongoing reactions during cycling in different electrolyte sytems.

In Figure 47 we present an overview about the various reactions taking place in the different BMP-TFSI based electrolyte mixtures, which were discussed separately in the preceding sections. The red numbers above the arrows indicate the onset potentials of the different reactions in the direction of the respective arrows. The different reactions can be summarized as follows:

1. In O_2-free electrolytes, the presence of Zn^{2+} in the IL electrolyte leads to a reversible Zn deposition / dissolution. On a clean GC surface Zn deposition (-0.1 V) is shifted to lower potentials to initiate Zn nucleation,[215] whereas in later cycles Zn deposition can be observed already at potentials < 0.1 V, equivalent to an shift of 0.2 V to more positive potentials. Although for Zn-air batteries a substantial potential difference between Zn deposition and ORR is desired, in the IL electrolyte studied here, the onset of the ORR in Zn^{2+}-free BMP-TFSI is only at ~0 V, i.e., in a similar potential range as Zn deposition. The ORR first proceeds reversibly via formation of a superoxide, whereas peroxide formation is observed at more negative potentials (-0.5 V).
2. In the "dry" electrolyte containing both Zn^{2+} and O_2, metallic Zn deposition plays only a minor role, and the ORR is the dominating process. In this electrolyte, the ORR proceeds via a transfer of two (at low potentials three) electrons per O_2 molecule, which results in

the deposition of ZnO_2 films. At low potentials, additional processes occur, such as ZnO formation, metallic Zn deposition and electrolyte decomposition, which lead to an overall increase of the number of electrons exchanged per O_2 molecule. Under these conditions, the OER is observed only after a preceding potential excursion to very low potentials, below -1.4 V, while at higher turnaround potentials the surface appears to be passivated with no OER in the anodic scan. The OER detected after cycling to very low potentials, delivers one electron per molecule O_2 formation. This is interpreted in a picture where after cycling superoxide species are formed in the cathodic scan (possibly due to a local depletion of Zn^{2+}) which are reversibly oxidized in the anodic scan producing O_2. Similar findings have been reported also for the ORR/OER upon the addition of Mg^{2+} (0.1 M) in the same IL.[51]

3. The addition of H_2O has a positive effect on the Zn deposition (in O_2-free electrolyte) and on the ORR and OER (independent of the Zn^{2+} addition).
   a. In Zn^{2+} containing O_2-free electrolyte, the Zn deposition occurs at higher potentials compared to "dry" electrolyte. Both, in humidified and "dry" electrolyte, the onset of Zn deposition in the first cathodic scan requires at least 0.3 V more negative potentials than the ongoing Zn deposition in the subsequent anodic scan. Thus the nucleation of Zn is a key issue for Zn deposition in both electrolytes. The positive potential shift in humidified electrolyte may be attributed to changes in the Zn^{2+} coordination changing from $TFSI^-$ coordinated ions to aqueous Zn^{2+} species. This has been found by Raman spectroscopy in trifluoromethanesulfonate based ILs.[204] Furthermore, the Zn dissolution peak is sharper upon water addition, which is likely related to changes in the physicochemical properties of the electrolyte, i.e., a decreased viscosity and increased mobility of the Zn^{2+} species.[15,203]
   b. The higher mobility of the electrolyte species by the addition of a protic solvent[49,185,219] also causes an increase of the faradaic currents of ORR and OER in Zn^{2+}-free BMP-TFSI.
   c. Upon the addition of water to the Zn^{2+}-free electrolyte, the number of electrons transferred per O_2 molecule changes and mostly peroxides are formed. Additionally, the amount of evolved O_2 is largely enhanced after humidifying the electrolyte, which indicates that the peroxide species remain at the working electrode and are therefore oxidized again.
   d. In Zn^{2+} and O_2 containing electrolyte, the onset potential for ORR is at similar potentials as in "dry", neat BMP-TFSI. After cycling to low potentials OER takes place

in both humidified, O_2 containing electrolytes. The transfer of two electrons per O_2 points to the reversible formation / oxidation of H_2O_2 in the ORR / OER on the GC electrode. While no significant enhancement of the ORR / OER has been found in dry BMP-TFSI[64] when using GC or catalysts which are known to be more active in aqueous electrolytes (Pt, manganese oxides), the influence of such more active catalysts has not been studied systematically in mixed water/ILs.

Finally we would like to note that it is well known that GC is not a good catalyst for the ORR in aqueous electrolytes, since the activity is low and mostly H_2O_2 is formed instead of water.[222] Therefore, better catalysts such as Pt or metal oxides[58,223,224] or even nanofiber materials,[225-227] are needed and used for Zn-air batteries. In non-aqueous electrolytes, the role of the electrocatalyst on the reaction mechanism is less understood. Comparing GC, Au,[63] Pt and manganese oxide catalysts,[64] no significant enhancement of the ORR / OER has been found in dry BMP-TFSI with and without the addition of Mg^{2+}. This observation may be explained by very weak interactions between the electrode surface and the superoxide anion, resulting in an outer sphere reaction mechanism.[63] Similarly, Reinsberg et al. found for another non-aqueous Mg^{2+} containing electrolyte (0.4 M $Mg(ClO_4)_2$ in DMSO) that around two electrons are transferred per O_2 molecule for GC, Au and Pt electrodes, while between 3 and 4 electrons are transferred when using Rh electrodes.[65] Since the humidified BMP-TFSI electrolytes are in between the aqueous and non-aqueous electrolytes, the influence of the electrode material would be an interesting topic for further studies.

Considering the studied mixtures as electrolytes for Zn-air batteries both, the ORR / OER and the Zn deposition / dissolution appear too sluggish for practical applications. The addition of water enhances the electrolyte properties and the reactions kinetics are improved, however, the reaction kinetics are still inferior to common aqueous electrolytes employed in Zn-air batteries. Therefore, the implicit advantages of ionic liquid electrolytes (e.g. no carbonate formation, less H_2 evolution) cannot counterbalance the drawbacks.

3.5.5 Conclusions

Aiming at a better understanding of the processes in secondary Zn-air batteries we have investigated the influence of water trace impurities and Zn^{2+} ions on the ORR/OER in humidified and dry BMP-TFSI on a GC electrode by online DEMS. The measurements were performed under enforced and controlled mass transport conditions. The addition of water was shown to lead to reversible peroxide formation, which is not suppressed by the addition

of Zn^{2+}. This shows that the addition of water can improve the performance of air batteries with ionic liquid electrolyte. Although the presence of water improves the Zn deposition / dissolution and ORR / OER characteristics of the IL electrolyte, the kinetics of the ORR are still slow compared to aqueous electrolytes. Here the electrode material i.e., the electrocatalyst, could play a crucial role in the humidified IL electrolytes. Overall, the measurements have demonstrated the additional insights that can be gained from online spectro-electrochemical studies under well-defined reaction and transport conditions.

3.5.6 Supporting Information

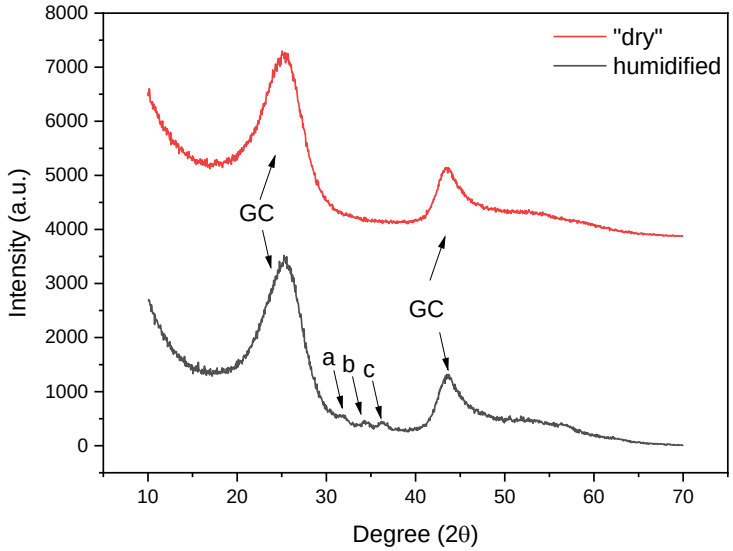


Figure 48: X-ray diffractograms of the products deposited during cyclic voltammetry on a glassy carbon electrode in 0.01 M Zn(TFSI)2 in BMP-TFSI under "dry" and humidified conditions.

After the cycling experiments (several cycles from 1.4 to -1.4 V) the electrode was washed with acetone and dried under a N_2-flow. In the X-ray diffraction patterns shown in Figure 48 under "dry" conditions only two peaks are visible, which can both be attributed to the glassy carbon substrate.[228] Thus, no sufficient amount of ZnO_x has been formed for the XRD analysis.

In humidified conditions three additional peaks appear at around 32° (a), 35° (b) and 37° (c). These peaks can be attributed to the deposition of either ZnO (a, b, c) or ZnO_2 (a, c).[229,230] So the appearance of these three signals does not allow to discriminate between ZnO and ZnO_2. For these two materials, additional peaks are expected at 47° and 57° for ZnO and 53° for ZnO_2,[229,230] which would enable the differentiation. Unfortunately, due to the low signal to noise ratio, these peaks cannot be detected. The low amount of ZnO_2 might be caused by only reversible formation of the peroxide, which cannot be accumulated during several cycles. Therefore, the deposited amount might be under the detection level of XRD.

4 Summary

Because of the limited availability and the questionable mining of key Li-ion battery components such as lithium and cobalt, taking a completely new approach in finding efficient materials and developing innovative battery systems is inevitable. The present thesis intends to contribute to the development of such Li- and Co-free systems by investigating new electrode materials and electrolytes regarding their performance and especially their stability for the application in Li-ion and metal-air batteries. For these investigations, differential electrochemical mass spectrometry (DEMS) was proven to be a valuable method. The simultaneous combination of electrochemistry and mass spectrometry allows tracing of the electrochemical reactions in parallel to the detection of volatile reaction products and thus facilitates conclusions on the reaction mechanisms going on during the electrochemical measurements.

For the DEMS measurements, different electrochemical cells, specifically developed for each investigated system, is a key factor for the information which can be gained. Within the present thesis, three different types of electrochemical cells were used. For the investigation of volatile electrolytes, in chapter 3.1, the difference between using an electrochemical cell equipped with a membrane in comparison to a cell without membrane was shown, resulting in the finding that each cell has its advantages and disadvantages: the membrane cell allows the detection of only small amounts of small molecules, whereas the cell without membrane enables the detection of $LiPF_6$ decomposition products. The combination of the results of both cells allows therefore a deeper understanding of the electrochemical decomposition processes. For non-volatile electrolytes, which show only a negligible vapour pressure, the use of an open cell is possible without the disadvantages of a high background pressure. Therefore, this system is suitable for the investigation of the decomposition mechanism of ILs as it was performed in chapter 3.2 and 3.3. However, it is not possible to investigate electrolytes based on ILs with volatile components like O_2, NBH or crown ether in this open cell. Therefore, again, a membrane containing cell (flow-cell) was used for the investigation of the ORR and OER in ionic liquids containing at least one of the former mentioned additives (chapter 3.4 and 3.5). The flow-cell system used in this case allows an even and controlled mass transport of the O_2 to the working electrode. Overall, with the use of suitable electrochemical cells and setups, DEMS is an appropriate tool for the investigation of battery reactions in order to gain insights into the reactions taking place at battery electrodes.

For the improvement of existing batteries, one first step is the use of a cobalt-free cathode material. Therefore, in the present thesis, Li_xVO_2F was investigated in chapter 3.1. This

cobalt-free material is supposed to have a high capacity in comparison to currently used cathode materials due to the formation of superoxide and peroxide species during charging. Thus, one important issue arising in this context is the question if the material remains stable during continuous charging and discharging or if it decomposes, together with the evolution of O_2. Another question is whether the LP30 electrolyte decomposes at the Li_xVO_2F surface. The measurements showed that the O_2 evolution behaviour has to be investigated in a membrane-cell, because for detecting small amounts of O_2 the background pressure of the electrolyte components has to be low, as these also produce fragments with m/z 32. The measurements showed a peak of O_2 evolution during the first anodic scan, while no O_2 was detected at the positive potential limit or in subsequent cycles. This indicates that after initial oxidation of impurities or decomposition of electrode components, resulting in O_2 formation, the material stays stable without additional O_2 release. Electrolyte decomposition products were detected in parallel. In the cathodic scan below 1.5 V, the formation of ethylene was observed, whereas at positive potentials above 3.2 V, CO_2 formation was monitored in the membrane-cell. These processes result in an electrochemical window of 1.7 V. On the other hand, the membrane-free cell showed the formation of $LiPF_6$ decomposition products in parallel to the CO_2 formation, which was not observed in the membrane cell.

Another step for improving battery systems is the use of an electrolyte with a broad electrochemical window. Therefore, the last years evidenced an increasing interest in the investigation of ionic liquids as battery electrolytes. Besides the high electrochemical stability, many ILs also show other positive properties like a low vapour pressure and a low flammability. Among them, BMP-TFSI and EMIM-TFSI have often been subject of model-studies due to their promising properties and commercial availability.

In order to further improve the electrochemical stability of ILs, it is needed to understand the decomposition mechanism. A first step is to discriminate at which potential the anion and cation, respectively, start to decompose. For the investigations presented in chapter 3.2 a novel DEMS setup was developed, which allows us to discriminate between the products formed at the working and the counter electrode. The results showed that the cathodic stability is influenced by simultaneous decomposition of anion and cation in neat IL, where BMP^+ showed a higher stability in comparison to $EMIM^+$. The BMP^+ decomposition on the Au electrode proceeds via cleaving the bond between the ring and the butyl sidechain, resulting in the formation of methylpyrrolidine and butyl. Also a ring opening was observed, which led to the detection of dibutylmethylamine. For the anodic stability, no influence of the cation was observed.

In chapter 3.3, the studies were broadened to include the influence of the electrode material and the effect of impurities from synthesis of the IL on the decomposition mechanism. The impact of the presence of metal ions, i.e. Li^+ and Mg^{2+}, which are inevitably present as charge carriers in battery electrolytes, on the electrochemical stability was investigated, as well. Changing the electrode material from Au to GC has no strong influence on the electrochemical stability of the IL, but it has some influence on the decomposition mechanism. On the GC electrode, the $TFSI^-$ decomposition becomes the dominant process at cathodic potentials, even though the stability window remains unchanged. The use of BMP-TFSI from two different suppliers, Merck and Solvionic, also shows a strong influence on the decomposition mechanism. Even though the exact reasons for this discrepancy in the results of the decomposition measurements remained unknown, we assume that residues from the synthesis of the IL are responsible for this observation. Also the addition of Li^+ influences the electrochemical stability of the IL. The presence of Li^+ largely hinders the formation of volatile cathodic BMP-TFSI decomposition products, while Li deposition / dissolution can be monitored. Similar to Li^+ also the presence of Mg^{2+} influences the BMP-TFSI decomposition mechanism. The strong interactions of the Mg^{2+} ion with $TFSI^-$ destabilizes the $TFSI^-$ anion against the reductive decomposition, resulting in a shift of the product distribution from mostly BMP^+ fragments in neat BMP-TFSI to mostly $TFSI^-$ fragments in $Mg(TFSI)_2$ containing BMP-TFSI. Additionally, it hampers the BMP^+ decomposition. Interestingly, in this electrolyte / electrode setup we could not find indications for Mg deposition.

Nonetheless, for the use in metal-air batteries not only the metal deposition behaviour and the electrochemical stability of the electrolyte are important aspects, but also a reversible oxygen reduction reaction is a key issue. The electrochemical window necessary for the ORR/OER reaction in BMP-TFSI electrolyte appears in the stability range of the electrolyte known from chapter 3.3. Measurements in our group[51,63,64,78] revealed that in Mg^{2+} containing BMP-TFSI a passivating layer of MgO and MgO_2 is formed on the electrode surface. One idea to overcome the formation of this passivating layer is masking the Mg^{2+} ions by complexing agents such as 18-crown-6 and NBH. The results discussed in chapter 3.4 showed that overstoichiometric amounts of 18-crown-6 can mask the Mg^{2+} ions and hinder the participation of Mg^{2+} in the ORR, resembling the measurements in Mg-free BMP-TFSI. On the other hand, the addition of 18-crown-6 also seems to reduce the amount of reduced oxide species (superoxide and peroxide) close to the electrode surface, diminishing the OER current as the ORR products are rinsed away by the constant electrolyte flow. The addition of NBH instead of crown ether also resulted in a slower passivation and a better reversibility compared

to neat BMP-TFSI when added with a concentration of 0.1 M. In total these results revealed a complex role of different additives, which should be considered for future studies regarding improving the ORR/OER performance of Mg-air batteries.

In contrast to the above mentioned studies in our group[51,63,64,78] using Mg^{2+}-containing BMP-TFSI where no Mg deposition was observed, Zn deposition from Zn^{2+}-containing BMP-TFSI was monitored in chapter 3.5. For ILs, previous studies showed an improvement of the reaction kinetics for Zn deposition and dissolution and of the reversibility of the reaction after the addition of water.[200,202-205] Accordingly, the influence of water in the IL electrolyte on the electrochemical properties of Zn-air batteries and on the performance of the ORR/OER and the Zn plating/stripping processes as the main processes in these batteries are of considerable interest. In the measurements presented in chapter 3.5, this assumption can be confirmed: The addition of water in Zn^{2+}- and O_2-containing electrolyte leads to reversible peroxide formation, which is not suppressed by the presence of the Zn^{2+} ions. Compared to water-free electrolyte, which shows the formation of superoxide as dominant process, water leads to the formation of mainly peroxide species. Nevertheless, the formation of peroxide appears to be reversible. This means that the presence of water improves the performance of Zn-air batteries with ionic liquid electrolyte such that more electrons per O_2 molecule are transferred. Even though the Zn deposition / dissolution and ORR / OER characteristics of the IL electrolyte is improved by the addition of water, the kinetics of the ORR are still slow compared to aqueous electrolytes.

Overall, the present thesis contributes to the understanding of electrochemical processes in Li-ion and Metal-air batteries with focus on IL-based electrolytes. We studied the electrochemical decomposition and the ORR / OER in several IL based model electrolytes, including the influence of several additives. DEMS proved to be a suitable and flexible technique for investigating these very different model systems. The findings presented here are limited to model studies and can only cover a limited amount of ILs and additives, but we are confident that this work will be continued further and that our fundamental research will be used as a basis for further electrochemical studies. Even though ionic liquids show promising properties regarding electrochemical stability and the low volatility, several drawbacks such as low conductivity have to be overcome before they can be used as battery electrolytes. Maybe, with a better understanding of the electrode|electrolyte reactions, it will be possible to achieve a systematic optimization of this interface to build better Li-ion and metal-air batteries.

5 Zusammenfassung (German)

Aufgrund der begrenzten Verfügbarkeit und den fragwürdigen Bedingungen bei der Gewinnung von wichtigen Rohstoffen für konventionelle Lithium-Ionen Batterien, wie z.B. Lithium und Kobalt, ist es in der Zukunft unvermeidlich auf besser verfügbare Batteriematerialien auszuweichen, die aber nicht weniger effizient als die aktuell verwendeten sein dürfen. Die vorliegende Arbeit soll durch Untersuchungen von neuartigen Elektrodenmaterialien und Elektrolyten bezüglich ihrer Leistungsfähigkeit und im speziellen ihrer Stabilität für die Anwendung in Lithium-Ionen und Metall-Luft Batterien einen Teil dazu beitragen, lithium- und kobaltfreie Systeme zu entwickeln. Als geeignete Methode für diese Untersuchungen erwies sich die differentielle elektrochemische Massenspektrometrie (DEMS). Die Kombination aus elektrochemischen und massenspektrometrischen Messungen ermöglicht die zeitgleiche Verfolgung elektrochemischer Reaktionen und massenspektrometrischer Signale, woraus man Rückschlüsse auf die Reaktionsmechanismen während der Messung ziehen kann. Die Anpassung der elektrochemischen DEMS-Zellen an die spezifische Messaufgabe bzw. das zu untersuchende System ist dabei von zentraler Bedeutung für die Informationen, die bei der Messung erlangt werden können. Für die vorliegende Arbeit wurden drei unterschiedliche Zelltypen weiterentwickelt.

Für die Untersuchung an einem Elektrolytsystem mit flüchtigen Komponenten (Kapitel 3.1) wurde der Unterschied zwischen einer elektrochemischen Zelle, die mit einer Membran ausgestattet wurde, und einer Zelle ohne Membran gezeigt, wobei jede Zelle ihre eigenen Vor- und Nachteile aufweist: die Membranzelle erlaubt die Messung von geringen Produktmengen kleiner Moleküle, während die Zelle ohne Membran die Detektion von $LiPF_6$-Zersetzungsprodukten ermöglicht, die durch eine Membran verhindert wird. Die Kombination der Ergebnisse beider Zellen eröffnet somit ein genaueres Verständnis auf die stattfindenden elektrochemischen Zersetzungsprozesse.

Für Elektrolyte mit sehr geringem Dampfdruck kann hingegen eine offene Zelle verwendet werden, ohne dass es zu einem hohen Hintergrunddruck kommt. Aus diesem Grund ist dieses System für die Untersuchung von Zersetzungsmechanismen in ionischen Flüssigkeiten geeignet, die in den Kapiteln 3.2 und 3.3 untersucht werden. Möchte man dagegen Elektrolyte untersuchen, die zwar auf ionischen Flüssigkeiten basieren, aber noch zusätzliche leicht flüchtige Bestandteile wie O_2, NBH oder Kronenether enthalten, ist wiederum ein anderer Zelltyp zu verwenden. Für die Messung von ORR und OER in ionischen Flüssigkeiten mit mindestens einem der vorher genannten flüchtigen Bestandteile ist daher die Nutzung einer

elektrochemischen (Fluss-)Zelle mit Membran die beste Lösung (Kapitel 3.4 und 3.5). Die verwendete Flusszelle ermöglicht einen gleichmäßigen und kontrollierten Massentransport von O_2 an die Arbeitselektrode.

Durch die Wahl der richtigen Zelle ist DEMS insgesamt eine geeignete und vielseitige Methode für die Untersuchung der unterschiedlichsten Batteriesysteme und ermöglicht damit einen neuen Zugang zu den an Batterieelektroden ablaufenden Oberflächenreaktionen.

Ein erster Schritt für eine Verbesserung existierender Batteriesysteme ist die Verwendung von kobaltfreien Kathodenmaterialien. Aus diesem Grund wurde im Rahmen der vorliegenden Arbeit Li_xVO_2F in Kapitel 3.1 als potentielles Elektrodenmaterial untersucht. Von diesem Material wird vermutet, dass es aufgrund der Bildung von Peroxid- und Superoxid-Spezies während des Ladevorgangs eine erhöhte Kapazität im Vergleich zu momentan verwendeten Kathodenmaterialien besitzt. Daraus ergibt sich die Frage, ob sich das Material während kontinuierlicher Lade- und Entladezyklen als stabil erweist oder ob es sich als Nebenreaktion unter Sauerstoffentwicklung zersetzt Auch die Frage nach der Stabilität des eingesetzten LP30 Elektrolyt an der Li_2VO_2F Oberfläche bzw. die parallele Bildung von flüchtigen Zersetzungsprodukten aus dem Elektrolyten stellt sich in diesem Zusammenhang. Die Messungen haben ergeben, dass die Sauerstoffentwicklung in einer Zelle mit Membran untersucht werden muss, da für die Detektion geringer Mengen Sauerstoff der Hintergrunddruck bestehend aus Elektrolytbestandteilen möglichst gering sein muss, da diese ebenfalls Fragmente mit m/z = 32 erzeugen. Während des ersten kathodischen Scans ist in den Messungen ein Sauerstoffpeak zu sehen, der in den weiteren Zyklen bei positivem Potential nicht mehr auftritt. Dies ist ein Hinweis darauf, dass nach anfänglicher Oxidation von Verunreinigungen oder Zersetzung von Elektrodenbestandteilen, die in Sauerstoffentwicklung resultieren, das Material stabil bleibt und kein weiterer Sauerstoff freigesetzt wird. Parallel zu diesen Untersuchungen sind die Zersetzungsprodukte des Elektrolyten gemessen worden. In der Membranzelle kann im kathodischen Scan unter 1,5 V die Bildung von Ethylen beobachtet werden, während bei positiven Potentialen höher als 3,2 V CO_2-Entwicklung auftritt. Daraus ergibt sich ein elektrochemischer Stabilitätsbereich von 1,7 V. Im Gegensatz dazu konnte in der Zelle ohne Membran die Bildung von $LiPF_6$ Zersetzungsprodukten beobachtet werden, welche in der Zelle mit Membran nicht festgestellt worden ist.

Ein weiterer Schritt bei der Verbesserung von Batteriesystemen ist die Verwendung eines Elektrolyten mit großer elektrochemischer Stabilität. Daher hat sich in den letzten Jahren ein steigendes Interesse an der Untersuchung von ionischen Flüssigkeiten als Batterieelektrolyt

gezeigt. Neben der elektrochemischen Stabilität zeigen viele ionische Flüssigkeiten weitere positive Eigenschaften wie einen geringen Dampfdruck und geringe Entflammbarkeit. Aufgrund ihrer vielversprechenden Eigenschaften und kommerziellen Verfügbarkeit sind die ionischen Flüssigkeiten BMP-TFSI und EMIM-TFSI oft Gegenstand von Modelluntersuchungen gewesen und werden auch in der vorliegenden Arbeit verwendet.

Um die elektrochemische Stabilität von ionischen Flüssigkeiten weiter zu erhöhen ist es notwendig, den elektrochemischen Zersetzungsmechanismus zu verstehen. Ein erster Schritt ist dabei herauszufinden, bei welchem Potential die Zersetzung von Anion und Kation beginnt. Für diese Untersuchungen, die in Kapitel 3.2 gezeigt werden, ist ein neuartiger DEMS-Aufbau entwickelt worden, welcher die Unterscheidung von Zersetzungsprodukten ermöglicht, die an Arbeits- oder Gegenelektrode erzeugt werden. Die Ergebnisse haben gezeigt, dass die kathodische Stabilität an der eingesetzten Gold-Elektrode von der gleichzeitigen Zersetzung von Anion und Kation in reiner IL beeinflusst wird, wobei BMP^+ eine höhere Stabilität aufweist als $EMIM^+$. Die BMP^+ Zersetzung ereignet sich durch den Bindungsbruch zwischen dem Ring und der Butyl-Seitenkette, wodurch Methylpyrrolidin und Butyl gebildet wird. Durch die Detektion von Dibutylmethylamin kann ebenfalls auf eine Ringöffnung geschlossen werden. Auf die anodische Stabilität hingegen hat die Art des Kations keinen Einfluss.

In Kapitel 3.3 sind die Untersuchungen erweitert worden um den Einfluss des Elektrodenmaterials und den von Verunreinigungen aus der IL-Synthese auf den Zersetzungsmechanismus zu beleuchten. Ebenfalls wurde der Einfluss von Metallionen (Li^+ und Mg^{2+}), die als Ladungsträger ein unvermeidlicher Bestandteil des Batterieelektrolyten sind, auf die elektrochemische Stabilität des Elektrolyten untersucht. Der Wechsel des Elektrodenmaterials von Gold auf Glaskohlenstoff zeigt keinen starken Einfluss auf die Stabilität der ionischen Flüssigkeit, jedoch auf den Zersetzungsmechanismus. Auf der Glaskohlenstoff-Elektrode ist bei kathodischen Potentialen die $TFSI^-$ Zersetzung nun der vorherrschende Prozess, das Potentialfenster der Halbzelle bleibt dabei aber unberührt. Die Wahl des Herstellers von BMP-TFSI, Merck und Solvionic, zeigt ebenfalls einen starken Einfluss auf den Zersetzungsmechanismus. Auch wenn die genauen Gründe für diese Beobachtung unklar bleiben, vermuten wir, dass Rückstände aus der IL-Synthese dafür verantwortlich sind. Betrachten wir nun den Einfluss von Li^+ auf die Stabilität des Elektrolyten, kann auch hier ein starker Einfluss festgestellt werden. Die Anwesenheit von Li^+ Ionen verhindert im kathodischen Scan größtenteils die Bildung von flüchtigen Zersetzungsprodukten des BMP-TFSI basierten Elektrolyten, während aber gleichzeitig

Lithium Abscheidung und Auflösung beobachtet werden konnte. Ähnlich dazu beeinflusst die Anwesenheit von Mg^{2+} Ionen ebenfalls den Zersetzungsmechanismus von BMP-TFSI. Die starken Wechselwirkungen zwischen Mg^{2+} und $TFSI^-$ destabilisieren das $TFSI^-$ Anion gegenüber reduktiver Zersetzung, was in einer Verschiebung der Produktverteilung von hauptsächlich BMP^+ Fragmenten in reinem BMP-TFSI zu schwerpunktmäßig $TFSI^-$ Fragmenten in $Mg(TFSI)_2$ haltigem Elektrolyten resultiert; die Zersetzung von BMP^+ wird somit durch die Anwesenheit von Mg^{2+} erschwert. Ein weiterer sehr interessanter Effekt: es konnte kein Hinweis auf die Abscheidung von Magnesium gefunden werden, diese wird in diesem Elektrolytsystem scheinbar vollständig gehemmt. Nichtsdestotrotz, für die Verwendung in Metall-Luft Batterien sind nicht nur das Abscheideverhalten von Metallen und die elektrochemische Stabilität des Elektrolyten wichtige Punkte, sondern die Reversibilität der Sauerstoffreduktion ist ebenfalls von zentraler Bedeutung. Der elektrochemische Bereich, in dem ORR und OER stattfinden, liegt im aus Kapitel 3.3 bekannten Stabilitätsbereich des Elektrolyten. Frühere Messungen in unserer Arbeitsgruppe[51,63,64,78] haben gezeigt, dass in Mg^{2+} haltigem BMP-TFSI eine passivierende Schicht bestehend aus MgO und MgO_2 an der Elektrodenoberfläche gebildet wird. Ein Ansatz um die Ausbildung der Passivierungsschicht zu verhindern ist die Maskierung der Mg^{2+} Ionen durch Komplexbildner wie 18-Krone-6 oder NBH. Die in Kapitel 3.4 diskutierten Ergebnisse zeigen, dass überstöchiometrische Mengen an 18-Krone-6 im Elektrolyten die Mg^{2+} Ionen maskieren und somit eine Beteiligung von Mg^{2+} in der ORR verhindern. Das Elektrolytsystem verhält sich damit, was die ORR betrifft, wieder ähnlich der Messungen in magnesiumfreiem BMP-TFSI. Allerdings scheint die Zugabe von 18-Krone-6 auch die Menge an reduzierten Spezies (Superoxid und Peroxid) in der Nähe der Elektrodenoberfläche zu reduzieren, wodurch sich der OER Strom verringert, da die ORR Produkte vom konstanten Elektrolytfluss weggetragen werden. Die Zugabe von 0.1 M NBH anstelle von Kronenether ergibt ebenfalls eine langsamere Passivierung und eine höhere Reversibilität im Vergleich zu reinem BMP-TFSI. Insgesamt zeigen diese Ergebnisse die komplexe und vielseitige Rolle von Additiven auf, welche für weitere Untersuchungen in Bezug auf die Verbesserung der ORR/OER in Magnesium-Luft Batterien in Betracht gezogen werden sollten.

Als Vergleich zu den Untersuchungen an Mg^{2+} haltigem BMP-TFSI haben wir auch das Verhalten von Zn^{2+} in demselben Elektrolytsystem untersucht. Dabei kann in Zn^{2+} haltiger Lösung Zinkabscheidung beobachtet werden (vergleiche Kapitel 3.5), wohingegen bei Mg^{2+} keine Mg-Abscheidung beobachtet werden konnte.[51,63,64,78] Frühere Studien in ionischen Flüssigkeiten haben außerdem für die Zinkabscheidung und Zinkauflösung gezeigt, dass sich

die Reaktionskinetik und Reversibilität durch Zugabe von Wasser erhöht.[200,202-205] Aus diesem Grund muss der Einfluss von Wasser auf die elektrochemischen Eigenschaften von Zink-Luft Batterien, in der parallel ORR / OER mit der zuvor genannten Zinkabscheidung und Zinkauflösung abläuft, ebenfalls von entscheidender Bedeutung sein. In den in Kapitel 3.5 gezeigten Messungen kann dies bestätigt werden: Die Zugabe von Wasser in Zn^{2+} und O_2-haltigen Elektrolyten führt zu einer reversiblen Peroxidbildung. Die Bildung dieser Spezies wird dabei durch die Gegenwart von Zn^{2+} Ionen nicht behindert. Verglichen mit wasserfreiem Elektrolyten, bei dem Superoxid das Hauptprodukt ist, führt Wasser damit zu einer Verschiebung der Produktverteilung hin zu Peroxid. Dies zeigt, dass die Gegenwart von Wasser die Leistung von auf ionischen Flüssigkeiten basierenden Zink-Luft Batterien dadurch erhöhen kann, dass mehr Elektronen pro Sauerstoffmolekül übertragen werden können. Allerdings, auch wenn die Zugabe von Wasser die Zink Abscheidung / Auflösung und die ORR / OER Eigenschaften des IL Elektrolyten verbessert, ist die Kinetik der ORR dennoch langsam im Vergleich zu wässrigem Elektrolyten.

Insgesamt soll diese Arbeit zum Verständnis der elektrochemischen Prozesse in Li-ionen und Metall-Luft Batterien beitragen, wobei ein Fokus auf die Untersuchung von IL-basierten Elektrolyten gelegt worden ist. Für einige IL-basierte Modellelektrolyte sind die elektrochemischen Zersetzungsreaktionen an den Potentialgrenzen und das Verhalten der ORR / OER untersucht worden, auch unter Zusatz von Additiven. Bei diesen Untersuchungen hat sich DEMS als anpassungsfähige Methode erwiesen, mit der sich Informationen über eine Vielzahl unterschiedlicher Systeme mit jeweils sehr unterschiedlichen Anforderungen an die jeweilige Messaufgabe gewinnen lässt. Die hier gezeigten Ergebnisse beschränken sich auf Modellstudien und können nur eine kleine Auswahl an interessanten ionischen Flüssigkeiten und Additiven abdecken, aber ich bin zuversichtlich, dass diese Arbeit weiter fortgeführt werden kann und die vorliegenden Ergebnisse eine Grundlage für weitere elektrochemische Untersuchungen sein werden. Auch wenn ionische Flüssigkeiten aufgrund der hohen elektrochemischen Stabilität und des geringen Dampfdrucks als sehr vielversprechend erscheinen, gibt es dennoch einige Nachteile wie eine geringe Leitfähigkeit, die überwunden werden müssen, bevor sie als Batterieelektrolyte eingesetzt werden können. Vielleicht wird es irgendwann möglich sein auf Grundlage eines besseren und systematischen Verständnisses der Grenzflächenreaktionen zwischen Elektrode und Elektrolyt zielgerichtet Verbesserungen an dieser Grenzfläche vornehmen zu können und dadurch bessere Lithium-Ionen und Metall-Luft Batterien zu entwickeln.

6 Bibliography

[1] M. Armand and J.-M. Tarascon, Nature, 451, **2008**, 652.

[2] J.B. Goodenough and K.S. Park, J. Am. Chem. Soc., 135, **2013**, 1167-1176.

[3] M.S. Whittingham, Chem. Rev., 104, **2004**, 4271-4302.

[4] J. Lee, A. Urban, X. Li, D. Su, G. Hautier, and G. Ceder, Science, 343, **2014**, 519.

[5] K. Mizushima, P.C. Jones, P.J. Wiseman, and J.B. Goodenough, Mater. Res. Bull., 15, **1980**, 783-789.

[6] A. Manthiram, Nature Comm., 11, **2020**, 1550.

[7] N. Nitta, F. Wu, J.T. Lee, and G. Yushin, Mater. Today, 18, **2015**, 252-264.

[8] A.C. Luntz and B.D. McCloskey, Chem. Rev., 114, **2014**, 11721-11750.

[9] L. Li and A. Manthiram, Adv. Energy Mater., 6, **2016**, 1502054.

[10] S. Ren, X. Duan, S. Liang, M. Zhang, and H. Zheng, J. Mater. Chem. A, 8, **2020**, 6144-6182.

[11] J.K. Norskov, J. Rossmeisl, A. Logadottir, L. Lindqvist, J.R. Kitchin, T. Bligaard, and H. Jonsson, J. Phys. Chem. B, 108, **2004**, 17886-17892.

[12] Z.W. Seh, J. Kibsgaard, C.F. Dickens, I. Chorkendorff, J.K. Norskov, and T.F. Jaramillo, Science, 355, **2017**, eaad4998.

[13] Y. NuLi, J. Yang, J. Wang, J. Xu, and P. Wang, Electrochem. Solid-State Lett., 8, **2005**, C166-C169.

[14] Z. Ma, D.R. MacFarlane, and M. Kar, Batteries & Supercaps, 2, **2019**, 115-127.

[15] M. Kar, B. Winther-Jensen, M. Armand, T.J. Simons, O. Winther-Jensen, M. Forsyth, and D.R. MacFarlane, Electrochim. Acta, 188, **2016**, 461-471.

[16] M. Kar, T.J. Simons, M. Forsyth, and D.R. MacFarlane, Phys. Chem. Chem. Phys., 16, **2014**, 18658-18674.

[17] Y. Wang, R. Ohnishi, E. Yoo, P. He, J. Kubota, K. Domen, and H. Zhou, J. Mater. Chem., 22, **2012**, 15549-15555.

[18] D. Strmcnik, D.F. van der Vliet, K.C. Chang, V. Komanicky, K. Kodama, H. You, V.R. Stamenkovic, and N.M. Markovic, J. Phys. Chem. Lett., 2, **2011**, 2733-2736.

[19] R. Devivaraprasad, R. Ramesh, N. Naresh, T. Kar, R.K. Singh, and M. Neergat, Langmuir, 30, **2014**, 8995-9006.

[20] A.R. Mainar, E. Iruin, L.C. Colmenares, A. Kvasha, I. de Meatza, M. Bengoechea, O. Leonet, I. Boyano, Z. Zhang, and J.A. Blazquez, J. Energy Storage, 15, **2018**, 304-328.

[21] N. Akhtar and W. Akhtar, Int. J. Energy Res., 39, **2015**, 303-316.

[22] C.J. Allen, J. Hwang, R. Kautz, S. Mukerjee, E.J. Plichta, M.A. Hendrickson, and K.M. Abraham, J. Phys. Chem. C, 116, **2012**, 20755-20764.

[23] A. Khan, C.A. Gunawan, and C. Zhao, ACS Sustainable Chem. Eng., 5, **2017**, 3698-3715.

[24] E.E. Switzer, R. Zeller, Q. Chen, K. Sieradzki, D.A. Buttry, and C. Friesen, J. Phys. Chem. C, 117, **2013**, 8683-8690.

[25] F. Endres and S. Zein El Abedin, Phys. Chem. Chem. Phys., 8, **2006**, 2101-2116.

[26] T. Waldmann, H.H. Huang, H.E. Hoster, O. Höfft, F. Endres, and R.J. Behm, ChemPhysChem, 12, **2011**, 2565-2567.

[27] D.S. Silvester and R.G. Compton, Z. Phys. Chem., 220, **2006**, 1247.

[28] K.R. Seddon, J. Chem. Technol. Biotechnol., 68, **1997**, 351-356.

[29] J.S. Wilkes, J.A. Levisky, R.A. Wilson, and C.L. Hussey, Inorg. Chem., 21, **1982**, 1263-1264.

[30] R. Ferraz, L.C. Branco, C. Prudencio, J.P. Noronha, and Z. Petrovski, ChemMedChem, 6, **2011**, 975-985.

[31] K. Xu and C. Wang, Nature Energy, 1, **2016**, 16161.

[32] M. Galinski, A. Lewandowski, and I. Stepniak, Electrochim. Acta, 51, **2006**, 5567-5580.

[33] R. Atkin, S.Z.E. Abedin, R. Hayes, L.H.S. Gasparotto, N. Borisenko, and F. Endres, J. Phys. Chem. C, 113, **2009**, 13266-13272.

[34] S. Randström, M. Montanino, G.B. Appetecchi, C. Lagergren, A. Moreno, and S. Passerini, Electrochim. Acta, 53, **2008**, 6397-6401.

[35] P.C. Howlett, E.I. Izgorodina, M. Forsyth, and D.R. MacFarlane, Z. Phys. Chem., 220, **2006**, 1483.

[36] J. Vatamanu, L. Xing, W. Li, and D. Bedrov, Phys. Chem. Chem. Phys., 16, **2014**, 5174-5182.

[37] S. Kondrat, N. Georgi, M.V. Fedorov, and A.A. Kornyshev, Phys. Chem. Chem. Phys., 13, **2011**, 11359-11366.

[38] H. Yildirim, J.B. Haskins, C.W. Bauschlicher, and J.W. Lawson, J. Phys. Chem. C, 121, **2017**, 28214-28234.

[39] J.B. Haskins, H. Yildirim, C.W. Bauschlicher, and J.W. Lawson, J. Phys. Chem. C, 121, **2017**, 28235-28248.

[40] S.E. Goodwin, J.S. Gibson, R.G. Jones, and D.A. Walsh, Electrochem. Commun., 90, **2018**, 111-115.

[41] N. Schweikert, A. Hofmann, M. Schulz, M. Scheuermann, S.T. Boles, T. Hanemann, H. Hahn, and S. Indris, J. Power Sources, 228, **2013**, 237-243.

[42] S.J. An, J. Li, C. Daniel, D. Mohanty, S. Nagpure, and D.L. Wood, Carbon, 105, **2016**, 52-76.

[43] D.R. MacFarlane, P. Meakin, J. Sun, N. Amini, and M. Forsyth, J. Phys. Chem. B, 103, **1999**, 4164-4170.

[44] P.A.Z. Suarez, V.M. Selbach, J.E.L. Dullius, S. Einloft, C.M.S. Piatnicki, D.S. Azambuja, R.F. de Souza, and J. Dupont, Electrochim. Acta, 42, **1997**, 2533-2535.

[45] U. Schröder, J.D. Wadhawan, R.G. Compton, F. Marken, P.A.Z. Suarez, C.S. Consorti, R.F. de Souza, and J.r. Dupont, New J. Chem., 24, **2000**, 1009-1015.

[46] M.C. Kroon, W. Buijs, C.J. Peters, and G.J. Witkamp, Green Chem., 8, **2006**, 241-245.

[47] P.C. Howlett, D.R. MacFarlane, and A.F. Hollenkamp, Electrochem. Solid-State Lett., 7, **2004**, A97-A101.

[48] J.B. Haskins, C.W. Bauschlicher, and J.W. Lawson, J. Phys. Chem. B, 119, **2015**, 14705-14719.

[49] Y. Katayama, H. Onodera, M. Yamagata, and T. Miura , J. Electrochem. Soc., 151, **2004**, A59-A63.

[50] L. Cecchetto, M. Salomon, B. Scrosati, and F. Croce, J. Power Sources, 213, **2012**, 233-238.

[51] J. Schnaidt, T.L. Nguyen, Z. Jusys, and R.J. Behm, Electrochim. Acta, 299, **2019**, 372-377.

[52] T. Reier, M. Oezaslan, and P. Strasser, ACS Catal., 2, **2012**, 1765-1772.

[53] H. Dau, C. Limberg, T. Reier, M. Risch, S. Roggan, and P. Strasser, ChemCatChem, 2, **2010**, 724-761.

[54] H.S. Wroblowa, C.P. Yen, and G. Razumney, J. electroanal. chem. interfacial electrochem., 69, **1976**, 195-201.

[55] A. Damjanovic, D.B. Sepa, and M.V. Vojnovic, Electrochim. Acta, 24, **1979**, 887-889.

[56] S.J. Clouser, J.C. Huang, and E. Yeager, J. Appl. Electrochem., 23, **1993**, 597-605.

[57] F. Si, Y. Zhang, L. Yan, J. Zhu, M. Xiao, C. Liu, W. Xing, and J. Zhang, 4 - Electrochemical Oxygen Reduction Reaction, in: W. Xing, G. Yin, and J. Zhang (Eds.), Rotating Electrode Methods and Oxygen Reduction Electrocatalysts, Elsevier, Amsterdam, 2014, pp. 133-170.

[58] M. Eckardt, K. Sakaushi, A. Lyalin, M. Wassner, N. Hüsing, T. Taketsugu, and R.J. Behm, Electrochim. Acta, 299, **2019**, 736-748.

[59] Y.J. Wang, W. Long, L. Wang, R. Yuan, A. Ignaszak, B. Fang, and D.P. Wilkinson, Energy Environ. Sci., 11, **2018**, 258-275.

[60] T. Murata, K. Kotsuki, H. Murayama, R. Tsuji, and Y. Morita, Comm. Chem., 2, **2019**, 46.

[61] X. Wang, Z. Li, Y. Qu, T. Yuan, W. Wang, Y. Wu, and Y. Li, Chem, 5, **2019**, 1486-1511.

[62] Y. Nie, L. Li, and Z. Wei, Chem. Soc. Rev., 44, **2015**, 2168-2201.

[63] Y.T. Law, J. Schnaidt, S. Brimaud, and R.J. Behm, J. Power Sources, 333, **2016**, 173-183.

[64] M. Bozorgchenani, P. Fischer, J. Schnaidt, T. Diemant, R.M. Schwarz, M. Marinaro, M. Wachtler, L. Jörissen, and R.J. Behm, ChemElectroChem, 5, **2018**, 2600-2611.

[65] P. Reinsberg, C. Bondue, and H. Baltruschat, Electrochim. Acta, 200, **2016**, 214-221.

[66] S. Bruckenstein and R.R. Gadde, J. Am. Chem. Soc., 93, **1971**, 793-794.

[67] O. Wolter and J. Heitbaum, Berichte der Bunsengesellschaft für physikalische Chemie, 88, **1984**, 2-6.

[68] S. Venkatachalam, R.J. Angelici, L.K. Woo, and A.C. Hillier, Anal. Chem., 85, **2013**, 6059-6065.

[69] H. Baltruschat, J. Am. Soc. Mass Spectr., 15, **2004**, 1693-1706.

[70] Z. Jusys, H. Massong, and H. Baltruschat, J. Electrochem. Soc., 146, **1999**, 1093-1098.

[71] M. Wohlfahrt-Mehrens and J. Heitbaum, J. electroanal. chem. interfacial electrochem., 237, **1987**, 251-260.

[72] S. Fierro, T. Nagel, H. Baltruschat, and C. Comninellis, Electrochem. Commun., 9, **2007**, 1969-1974.

[73] C. Cremers, T. Jurzinsky, J. Meier, A. Schade, M. Branghofer, K. Pinkwart, and J. Tübke, J. Electrochem. Soc., 165, **2018**, F3307-F3315.

[74] C. Gebauer, P. Fischer, M. Wassner, T. Diemant, Z. Jusys, N. Hüsing, and R.J. Behm, Nano Energy, 29, **2016**, 136-148.

[75] C. Spöri, J.T.H. Kwan, A. Bonakdarpour, D.P. Wilkinson, and P. Strasser, Angew. Chem. Int. Ed., 56, **2017**, 5994-6021.

[76] B.D. McCloskey, D.S. Bethune, R.M. Shelby, G. Girishkumar, and A.C. Luntz, J. Phys. Chem. Lett., 2, **2011**, 1161-1166.

[77] C.L. Bender, P. Hartmann, M. Vracar, P. Adelhelm, and J. Janek, Adv. Energ. Mat., 4, **2014**, 1301863.

[78] Z. Jusys, J. Schnaidt, and R.J. Behm, J. Chem. Phys., 150, **2018**, 041724.

[79] G. Garcia, W. Schuhmann, and E. Ventosa, ChemElectroChem, 3, **2016**, 592-597.

[80] L. Ma, M.A. Schroeder, T.P. Pollard, O. Borodin, M.S. Ding, R. Sun, L. Cao, J. Ho, D.R. Baker, C. Wang, and K. Xu, Energy Environ. Mater., n/a, **2020**.

[81] P.T. Kissinger and W.R. Heineman, J. Chem. Educ., 60, **1983**, 702.

[82] G.A. Snook, A.S. Best, A.G. Pandolfo, and A.F. Hollenkamp, Electrochem. Commun., 8, **2006**, 1405-1411.

[83] C.R. Müller, Elektrochemische und bildgebende Untersuchungen zur Struktur der Phasengrenzfläche zwischen ionischen Flüssigkeiten und wohldefinierten Elektrodenoberflächen. 11-8-2017. Universität Ulm.
Thesis/Dissertation

[84] Y. Katayama, R. Fukui, and T. Miura, J. Electrochem. Soc., 154, **2007**, D534-D537.

[85] Y. Katayama, K. Sekiguchi, M. Yamagata, and T. Miura, J. Electrochem. Soc., 152, **2005**, E247-E250.

[86] R. Wibowo, S.E. Ward Jones, and R.G. Compton, J. Phys. Chem. B, 113, **2009**, 12293-12298.

[87] R.A. Pasternak, G.L. Burns, and J. Heller, Macromolecules, 4, **1971**, 470-475.

[88] K.A. Connors, Drug Dev. Ind. Pharm., 14, **1988**, 1891-1903.

[89] K. Fischer, Angewandte Chemie, 48, **1935**, 394-396.

[90] G. Wedler, Lehrbuch der Physikalischen Chemie, WILEY-VCH Verlag GmbH Co. KGaA, Weinheim, 2004.

[91] J.W.Niemantsverdriet, The Ion Spectroscopies, Spectroscopy in Catalysis, WILEY-VCH Verlag GmbH Co. KGaA, Weinheim, 2007, pp. 85-119.

[92] J.H. Chang, C. Baur, J.M. Ateba Mba, D. Arcon, G. Mali, D. Alwast, R.J. Behm, M. Fichtner, T. Vegge, and J.M. Garcia Lastra, J. Mater. Chem. A, **2020**.

[93] M.S. Whittingham, Science, 192, **1976**, 1126.

[94] A. Yoshino, Angew. Chem. Int. Ed., 51, **2012**, 5798-5800.

[95] K. Xu, Chem. Rev., 104, **2004**, 4303-4418.

[96] J. Kalhoff, G.G. Eshetu, D. Bresser, and S. Passerini, ChemSusChem, 8, **2015**, 2154-2175.

[97] J.Y. Lin, C.C. Hsu, H.P. Ho, and S.h. Wu, Electrochim. Acta, 87, **2013**, 126-132.

[98] Y.P. Wu, E. Rahm, and R. Holze, J. Power Sources, 114, **2003**, 228-236.

[99] M.G.S.R. Thomas, W.I.F. David, J.B. Goodenough, and P. Groves, Mater. Res. Bull., 20, **1985**, 1137-1146.

[100] J.R. Dahn, U. von Sacken, and C.A. Michal, Solid State Ionics, 44, **1990**, 87-97.

[101] C. Chazel, M. Menetrier, L. Croguennec, and C. Delmas, Inorg. Chem., 45, **2006**, 1184-1191.

[102] M.M. Thackeray, P.J. Johnson, L.A. de Picciotto, P.G. Bruce, and J.B. Goodenough, Mater. Res. Bull., 19, **1984**, 179-187.

[103] A. Urban, J. Lee, and G. Ceder, Adv. Energy Mater., 4, **2014**, 1400478.

[104] C. Baur, I. Källquist, J. Chable, J.H. Chang, R.E. Johnsen, F. Ruiz-Zepeda, J.M. Ateba Mba, A.J. Naylor, J.M. Garcia-Lastra, T. Vegge, F. Klein, A.R. Schür, P. Norby, K. Edström, M. Hahlin, and M. Fichtner, J. Mater. Chem. A, 7, **2019**, 21244-21253.

[105] I. Källquist, A.J. Naylor, C. Baur, J. Chable, J. Kullgren, M. Fichtner, K. Edström, D. Brandell, and M. Hahlin, Chem. Mater., 31, **2019**, 6084-6096.

[106] V.K. Shen, D.W. Siderius, W.P. Krekelberg, and H.W. Hatch, NIST Standard Reference Simulation Website, NIST Standard Reference Database Number 173, National Institute of Standards and Technology, Gaithersburg MD, 2018.

[107] A. Gueguen, D. Streich, M. He, M. Mendez, F.F. Chesneau, P. Novak, and E.J. Berg, J. Electrochem. Soc., 163, **2016**, A1095-A1100.

[108] S.E. Renfrew and B.D. McCloskey, J. Am. Chem. Soc., 139, **2017**, 17853-17860.

[109] M.A. Cambaz, B.P. Vinayan, S.A. Pervez, R.E. Johnsen, H. Geßwein, A.A. Guda, Y.V. Rusalev, M.K. Kinyanjui, U. Kaiser, and M. Fichtner, Chem. Mater., 31, **2019**, 7941-7950.

[110] D. Alwast, J. Schnaidt, Y.T. Law, and R.J. Behm, Electrochim. Acta, 197, **2016**, 290-299.

[111] T. Kuboki, T. Okuyama, T. Ohsaki, and N. Takami, J. Power Sources, 146, **2005**, 766-769.

[112] J. Zhang and A.M. Bond, Analyst, 130, **2005**, 1132-1147.

[113] M. Armand, F. Endres, D.R. MacFarlane, H. Ohno, and B. Scrosati, Nat. Mater., 8, **2009**, 621-629.

[114] G. Girishkumar, B. McCloskey, A.C. Luntz, S. Swanson, and W. Wilcke, J. Phys. Chem. Lett., 1, **2010**, 2193-2203.

[115] M. Shamsipur, A.A.M. Beigi, M. Teymouri, S.M. Pourmortazavi, and M. Irandoust, J. Mol. Liq., 157, **2010**, 43-50.

[116] P. Bonhôte, A.P. Dias, N. Papageorgiou, K. Kalyanasundaram, and M. Grätzel, Inorg. Chem., 35, **1996**, 1168-1178.

[117] F. Endres, S.Z. ElAbedin, and N. Borissenko, Z. Phys. Chem., 220, **2015**, 1377-1394.

[118] N. De Vos, C. Maton, and C.V. Stevens, ChemElectroChem, 1, **2014**, 1258-1270.

[119] V.R. Koch, L.A. Dominey, C. Nanjundiah, and M.J. Ondrechen, J. Electrochem. Soc., 143, **1996**, 798-803.

[120] P. Novak, D. Goers, L. Hardwick, M. Holzapfel, W. Scheifele, J. Ufheil, and A. Würsig, J. Power Sources, 146, **2005**, 15-20.

[121] N. Tsiouvaras, S. Meini, I. Buchberger, and H.A. Gasteiger, J. Electrochem. Soc., 160, **2013**, A471-A477.

[122] J.H. Shin, W.A. Henderson, and S. Passerini, J. Electrochem. Soc., 152, **2005**, A978-A983.

[123] F. Endres and S. Zein El Abedin, Z. Phys. Chem., 221, **2007**, 1407-1427.

[124] D.R. MacFarlane, M. Forsyth, P.C. Howlett, J.M. Pringle, J. Sun, G. Annat, W. Neil, and E.I. Izgorodina, Acc. Chem. Res., 40, **2007**, 1165-1173.

[125] E. Markevich, R. Sharabi, V. Borgel, H. Gottlieb, G. Salitra, D. Aurbach, G. Semrau, and M.A. Schmidt, Electrochim. Acta, 55, **2010**, 2687-2696.

[126] C. Zhao, A.M. Bond, and X. Lu, Anal. Chem., 84, **2012**, 2784-2791.

[127] G.H. Lane, Electrochim. Acta, 83, **2012**, 513-528.

[128] M.C. Buzzeo, R.G. Evans, and R.G. Compton, ChemPhysChem, 5, **2004**, 1106-1120.

[129] S.P. Ong, O. Andreussi, Y. Wu, N. Marzari, and G. Ceder, Chem. Mater., 23, **2011**, 2979-2986.

[130] A. Garcia-Mendoza and J.C. Aguilar, Electrochim. Acta, 182, **2015**, 238-246.

[131] S. Randström, G.B. Appetecchi, C. Lagergren, A. Moreno, and S. Passerini, Electrochim. Acta, 53, **2007**, 1837-1842.

[132] L. Xiao and K.E. Johnson, J. Electrochem. Soc., 150, **2003**, E307-E311.

[133] R. Wen, B. Rahn, and O.M. Magnussen, Angew. Chem. Int. Ed., 54, **2015**, 6062-6066.

[134] N. Borisenko, S. Zein El Abedin, and F. Endres, J. Phys. Chem. C, 110, **2006**, 6250-6256.

[135] M. Drüschler, B. Huber, S. Passerini, and B. Roling, J. Phys. Chem. C, 114, **2010**, 3614-3617.

[136] S. Xiong, K. Xie, E. Blomberg, P. Jacobsson, and A. Matic, J. Power Sources, 252, **2014**, 150-155.

[137] C.C. Nguyen, S.W. Woo, and S.W. Song, J. Phys. Chem. C, 116, **2012**, 14764-14771.

[138] D. Aurbach, O. Chusid, I. Weissman, and P. Dan, Electrochim. Acta, 41, **1996**, 747-760.

[139] P.C. Howlett, N. Brack, A.F. Hollenkamp, M. Forsyth, and D.R. MacFarlane, J. Electrochem. Soc., 153, **2006**, A595-A606.

[140] A.M. Duffield, H. Budzikiewicz, D.H. Williams, and C. Djerassi, J. Am. Chem. Soc., 87, **1965**, 810-816.

[141] R.S. Gohlke and F.W. McLafferty, Anal. Chem., 34, **1962**, 1281-1287.

[142] M.J. O'Neal and T.P. Wier, Anal. Chem., 23, **1951**, 830-843.

[143] Y.H. Tian, G.S. Goff, W.H. Runde, and E.R. Batista, J. Phys. Chem. B, 116, **2012**, 11943-11952.

[144] A. Tolstogouzov, U. Bardi, O. Nishikawa, and M. Taniguchi, Int. J. Mass Spectrom., 281, **2009**, 37-40.

[145] D. Alwast, J. Schnaidt, K. Hancock, G. Yetis, and R.J. Behm, ChemElectroChem, 6, **2019**, 3009-3019.

[146] A. Fernicola, F. Croce, B. Scrosati, T. Watanabe, and H. Ohno, J. Power Sources, 174, **2007**, 342-348.

[147] P. Hapiot and C. Lagrost, Chem. Rev., 108, **2008**, 2238-2264.

[148] A. Lahiri, T. Schubert, B. Iliev, and F. Endres, Phys. Chem. Chem. Phys., 17, **2015**.

[149] M. Watanabe, M.L. Thomas, S. Zhang, K. Ueno, T. Yasuda, and K. Dokko, Chem. Rev., 117, **2017**, 7190-7239.

[150] M. Moreno, E. Simonetti, G.B. Appetecchi, M. Carewska, M. Montanino, G.T. Kim, N. Loeffler, and S. Passerini, J. Electrochem. Soc., 164, **2017**, A6026-A6031.

[151] S. Ferrari, E. Quartarone, C. Tomasi, M. Bini, P. Galinetto, M. Fagnoni, and P. Mustarelli, J. Electrochem. Soc., 162, **2015**, A3001-A3006.

[152] G.A. Giffin, J. Mater. Chem. A, 4, **2016**, 13378-13389.

[153] N. Mozhzhukhina, A.Y. Tesio, L.P.M. De Leo, and E.J. Calvo, J. Electrochem. Soc., 164, **2017**, A518-A523.

[154] R. Mohtadi and F. Mizuno, Beilstein J. Nanotechnol., 5, **2014**, 1291-1311.

[155] H.D. Yoo, I. Shterenberg, Y. Gofer, G. Gershinsky, N. Pour, and D. Aurbach, Energy Environ. Sci., 6, **2013**, 2265-2279.

[156] G.A. Giffin, A. Moretti, S. Jeong, and S. Passerini, J. Phys. Chem. C, 118, **2014**, 9966-9973.

[157] S. Jeremias, G.A. Giffin, A. Moretti, S. Jeong, and S. Passerini, J. Phys. Chem. C, 118, **2014**, 28361-28368.

[158] K. Sodeyama, Y. Yamada, K. Aikawa, A. Yamada, and Y. Tateyama, J. Phys. Chem. C, 118, **2014**, 14091-14097.

[159] N.N. Rajput, X. Qu, N. Sa, A.K. Burrell, and K.A. Persson, J. Am. Chem. Soc., 137, **2015**, 3411-3420.

[160] R. Atkin, N. Borisenko, M. Drüschler, S.Z. El Abedin, F. Endres, R. Hayes, B. Huber, and B. Roling, Phys. Chem. Chem. Phys., 13, **2011**, 6849-6857.

[161] R. Wibowo, L. Aldous, R.M.J. Jacobs, N.S.A. Manan, and R.G. Compton, Chem. Phys. Lett., 517, **2011**, 103-107.

[162] M. Tulodziecki, J.M. Tarascon, P.L. Taberna, and C. Guery, Electrochem. Commun., 77, **2017**, 128-132.

[163] A.M. OMahony, D.S. Silvester, L. Aldous, C. Hardacre, and R.G. Compton, J. Chem. Eng. Data, 53, **2008**, 2884-2891.

[164] G.T. Cheek, W.E. O'Grady, S.Z. El Abedin, E.M. Moustafa, and F. Endres, J. Electrochem. Soc., 155, **2008**, D91-D95.

[165] E. Knipping, C. Aucher, G. Guirado, and L. Aubouy, New J. Chem., 42, **2018**, 4693-4699.

[166] M. Eckardt, D. Alwast, J. Schnaidt, and R.J. Behm, ChemSusChem, 13, **2020**, 3919-3927.

[167] Y. Li and H. Dai, Chem. Soc. Rev., 43, **2014**, 5257-5275.

[168] J.S. Lee, S. Tai Kim, R. Cao, N.S. Choi, M. Liu, K.T. Lee, and J. Cho, Adv. Energy Mater., 1, **2011**, 34-50.

[169] Z.L. Wang, D. Xu, J.J. Xu, and X.B. Zhang, Chem. Soc. Rev., 43, **2014**, 7746-7786.

[170] M. Xu, D.G. Ivey, Z. Xie, and W. Qu, J. Power Sources, 283, **2015**, 358-371.

[171] J. Fu, Z.P. Cano, M.G. Park, A. Yu, M. Fowler, and Z. Chen, Adv. Mater., 29, **2017**.

[172] P. Gu, M. Zheng, Q. Zhao, X. Xiao, H. Xue, and H. Pang, J. Mater. Chem. A, 5, **2017**, 7651-7666.

[173] J. Fu, R. Liang, G. Liu, A. Yu, Z. Bai, L. Yang, and Z. Chen, Adv. Mater., 0, **2018**, 1805230.

[174] F. Mizuno, S. Nakanishi, Y. Kotani, S. Yokoishi, and H. Iba, Electrochemistry, 78, **2010**, 403-405.

[175] M. Rahman, X. Wang, and C. Wen, J. Electrochem. Soc., 160, **2013**, A1759-A1771.

[176] T. Zhang, Z. Tao, and J. Chen, Mater. Horiz., 1, **2014**, 196-206.

[177] G. Vardar, J.G. Smith, T. Thompson, K. Inagaki, J. Naruse, H. Hiramatsu, A.E.S. Sleightholme, J. Sakamoto, D.J. Siegel, and C.W. Monroe, Chem. Mater., 28, **2016**, 7629-7637.

[178] D. Sharon, D. Hirshberg, M. Afri, A.A. Frimer, M. Noked, and D. Aurbach, J. Solid State Electr., 21, **2017**, 1861-1878.

[179] Y. Sun, X. Liu, Y. Jiang, J. Li, J. Ding, W. Hu, and C. Zhong, J. Mater. Chem. A, 7, **2019**, 18183-18208.

[180] G. Vardar, A.E.S. Sleightholme, J. Naruse, H. Hiramatsu, D.J. Siegel, and C.W. Monroe, ACS Appl. Mater. Interfaces, 6, **2014**, 18033-18039.

[181] F. Sagane, K. Ogi, A. Konno, and K. Kanamura, J. Electrochem. Soc., 166, **2019**, A5054-A5058.

[182] S. Matsuda, K. Uosaki, and S. Nakanishi, J. Power Sources, 353, **2017**, 138-143.

[183] D. Alwast, J. Schnaidt, Z. Jusys, and R.J. Behm, J. Electrochem. Soc., 167, **2020**.

[184] F. Sagane, K. Ogi, A. Konno, M. Egashira, and K. Kanamura, Electrochemistry, 84, **2016**, 76-78.

[185] X.Z. Yuan, V. Alzate, Z. Xie, D.G. Ivey, and W. Qu, J. Electrochem. Soc., 161, **2014**, A451-A457.

[186] J. Herranz, A. Garsuch, and H.A. Gasteiger, J. Phys. Chem. C, 116, **2012**, 19084-19094.

[187] S. Monaco, A.M. Arangio, F. Soavi, M. Mastragostino, E. Paillard, and S. Passerini, Electrochim. Acta, 83, **2012**, 94-104.

[188] A.W. Lodge, M.J. Lacey, M. Fitt, N. Garcia-Araez, and J.R. Owen, Electrochim. Acta, 140, **2014**, 168-173.

[189] J.G. Smith, J. Naruse, H. Hiramatsu, and D.J. Siegel, Chem. Mater., 29, **2017**, 3152-3163.

[190] M. Mao, T. Gao, S. Hou, and C. Wang, Chem. Soc. Rev., 47, **2018**, 8804-8841.

[191] G. Vardar, E.G. Nelson, J.G. Smith, J. Naruse, H. Hiramatsu, B.M. Bartlett, A.E.S. Sleightholme, D.J. Siegel, and C.W. Monroe, Chem. Mater., 27, **2015**, 7564-7568.

[192] I. Weber, J. Ingenmey, J. Schnaidt, B. Kirchner, and R.J. Behm, Influence of Complexing Additives on the Reversible Deposition / Dissolution of Magnesium in an Ionic Liquid. 2021.
Unpublished Work

[193] M. Bremer, G. Linti, H. Nöth, M. Thomann-Albach, and G.E.W.J. Wagner, Z. anorg. allg. Chem., 631, **2005**, 683-697.

[194] Y. Shao, T. Liu, G. Li, M. Gu, Z. Nie, M. Engelhard, J. Xiao, D. Lv, C. Wang, J.G. Zhang, and J. Liu, Sci. Rep., 3, **2013**, 3130.

[195] R. Mainar, O. Leonet, M. Bengoechea, I. Boyano, I. de Meatza, A. Kvasha, A. Guerfi, and J. Alberto Blazquez, Int. J. Energy Res., 40, **2016**, 1032-1049.

[196] G. Koscher and K. Kordesch, J. Power Sources, 136, **2004**, 215-219.

[197] L. Jörissen, J. Power Sources, 155, **2006**, 23-32.

[198] S. Liu, W. Han, B. Cui, X. Liu, F. Zhao, J. Stuart, and S. Licht, J. Power Sources, 342, **2017**, 435-441.

[199] J.F. Drillet, F. Holzer, T. Kallis, S. Müller, and V.M. Schmidt, Phys. Chem. Chem. Phys., 3, **2001**, 368-371.

[200] B. Dilasari, Y. Jung, and K. Kwon, J. Ind. Eng. Chem., 45, **2017**, 375-379.

[201] T.J. Simons, D.R. MacFarlane, M. Forsyth, and P.C. Howlett, ChemElectroChem, 1, **2014**, 1688-1697.

[202] M. Xu, D.G. Ivey, Z. Xie, W. Qu, and E. Dy, Electrochim. Acta, 97, **2013**, 289-295.

[203] T.J. Simons, A.A.J. Torriero, P.C. Howlett, D.R. MacFarlane, and M. Forsyth, Electrochem. Commun., 18, **2012**, 119-122.

[204] Z. Liu, S.Z. El Abedin, and F. Endres, Phys. Chem. Chem. Phys., 17, **2015**, 15945-15952.

[205] M.S. Ghazvini, G. Pulletikurthi, T. Cui, C. Kuhl, and F. Endres, J. Electrochem. Soc., 165, **2018**, D354-D363.

[206] I.M. AlNashef, M.L. Leonard, M.C. Kittle, M.A. Matthews, and J. Weidner, Electrochem. Solid-State Lett., 4, **2001**, D16-D18.

[207] L. Xiong, E.O. Barnes, and R.G. Compton, Sens. Actuators, B, 200, **2014**, 157-166.

[208] M. Islam, B.N. Ferdousi, T. Okajima, and T. Ohsaka, Electrochem. Commun., 7, **2005**, 789-795.

[209] P. Reinsberg, A. Abd-El-Latif, and H. Baltruschat, Electrochim. Acta, 273, **2018**, 424-431.

[210] C. Pozo-Gonzalo, P.C. Howlett, D.R. MacFarlane, and M. Forsyth, Electrochem. Commun., 74, **2017**, 14-18.

[211] E. Azaceta, R. Tena-Zaera, R. Marcilla, S. Fantini, J. Echeberria, J.A. Pomposo, H. Grande, and D. Mecerreyes, Electrochem. Commun., 11, **2009**, 2184-2186.

[212] E. Azaceta, R. Marcilla, D. Mecerreyes, M. Ungureanu, A. Dev, T. Voss, S. Fantini, H.J. Grande, G. Cabanero, and R. Tena-Zaera, Phys. Chem. Chem. Phys., 13, **2011**, 13433-13440.

[213] M. Tulodziecki, J.M. Tarascon, P.L. Taberna, and C. Guery, J. Electrochem. Soc., 159, **2012**, D691-D698.

[214] Y.S. Wang, H.W. Yeh, Y.H. Tang, C.L. Kao, and P.Y. Chen, J. Electrochem. Soc., 164, **2017**, D39-D47.

[215] M. Xu, D.G. Ivey, Z. Xie, and W. Qu, Electrochim. Acta, 89, **2013**, 756-762.

[216] F.R. McLarnon and E.J. Cairns, J. Electrochem. Soc., 138, **1991**, 645-656.

[217] K. Kim, Y.H. Cho, S.W. Eom, H.S. Kim, and J.H. Yeum, Mater. Res. Bull., 45, **2010**, 262-264.

[218] R.E.F. Einerhand, W.H.M. Visscher, and E. Barendrecht, J. Appl. Electrochem., 18, **1988**, 799-806.

[219] X.Z. Yuan, V. Alzate, Z. Xie, D.G. Ivey, E. Dy, and W. Qu, J. Electrochem. Soc., 161, **2014**, A458-A466.

[220] We would like to note that we were not able to reconcile these numbers. First, the equation given by the authors is incorrect in so far as it refers to a 2- or 4-electron process at the disk reaction, which is correct in aqueous electrolytes where H_2O_2 formation needs to be discriminated from H_2O, but not for the present case. Furthermore, the ring potential applied is well in the ORR region. 2019.

[221] C. Pozo-Gonzalo, A.A.J. Torriero, M. Forsyth, D.R. MacFarlane, and P.C. Howlett, J. Phys. Chem. Lett., 4, **2013**, 1834-1837.

[222] R.L. McCreery, Chem. Rev., 108, **2008**, 2646-2687.

[223] M. Wassner, M. Eckardt, C. Gebauer, G.R. Bourret, N. Hüsing, and R.J. Behm, Electrochim. Acta, 227, **2017**, 367-381.

[224] M.H. Seo, S.M. Choi, H.J. Kim, and W.B. Kim, Electrochem. Commun., 13, **2011**, 182-185.

[225] J. Bian, Z. Li, N. Li, and C. Sun, Inorg. Chem., 58, **2019**, 8208-8214.

[226] J. Bian, R. Su, Y. Yao, J. Wang, J. Zhou, F. Li, Z.L. Wang, and C. Sun, ACS Appl. Energy Mater., 2, **2019**, 923-931.

[227] X. Zhang, Y. Gong, S. Li, and C. Sun, ACS Catal., 7, **2017**, 7737-7747.

[228] T. Noda and M. Inagaki, Bull. Chem. Soc. Jpn., 37, **1964**, 1534-1538.

[229] M.R. Arefi and S. Rezaei-Zarchi, Int. J. Mol. Sci., 13, **2012**.

[230] W. Chen, Y.H. Lu, M. Wang, L. Kroner, H. Paul, H.J. Fecht, J. Bednarcik, K. Stahl, Z.L. Zhang, U. Wiedwald, U. Kaiser, P. Ziemann, T. Kikegawa, C.D. Wu, and J.Z. Jiang, J. Phys. Chem. C, 113, **2009**, 1320-1324.

7 Appendix

7.1 Liste der verwendeten Daten

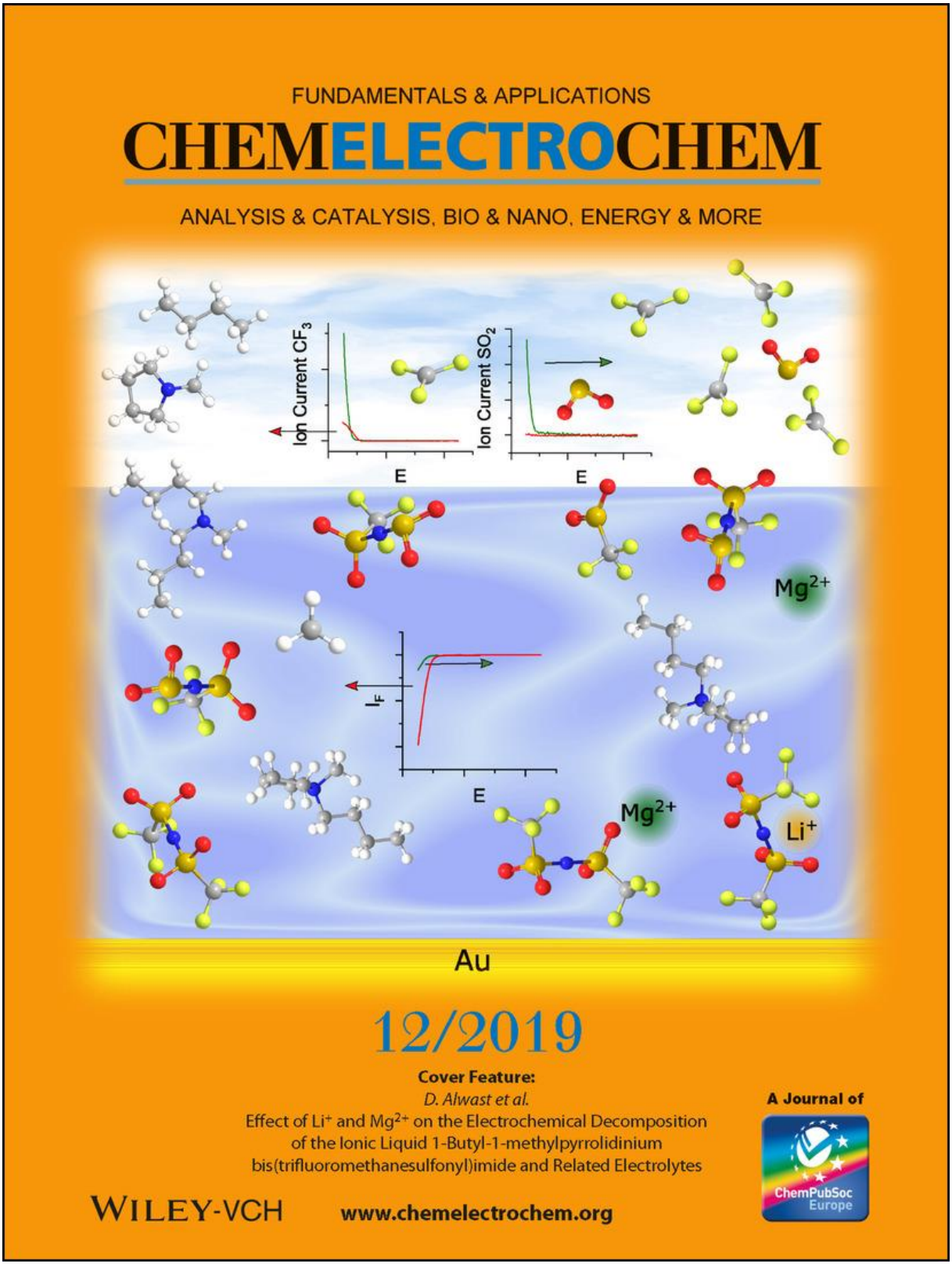
Figure	Source
Figure 7	27.11.2015
Figure 9	15.06.2019
Figure 11	08.05.2015
Figure 13	05.09.2014
Figure 15	24.09.2014
Figure 17	25.09.2014
Figure 19	08.05.2015
Figure 21	05.09.2014
Figure 23	24.09.2014
Figure 25	25.09.2014
Figure 27	25.09.2014
Figure 29	No measurement
Figure 31	07.12.2015 15.01.2016

Figure	Source
Figure 8	09.10.2017
Figure 10	27.04.2015
Figure 12	08.05.2015
Figure 14	23.09.2014
Figure 16	24.09.2014
Figure 18	08.05.2015
Figure 20	05.09.2014
Figure 22	05.09.2014
Figure 24	24.09.2014
Figure 26	25.09.2014
Figure 28	08.05.2015 07.12.2015
Figure 30	No measurement
Figure 32	07.12.2015 14.12.2015 15.12.2015 18.12.2015 15.01.2016 22.01.2016 22.11.2016 23.11.2016 25.11.2016 02.12.2016 05.12.2016 07.12.2016 27.02.2017 28.02.2017 16.03.2017 02.05.2017

Figure 33	05.09.2014 01.02.2016
Figure 34	19.01.2016 20.01.2016 01.02.2016 09.02.2016 07.11.2016 08.11.2016 11.11.2016 14.11.2016 21.11.2016 01.12.2016 06.12.2016 08.12.2016 14.12.2016 14.02.2017 15.02.2017 16.02.2017 17.02.2017
Figure 35	16.03.2017 02.12.2016 07.12.2015 04.11.2016 10.11.2016
Figure 36	17.02.2017 01.12.2016 05.09.2014 07.11.2016 11.11.2016
Figure 37	04.11.2016
Figure 38	23.10.2019 09.09.2019
Figure 39	16.09.2019 24.09.2019 26.11.2019
Figure 40	03.12.2019
Figure 41	06.11.2019 07.11.2019
Figure 42	No measurement
Figure 43	17.08.2018
Figure 44	29.11.2018
Figure 45	05.12.2018 14.12.2018
Figure 46	10.01.2019
Figure 47	No measurement
Figure 48	16.10.2019 17.10.2019

7.2 Lebenslauf

… aus Gründen des Datenschutzes entfernt.



Reprinted with permission by ChemElectroChem / John Wiley and Sons.

7.3 Publikationen

Artikel

1 Benedikt Uhl, Florian Buchner, Dorothea Alwast, Nadja Wagner, R. Jürgen Behm: Adsorption of the ionic liquid [BMP][TFSA] on Au (111) and Ag (111): substrate effects on the structure formation investigated by STM, *Beilstein Journal of Nanotechnology* **2013**, *4*, *1*, 903.

2 Florian Buchner, Katrin Forster-Tonigold, Benedikt Uhl, Dorothea Alwast, Nadja Wagner, Hanieh Farkhondeh, Axel Groß, R. Jürgen Behm: Towards the microscopic identification of anions and cations at the ionic liquid | Ag(111) interface: a combined experimental and theoretical investigation, *ACS Nano* **2013**, *7*, *9*, 7773.

3 Benedikt Uhl, Hsinhui Huang, Dorothea Alwast, Florian Buchner, R. Jürgen Behm: Interaction of ionic liquids with noble metal surfaces: structure formation and stability of [OMIM][TFSA] and [EMIM][TFSA] on Au(111) and Ag(111), *Phys. Chem. Chem. Phys.* **2015**, 17, 23816-23832.

4 Dorothea Alwast, Johannes Schnaidt, Jeuk-Ting Law, R. Jürgen Behm: A Novel Approach for Differential Electrochemical Mass Spectrometry Studies on the Decomposition of Ionic Liquids. *Electrochimica Acta* **2016**, 197, 290.

5 Dorothea Alwast, Johannes Schnaidt, Kurtus Hancock, Gülsah Yetis, R. Juergen Behm: Effect of Li^+ and Mg^{2+} on the Electrochemical Decomposition of the Ionic Liquid 1-Butyl-1-methylpyrrolidinium bis(trifluoromethanesulfonyl)imide and Related Electrolytes, *ChemElectroChem* **2019**, 12, 2967.

6 Dorothea Alwast, Johannes Schnaidt, Zenonas Jusys, R. Jürgen Behm: Ionic Liquid Electrolytes for Metal-Air Batteries: Interactions between O_2, Zn^{2+} and H_2O Impurities, *Journal of the Electrochemical Society* **2020**, 167, 070505.

7 Markus Eckardt*, Dorothea Alwast*, Johannes Schnaidt, R. Jürgen Behm: Influence of additives on the reversible ORR / OER in the magnesium containing ionic liquid N-Butyl-N-methylpyrrolidinium bis(trifluoromethanesulfonyl)imide, ChemSusChem **2020**, 13, 3919.
* Authors contributed equally

8 Fanglin Wu, Guk-Tae Kim, Thomas Diemant, Matthias Kuenzel, Annika Regitta Schür, Xinpei Gao, Bingsheng Qin, Dorothea Alwast, Zenonas Jusys, R. Jürgen Behm, Dorin Geiger, Ute Kaiser, Stefano Passerini: Reducing Capacity and Voltage Decay of Co-Free Li1.2Ni0.2Mn0.6O2 as Positive Electrode Material for Lithium Batteries Employing an Ionic Liquid-Based Electrolyte, *Advanced Energy Materials* **2020**, 10, 2001830.

9 Jin Jyun Chang, Christian Baur, Jean-Marcel Ateba Mba, Denis Arčon, Gregor Mali, Dorothea Alwast, R. Jürgen Behm, Maximilian Fichtner, Tejs Vegge, Juan Maria Garcia Lastra: Superoxide formation in Li2VO2F cathode material – a combined computational and experimental investigation of anionic redox activity, *Journal of Materials Chemistry A* **2020**, 8, 16551.

Vorträge

1 Dorothea Alwast, Johannes Schnaidt, Kurtus Hancock, R. Jürgen Behm:
Decomposition of the Ionic Liquid [BMP][TFSA] on Gold and Glassy Carbon Studied by Differential Electrochemical Mass Spectrometry (DEMS); GDCh Electrochemistry Goslar **2016**.

2 Dorothea Alwast, Johannes Schnaidt, Kurtus Hancock, R. Jürgen Behm:
Model Studies on the Electrochemical Decomposition of BMP TFSI on Gold and Glassy Carbon Electrodes, DPG Frühjahrstagung Dresden **2017**.

Poster

1 Dorothea Alwast, Benedikt Uhl, Florian Buchner, R. Jürgen Behm:
STM investigation on the structure formation of the ionic liquid BMP-TFSA on different metal surfaces; DPG Frühjahrstagung Regensburg **2013**.

2 Dorothea Alwast, Johannes Schnaidt, Yeuk Ting Law, R. Jürgen Behm:
Model Studies on the Electrochemical Decomposition of [BMP][TFSA] on Au electrodes, DPG Frühjahrstagung Berlin **2015**.

3 Dorothea Alwast, Johannes Schnaidt, Yeuk Ting Law, R. Jürgen Behm:
DEMS Study on the Decomposition of Ionic Liquids, 13. Internationales Fischer Symposium Lübeck **2015**.

4 Dorothea Alwast, Johannes Schnaidt, Kurtus Hancock, R. Jürgen Behm:
Decomposition of the Ionic Liquid [BMP][TFSA] on Gold and Glassy Carbon Studied by Differential Electrochemical Mass Spectrometry (DEMS), UECT Blaubeuren **2016** – 3rd Place Poster award

5 Dorothea Alwast, Johannes Schnaidt, Kurtus Hancock, R. Jürgen Behm:
Decomposition of the Ionic Liquid [BMP][TFSA] on Gold and Glassy Carbon Studied by Differential Electrochemical Mass Spectrometry (DEMS), 1st Symposium on Mg Batteries Blaubeuren **2016**.

6 Dorothea Alwast, Gülsah Yetis, Johannes Schnaidt, R. Jürgen Behm:
Influence of Mg^{2+} and Li^{+} Ions on the electrochemical decomposition of [BMP][TFSI] on Au electrodes, DPG Frühjahrstagung Dresden **2017**.

7 Dorothea Alwast, Johannes Schnaidt, Kaidi Zhang, T. Linh Nguyen, Zenonas Jusys, R. Jürgen Behm:
Influence of Mg^{2+} and Zn^{2+} on the ORR and OER in the Ionic Liquid BMP-TFSI, UECT Ulm **2018**.

8 Dorothea Alwast, Johannes Schnaidt, Zenonas Jusys, R. Jürgen Behm:
Influence of Zn^{2+} and of the Addition of Water on the ORR and OER in the Ionic Liquid BMP-TFSI, GDCh Electrochemistry Ulm **2018**.

7.4 Danksagung

... aus Gründen des Datenschutzes entfernt.

7.5 Erklärung

Hiermit erkläre ich, Dorothea Alwast, dass ich die vorliegende Dissertation selbständig verfasst und keine weiteren als die angegebenen Quellen und Hilfsmittel benutzt habe. Alle wörtlich oder inhaltlich übernommenen Stellen habe ich als solche gekennzeichnet. Darüber hinaus versichere ich, dass ich die Satzung der Universität Ulm zur Sicherung guter wissenschaftlicher Praxis beachtet habe.

Ulm, den 04.11.2020

_____

Dorothea Alwast